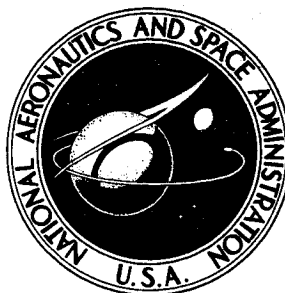


NASA CONTRACTOR REPORT



NASA CR-826

NASA CR-826

FACILITY FORM 602	N 67-34031	
	(ACCESSION NUMBER)	(THRU)
	134 (PAGES)	(CODE)
	(NASA CR OR TMX OR AD NUMBER)	51 (CATEGORY)

ANALYSIS AND DESIGN OF SPACE VEHICLE FLIGHT CONTROL SYSTEMS

VOLUME VII - ATTITUDE CONTROL DURING LAUNCH

by Arthur L. Greensite

Prepared by
GENERAL DYNAMICS CORPORATION
San Diego, Calif.
for George C. Marshall Space Flight Center

NATIONAL AERONAUTICS AND SPACE ADMINISTRATION • WASHINGTON, D. C. • JULY 1967

ANALYSIS AND DESIGN OF SPACE VEHICLE
FLIGHT CONTROL SYSTEMS
VOLUME VII - ATTITUDE CONTROL DURING LAUNCH
By Arthur L. Greensite

Distribution of this report is provided in the interest of information exchange. Responsibility for the contents resides in the author or organization that prepared it.

Issued by Originator as GDC-DDE66-028

Prepared under Contract No. NAS 8-11494 by
GENERAL DYNAMICS CONVAIR
A DIVISION OF GENERAL DYNAMICS CORPORATION
San Diego, Calif.

for George C. Marshall Space Flight Center

NATIONAL AERONAUTICS AND SPACE ADMINISTRATION

PRECEDING PAGE BLANK NOT FILMED.

FOREWORD

This report was prepared under NASA Contract NAS 8-11494 and is one of a series intended to illustrate methods used for the design and analysis of space vehicle flight control systems. Below is a complete list of the reports in the series:

Volume I	Short Period Dynamics
Volume II	Trajectory Equations
Volume III	Linear Systems
Volume IV	Nonlinear Systems
Volume V	Sensitivity Theory
Volume VI	Stochastic Effects
Volume VII	Attitude Control During Launch
Volume VIII	Rendezvous and Docking
Volume IX	Optimization Methods
Volume X	Man in the Loop
Volume XI	Component Dynamics
Volume XII	Attitude Control in Space
Volume XIII	Adaptive Control
Volume XIV	Load Relief
Volume XV	Elastic Body Equations
Volume XVI	Abort

The work was conducted under the direction of Clyde D. Baker, Billy G. Davis and Fred W. Swift, Aero-Astro Dynamics Laboratory, George C. Marshall Space Flight Center. The General Dynamics Convair program was conducted under the direction of Arthur L. Greensite.

PRECEDING PAGE BLANK NOT FILMED.

PRECEDING PAGE BLANK NOT FILMED.

TABLE OF CONTENTS

<u>Section</u>	<u>Page</u>
1. STATEMENT OF THE PROBLEM	1
2. STATE OF THE ART	3
3. RECOMMENDED PROCEDURES	5
3.1 GENERAL FEATURES OF THE ATTITUDE CONTROL PROBLEM.	6
3.2 EQUATIONS OF SHORT-PERIOD DYNAMICS	15
3.3 AUTOPILOT DESIGN	29
3.3.1 Dynamic Modes	29
3.3.1.1 Rigid Body.	31
3.3.1.2 Fuel Sloshing	41
3.3.1.3 Engine Inertia.	46
3.3.1.4 Vehicle Flexibility	50
3.3.2 Stabilization Techniques	62
3.3.2.1 Filters	62
3.3.2.2 Sensor Location	67
3.3.3 Influence of Nonlinearities	72
3.3.4 Approximations	84
3.3.4.1 Aerodynamic Damping	84
3.3.4.2 Modal Coupling	87
3.3.4.3 Load Torque Feedback to Actuator.	91
3.3.4.4 Higher-Order Dynamic Effects	93
3.3.5 Complete Simulation	93
4. REFERENCES	95
APPENDICES	
A. Basic Data for a Typical Launch Vehicle	97
B. Mechanical Analogy for Liquid Sloshing in a Cylindrical Tank	103

PRECEDING PAGE BLANK NOT FILMED.

LIST OF ILLUSTRATIONS

<u>Figure</u>		<u>Page</u>
1	Control Capability of Attitude Control System	7
2	Geometry of Vehicle in Pitch Plane	8
3	Response to Step Gust; $K_\alpha = 1$, $K_\theta = 1$	16
4	Response to Step Gust; $K_\alpha = 1.8$, $K_\theta = 1$	17
5	Response to Step Gust; $K_\alpha = 2.2$, $K_\theta = 1$	18
6	Response to Step Gust; $K_\alpha = 2.2$, $K_\theta = 0$	19
7	Response to Step Gust; $K_\alpha = 1$, $K_\theta = 0$	19
8	Elastic Vehicle in the Pitch Plane	24
9	Schematic of Sloshing Pendulum, Pitch Plane	27
10	Autopilot for Simplified Rigid Body.	34
11	Root Locus for Simplified Autopilot	35
12	Root Locus Showing Influence of One Lag Filter	36
13	Root Locus Showing Influence of Two Lag Filters.	37
14	Bode Plot For Eq. (61)	39
15	Configuration for Disturbance Input	39
16	Pole-zero Configuration for Rigid Body and One Slosh Dipole	44
17	Root Loci Showing Influence of Slosh Damping	47
18	Slosh Stabilization by Passive Filtering	48
19	Root Locus of Simplified Autopilot Showing Influence of Engine Inertia	49
20	Launch Vehicle Autopilot	52
21	Pole-zero Configuration for Case 1	57
22	Pole-zero Configuration for Case 2	58
23	Gain-stabilizing an Unstable Bending Mode	59
24	Pole-zero Configuration for Case 3	60
25	Stability Analysis of Higher Bending Modes, $\sigma_G^{(i)}$ Negative	61
26	Stability Analysis of Higher Bending Modes, $\sigma_G^{(i)}$ Positive	63

LIST OF ILLUSTRATIONS (Contd)

<u>Figure</u>		<u>Page</u>
27	Stabilizing an Unstable Bending Mode by Passive Filters (Case 2) . . .	64
28	Stabilizing an Unstable Bending Mode by Passive Filters (Case 3) . . .	65
29	Root Locus for Case A	68
30	Root Locus for Case B	69
31	Root Locus for Case C	70
32	Root Locus for Case D	71
33	Typical Stability Boundary Plot for Several Flight Times	73
34	Flight History for μ_c	75
35	Flight History for μ_α	76
36	Low-frequency Approximation $K'_c/(s + K'_c)$	77
37	Constant-amplitude and Constant-gain Loci	79
38	Family of Constant-gain vs. Constant-amplitude Loci	79
39	Simplified Autopilot with Equivalent Linear Transfer Function for Actuator	79
40	Equivalent Form of Autopilot of Figure 38	80
41	Pole-zero Configuration for Eq. (113)	82
42	Root Locus for Pole Position p_1	83
43	Root Locus for Pole Position p_2	84
44	Root Locus for Pole Position p_3	85
45	Effect of Aerodynamic Damping on Pitching Mode	86
46	Effect of Aerodynamic Damping on Bending Mode	88
47	Influence of Sloshing Mode	90
48	Load Torque Feedback to Actuator	92
49	Alternate Form of Load Torque Feedback	92
A1	Schematic of Engine Servo System	100
B1	Tank and Liquid Geometry	108
B2	Analogous Mechanical System; Rotational Degree of Freedom Included	121
B3	Analogous Mechanical System; Translational Degree of Freedom Only	124

1. STATEMENT OF THE PROBLEM

A launch vehicle guidance system provides the control system inputs necessary to fly a prescribed trajectory. These inputs are generally in the form of attitude commands whose purpose is to orient the vehicle in a prescribed direction. Normally, the attitude control problem is concerned with the short-period dynamics of the vehicle, where the fundamental aim is to achieve adequate stability and reasonably rapid (and well-damped) response to input commands, with moderate insensitivity to external disturbances (winds). The usual method of studying the short-period dynamics of the vehicle is to analyze perturbations from a reference condition via linear methods and to arrive at an autopilot configuration that meets design requirements. Actually, while this problem may be analyzed to a large extent independently of the guidance problem, the two cannot be completely divorced. The characteristics of the autopilot will have a significant influence on trajectory dispersions, especially during the atmospheric phase. Winds, for example, will tend to cause deviations from a reference trajectory. The vehicle autopilot will usually be required to meet conflicting requirements: 1) to minimize trajectory deviations; and 2) to minimize various excursions (e.g., angle of attack) in order to ensure structural integrity of the vehicle.

The general features of the attitude control problem, especially as it relates to trajectory deviations, are discussed in Sec. 3.1. Related discussions are contained in other monographs in this series*. This monograph is concerned primarily with the short-period dynamics of attitude control and is a direct extension of material in "Short Period Dynamics" and "Elastic Body Equations," parts 1 and 2 of Vol. I in the series. This material provides the conceptual framework for the autopilot design problem that will be discussed here in some detail.

The distinguishing features of the attitude control problem of a launch vehicle are:

- a. The use of swivelled engines for attitude control.
- b. The rapidly varying mass and inertial properties of the vehicle.
- c. The extreme flexibility of the vehicle.
- d. The influence of propellant sloshing.
- e. Aerodynamic instability of the airframe.
- f. The need for completely automatic control.

*cf. Vol. I, part 3, "Trajectory Equations;" Vol. III, part 2, "Load Relief."

Because a failure of any one of a multitude of systems or components could mean the loss of the vehicle, an extensive ground testing and evaluation program is necessary. This has motivated the development of highly refined methods of analysis that could provide the maximum confidence for successful flight. Probably the most severe problem is that of vehicle flexibility, ⁽¹²⁾ which manifests itself in the sensing of local elastic deflections by the gyroscopes. When the bending mode and control frequencies are of the same order of magnitude, potential stability problems exist. The problem is complicated by the facts that passive filtering compromises the gain and phase margins of the fundamental control loop and that the bending-mode frequencies vary in flight.

The monograph discusses the usual stabilization techniques as well as the influence of various nonlinearities. The final section considers the errors introduced by the use of various approximate transfer functions in design and analysis.

2. STATE OF THE ART

Major design problems arise because a launch vehicle is aerodynamically unstable and highly flexible. Further complications are introduced by sloshing of liquid propellants and the inertia effects of swivelling engines. The aim of any analysis is to formulate the simplest mathematical model that will account for all significant phenomena. Depending on the precision of results required for specific purposes, various simplified models may be used. Thus, for preliminary design studies, only crude estimates may be necessary. Alternatively, in finalizing a design, a rather extensive formulation is required. Consequently, the design problem may be analyzed at various levels of sophistication.

The design of the attitude control system is thus conducted in several phases. One is concerned primarily with developing an autopilot configuration that achieves adequate short-period stability and performance. This makes use of the so-called "time slice" approach, in which time-varying mass and inertial properties are "frozen" over a short period of time. In this way, the powerful techniques of linear analysis are exploited most fully, thereby reducing overwhelming analytical difficulties to manageable proportions. This is usually followed by time-varying simulations on a computer (incorporating all significant nonlinearities) and refinement of various elements of the control system as necessary. The major input here (in addition to guidance commands) is the wind profile -- more specifically, a series of wind profiles. This permits an evaluation of the system with respect to trajectory dispersions, induced binding loads, and time histories of various parameters of interest (e.g., angle of attack and thrust angle deflection).

It has also been found that the sloshing of the liquid propellants introduces dynamic effects that may lead to instability unless properly compensated. For purposes of analyzing this phenomenon, it has been found that the sloshing liquid may be replaced by a rigid mass and series of pendulums whose size and location are a function of the tank shape and liquid level. (13)

From an analytical point of view, the most difficult part of the problem is the need to design an autopilot for a high-order, nonlinear, time-varying system. Experience has shown that analyzing the system at fixed times of flight, in which a linear constant coefficient representation is used, leads to a satisfactory design. Further checks and refinements are made by simulating the complete time-varying dynamics on a computer. At present, this procedure has been generally adopted and has been validated by extensive flight experience.

Many of the problems mentioned above are seriously aggravated for certain advanced configurations. In these cases, conventional methods are only marginally effective, primarily because the bending mode and control frequencies are in close proximity and the bending mode properties are not known with sufficient precision. This has led to the consideration of so-called "adaptive control," a technique that is beyond the scope of this monograph. It is considered in part 8 of Vol. III in the series.

3. RECOMMENDED PROCEDURES

A prerequisite to the design of a launch vehicle autopilot is the determination of the mission profile, reference trajectory, and overall vehicle configuration. Studies of this nature are conducted with varying degrees of sophistication. In the preliminary phases of analysis, the vehicle is assumed to be a point mass that can be steered perfectly along the prescribed trajectory. Under the action of known aerodynamic, propulsive, and gravity forces, a reference trajectory is determined, along with payload capacity, fuel volumes, burning rates, etc., which serve to define the overall vehicle characteristics. For purposes of the ensuing discussions, it is assumed that the vehicle configuration and mission profile have been specified. It is now necessary to investigate the short-period dynamics of the vehicle and to design an autopilot that will:

- a. Stabilize the vehicle.
- b. Ensure reasonably rapid response to guidance commands.
- c. Provide adequate safety margins for anticipated extraneous (wind) disturbances.

This design proceeds by stages, beginning with the use of highly simplified mathematical models to determine "order-of-magnitude" parameters for the system. Such an approach permits the analysis of general design philosophies and concepts, yielding qualitative results on the relative merits of each. Furthermore, by introducing the various dynamic modes (sloshing, bending, instrumentation dynamics, etc.) in stages, the salient features of each are determined with a minimum of complexity. This approach has the virtue of providing maximum insight into the dynamic operation of the system, free of the inertial and elastic coupling effects that tend to obscure understanding.

Thus, the design of a launch vehicle autopilot may be conveniently divided into four phases:

1. Point mass determination of reference trajectory.
2. Rigid body analysis to determine performance characteristics (drift, loading, response time, etc.).
3. Flexible body analysis to determine filters, gyro locations, and stability characteristics.
4. Computer simulation with nonlinear, time-varying coefficients to determine both stability and performance characteristics in response to design winds.

In phase 2 the basic control gains are calculated. These are further refined in phase 3 and usually result in values approximately 40-60% lower than those calculated

in phase 2. Phase 4 gain values are the linearized curve fit values from phase 3, and are the actual flight values which are programmed as a function of flight time.

The material that follows is divided into three main categories. Sec. 3.1 is concerned with the general features of the attitude control problem, especially as it relates to interaction with guidance and loads. A detailed treatment of these considerations is contained in parts 2 and 10 of Vol. III in the series. Sec. 3.2 contains a complete set of the equations of short-period dynamics derived in Ref. 1. Related material on trajectory aspects and component dynamics may be found in part 3, Vol. I (Trajectory Equations), and part II, Vol. III (Component Dynamics), of the series.

In Sec. 3.3, the autopilot design problem is considered in detail. The general features of the salient dynamic modes are discussed first, followed by a consideration of the usual techniques for providing stability augmentation. The influence of various nonlinear effects is considered next, together with appropriate analytical techniques. A discussion of approximate transfer functions and of a complete computer simulation concludes the presentation.

3.1 GENERAL FEATURES OF THE ATTITUDE CONTROL PROBLEM

The first requirement of attitude control is that there exist sufficient control capability to counteract anticipated aerodynamic loads. Referring to Fig. 1, this requirement is formulated quantitatively as

$$T_c \delta_{\max} l_c > L_{\alpha} l_{\alpha} \alpha_{\max} \quad (1)$$

where

T_c = control thrust

L_{α} = aerodynamic load per unit angle of attack

l_c = distance from mass center of vehicle to engine swivel point

l_{α} = distance from mass center of vehicle to center of pressure

δ = thrust deflection angle

α = angle of attack

In short, the thrust control moment must be greater than the maximum anticipated aerodynamic moment. Based on a maximum available thrust deflection angle, δ_{\max} , a maximum permissible angle of attack, α_{\max} , is determined. Exceeding this angle leads to loss of control. Eq. (1) yields only a first approximation of control capability, since dynamic overshoot effects have not been considered. For preliminary

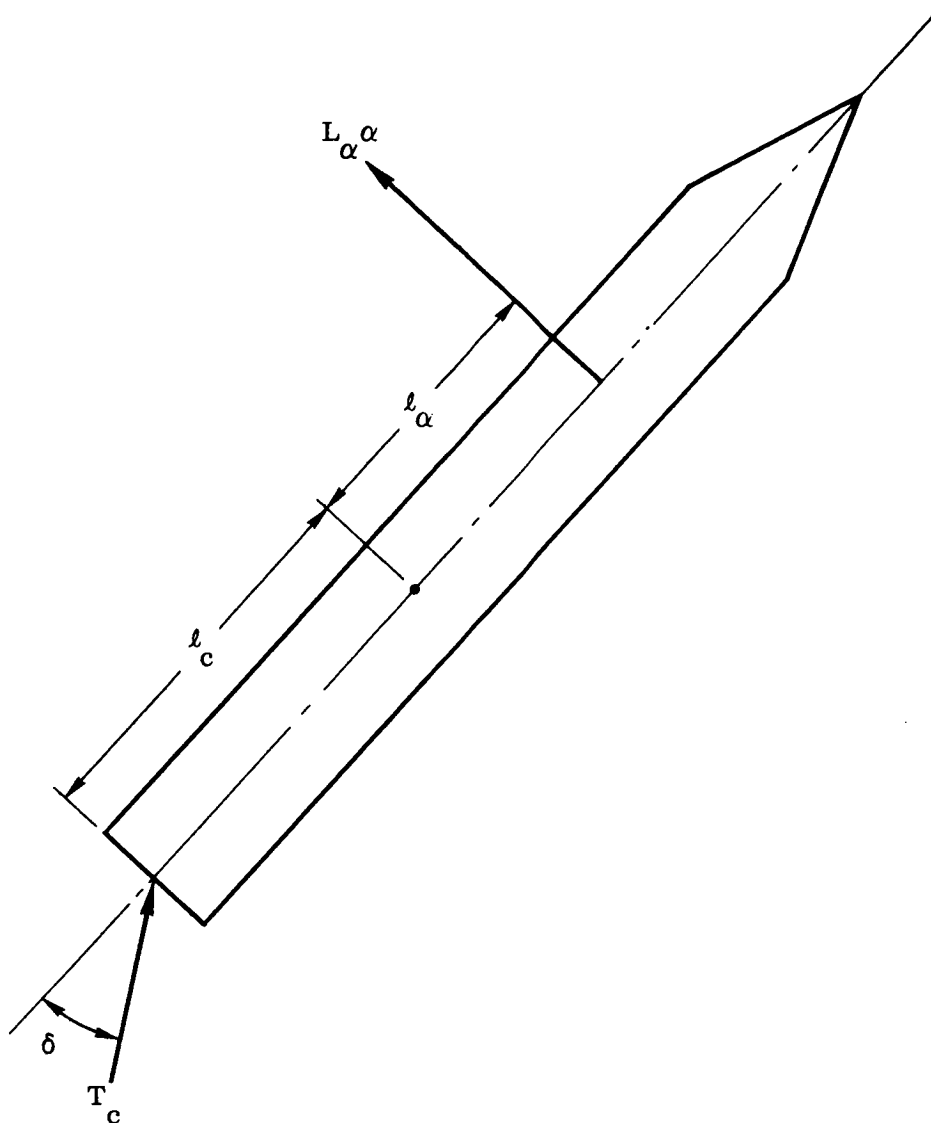


Figure 1. Control Capability of Attitude Control System

estimates, one may reduce α_{\max} by 30-50 percent to take account of the dynamic effects. As the design is refined, complete time-varying computer simulations, using many wind profiles, are employed to ensure that critical parameters are within design limits. These factors are considered in detail in part 10, Vol. III (Response Studies) of this series.

Before turning to a detailed consideration of the autopilot, which is concerned primarily with stabilizing the short-period motions of the vehicle, it is necessary to examine the influence of autopilot characteristics as they relate to loads and guidance. As noted above, the induced angle of attack in response to winds (especially in regions of high dynamic pressure) must be limited, to avoid loss of control. This induced angle of attack must also be controlled in order to limit the resulting bending moment. On the other hand, it is necessary to minimize deviations from the nominal trajectory,

since excessive guidance corrections result in payload penalty. These are conflicting requirements. The broad features of possible tradeoffs may be studied with reference to Fig. 2, which depicts the pitch plane geometry of the rigid vehicle. Neglecting the

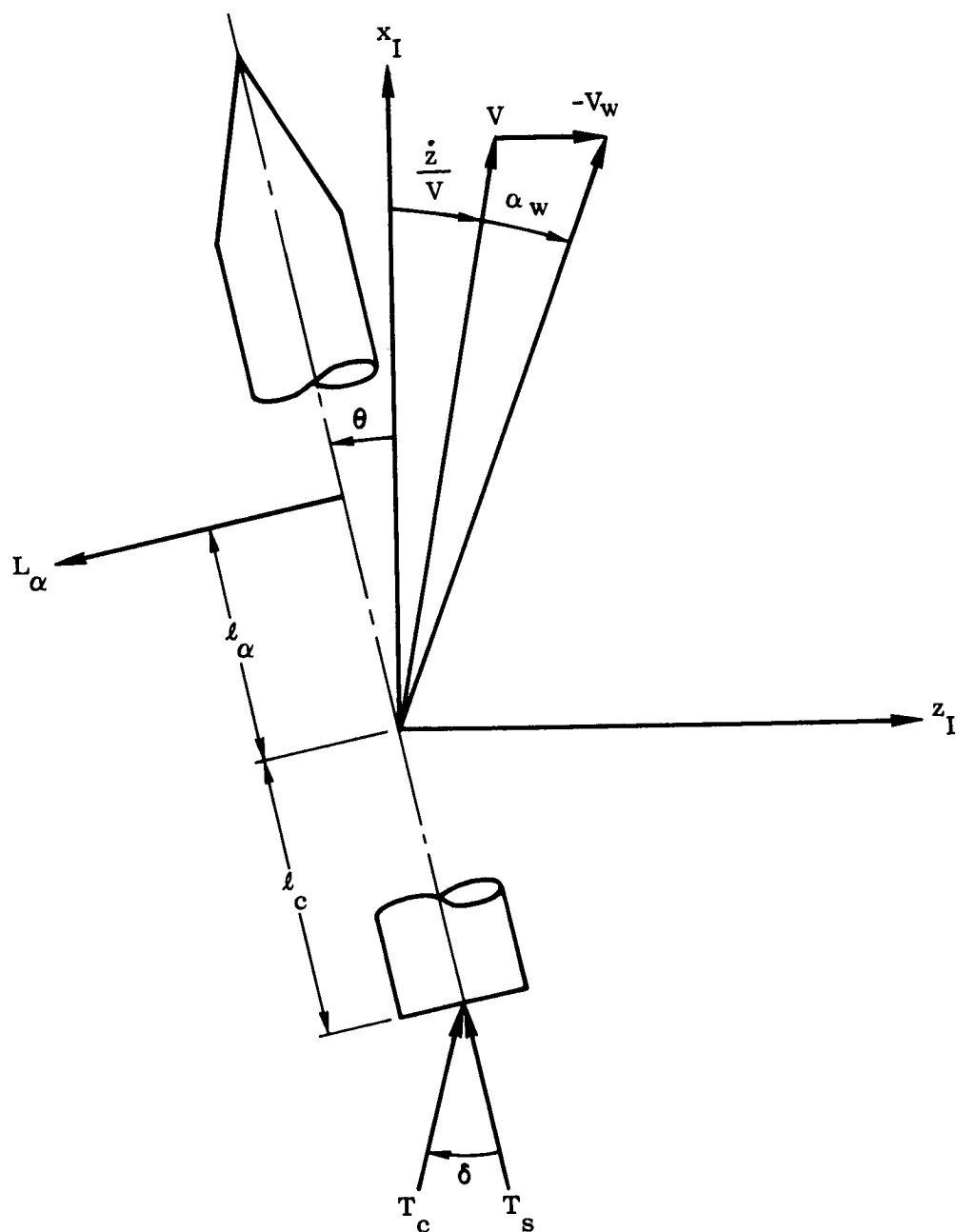


Figure 2. Geometry of Vehicle in Pitch Plane

effects of bending and sloshing and the lags due to actuator and instrumentation dynamics, the motion of the vehicle is described by

$$\ddot{z} = - \frac{(T_T - D)}{m} \theta - \frac{L_\alpha}{m} \alpha + \frac{T_c}{m} \delta \quad (2)$$

$$\ddot{\theta} = \mu_\alpha \alpha + \mu_c \delta \quad (3)$$

$$\alpha = \theta + \frac{\dot{z}}{V} + \alpha_w \quad (4)$$

where

D = drag

I = moment of inertia of vehicle about pitch axis

m = mass of vehicle

T_s = sustainer (nonswivelled) thrust

$T_T = T_c + T_s$

V = forward velocity of vehicle

V_w = wind velocity

z = normal displacement of vehicle relative to inertial frame

α_w = gust angle of attack = $-\frac{V_w}{V}$

θ = attitude angle of vehicle relative to inertial frame

$\mu_\alpha = \frac{L_\alpha \ell_\alpha}{I}$

$\mu_c = \frac{T_c \ell_c}{I}$

and other symbols are as defined previously.

The control law is expressed as

$$\delta = -K_A \left(K_R \dot{\theta} + K_\theta \theta + K_\alpha \alpha \right) \quad (5)$$

K_A = servoamplifier gain

K_R = rate gyro gain

K_θ = position gyro gain

K_α = gain of angle-of-attack sensor

In an attitude control system, $K_\theta = 1$. However, we write K_θ instead of unity to preserve the possibility of trading attitude control for other features. One may also sense normal acceleration rather than angle of attack for use as a feedback control variable. This will generally lead to the same type of autopilot properties.

By straightforward manipulation of Eqs. (2) - (5), we obtain the transfer functions

$$\frac{\dot{z}}{\alpha_w V} = - \frac{a_2 s^2 + a_1 s + a_0}{\Delta} \quad (6)$$

$$\frac{\theta}{\alpha_w} = - \frac{(\mu_c K_A K_\alpha - \mu_\alpha) s}{\Delta} \quad (7)$$

$$\frac{\delta}{\alpha_w} = - \frac{K_A s (K_\alpha s^2 + \mu_\alpha K_R s + \mu_\alpha K_\theta)}{\Delta} \quad (8)$$

$$\frac{\alpha}{\alpha_w} = \frac{s (s^2 + \mu_c K_A K_R s + \mu_c K_A K_\theta)}{\Delta} \quad (9)$$

where

s = Laplace operator

$$a_2 = \frac{T_c}{m V} \left(K_A K_\alpha + \frac{L_\alpha}{T_c} \right)$$

$$a_1 = \frac{K_A T_c K_R}{m V} \left(\mu_\alpha + \frac{\mu_c L_\alpha}{T_c} \right)$$

$$a_0 = \frac{T_c K_A K_\theta}{m V} \left(\mu_\alpha + \frac{\mu_c L \alpha}{T_c} \right) - \frac{T_T - D}{m V} \left(\mu_c K_A K_\alpha - \mu_\alpha \right)$$

$$\Delta = s^3 + B_2 s^2 + B_1 s + B_0 \quad (10)$$

$$B_2 = \mu_c K_A K_R + \frac{T_c}{m V} \left(K_A K_\alpha + \frac{L \alpha}{T_c} \right)$$

$$B_1 = \mu_c K_A \left(K_\theta + K_\alpha \right) - \mu_\alpha + \frac{K_A T_c K_R}{m V} \left(\mu_\alpha + \frac{\mu_c L \alpha}{T_c} \right)$$

$$B_0 = \frac{T_c K_A K_\theta}{m V} \left(\mu_\alpha + \frac{\mu_c L \alpha}{T_c} \right) - \frac{T_T - D}{m V} \left(\mu_c K_A K_\alpha - \mu_\alpha \right)$$

Certain general features of this system are now readily derived. If we assume a unit step input in gust

$$\alpha_w(s) = \frac{1}{s}$$

then the Final Value Theorem yields*

$$\lim_{t \rightarrow \infty} \left(\frac{\dot{z}}{V} \right) = -1$$

$$\lim_{t \rightarrow \infty} \theta = 0$$

$$\lim_{t \rightarrow \infty} \delta = 0$$

$$\lim_{t \rightarrow \infty} \alpha = 0$$

In other words, in the steady state, θ , δ , and α are all zero and the vehicle drifts in the negative z_I direction with a velocity $\dot{z} = V_w$.

*Assuming that $\Delta=0$ has all its roots in the left-half plane.

Some further results relating to transient effects may be obtained by examining the characteristic equation (10). This has three roots, two of which (usually complex conjugates) are associated with the rotary motion of the vehicle about its center of gravity. The third root describes essentially the response of the flight path (lateral drift) to wind. Since the fundamental time constant associated with lateral drift is generally much greater than that associated with vehicle oscillation about the mass center, it is reasonable to analyze a so-called "quasi steady-state" condition wherein the first- and higher-order derivatives in θ are set equal to zero. (4)

Thus by substituting Eqs. (4) and (5) in Eq. (3), we find

$$\theta = - \frac{(\mu_c K_A K_\alpha - \mu_\alpha)}{\left[s^2 + \mu_c K_A K_R s + \mu_c K_A (K_\theta + K_\alpha) - \mu_\alpha \right]} \left(\frac{\dot{z}_{ss}}{V} + \alpha_w \right) \quad (11)$$

Setting the first and second derivatives of θ equal to zero,

$$\theta_{ss} = - \frac{(\mu_c K_A K_\alpha - \mu_\alpha)}{[\mu_c K_A (K_\theta + K_\alpha) - \mu_\alpha]} \left(\frac{\dot{z}_{ss}}{V} + \alpha_w \right) \quad (12)$$

By substituting (12) into Eqs. (4) and (5) we obtain the quasi steady-state values for α and δ ; viz.,

$$\alpha_{ss} = \frac{K_A K_\theta \mu_c}{\mu_c K_A (K_\theta + K_\alpha) - \mu_\alpha} \left(\frac{\dot{z}_{ss}}{V} + \alpha_w \right) \quad (13)$$

$$\delta_{ss} = - \frac{K_A K_\theta \mu_\alpha}{[\mu_c K_A (K_\theta + K_\alpha) - \mu_\alpha]} \left(\frac{\dot{z}_{ss}}{V} + \alpha_w \right) \quad (14)$$

We find, therefore, that the quasi steady-state values of θ , α , and δ , depend on the autopilot gains and the parameter $(\dot{z}/V + \alpha_w)$. It is instructive to investigate the conditions whereby \dot{z} is a constant. If we combine Eqs. (6) and (7) and apply the quasi steady-state assumptions, we find

$$\frac{\dot{z}_{ss}}{V} = \frac{-V a_0}{[\mu_c K_A (K_\theta + K_\alpha) - \mu_\alpha]} \left(\frac{\dot{z}_{ss}}{V} + \alpha_w \right) \quad (15)$$

This shows that $\dot{z}_{ss} = 0$ whenever $B_0 = 0$, regardless of the wind input. Hoelker⁽⁴⁾ calls this the Drift Minimum condition. To examine this effect quantitatively, consider the transfer function, Eq. (6), with $B_0 = 0$. Then if α_w is a unit step input, we find

$$\lim_{t \rightarrow \infty} \left(\frac{\dot{z}}{V} \right) = - \frac{1}{1 + \frac{m V [\mu_c K_A (K_\theta + K_\alpha) - \mu_\alpha]}{K_A K_R T_c \left(\mu_\alpha + \frac{\mu_c L_\alpha}{T_c} \right)}} \quad (16)$$

Using the values given in Table 1, with $K_\theta = 1$ and $K_\alpha = 1.80$ (which makes $B_0 = 0$), this becomes

$$\lim_{t \rightarrow \infty} \left(\frac{\dot{z}}{V} \right) = - 0.0102$$

Thus, by applying the drift minimum condition, the lateral drift has been reduced by a factor of 50. The variables θ , α , and δ take on values in accordance with Eqs. (12) - (14). If K_α is further increased such that $B_0 = 0$, then \dot{z}/V will take on a positive value; i.e., the vehicle will drift into the wind. This will further reduce the trajectory deviations. However, the motion is unstable (as indicated by a positive root in the characteristic equation). Nevertheless, if the drift rate is small, one may accept a temporarily unstable condition in order to limit trajectory deviations.

The drift minimum condition, $B_0 = 0$, may be expressed as follows.

$$T_C K_A K_\theta \left(\mu_\alpha + \frac{\mu_c L_\alpha}{T_c} \right) = (T_T - D) (\mu_c K_A K_\alpha - \mu_\alpha)$$

which, after a simple rearrangement, becomes

$$\frac{\mu_c K_A K_\alpha - \mu_\alpha}{\mu_c K_A K_\theta} = \frac{L_\alpha}{(T_T - D)} \left(1 + \frac{l_\alpha}{l_c} \right) \quad (17)$$

For an aerodynamically stable vehicle, $\mu_\alpha < 0$ and $l_\alpha < 0$, while $|l_\alpha| < l_c$. This means that the right-hand side of Eq. (17) is always positive and the drift minimum condition can be satisfied for some value of K_A even if $K_\alpha = 0$. However, an aerodynamically unstable vehicle will generally require some finite value for K_α in order that the drift minimum condition (17) be satisfied.

Table 1. Typical Launch Vehicle Parameters at Max q

I	$= 2.43 \times 10^6 \text{ slug ft}^2$
l_{α}	$= 38.0 \text{ ft}$
l_c	$= 32.3 \text{ ft}$
L_{α}	$= 240,000 \text{ lb/rad}$
m	$= 5830 \text{ slugs}$
T_c	$= 341,000 \text{ lb}$
$T_T - D$	$= 375,000 \text{ lb}$
V	$= 1320 \text{ ft/sec}$
K_A	$= 2$
K_R	$= 0.4 \text{ sec}^{-1}$
μ_{α}	$= 3.75$
μ_c	$= 4.54$

Consider now the problem of minimizing the excursions in angle of attack in response to wind gusts. We note from Eqs. (13) and (14) that the quasi steady-state values of α and δ are zero if $K_{\theta} = 0$, regardless of the gust magnitudes. The condition $K_{\theta} = 0$ is called the Load Minimum⁽⁴⁾ condition. In this case,

$$\alpha_{ss} = \delta_{ss} = 0$$

while

$$\theta_{ss} = -\left(\frac{\dot{z}}{V} + \alpha_w\right) \quad (18)$$

$$\frac{\dot{z}}{V} = \frac{T_T - D}{m V} \left(\frac{\dot{z}}{V} + \alpha_w\right) \quad (19)$$

This indicates that the vehicle will turn into the wind and the lateral drift will be opposite to the direction of wind velocity. The motion is unstable, since $B_0 < 0$. However, this may not be objectionable for short periods, especially when the prime consideration is the reduction of aerodynamic loads on the vehicle.

In order to obtain some feel for the orders of magnitude involved, the system was simulated on an analog computer. The results are displayed in Figs. 3 through 7. The vehicle parameters of Table 1 were used, and in each case a step gust of 0.10 rad was applied as an input. While this is not a physically realistic gust, it serves to highlight the response characteristics of the system. In all cases, the transients associated with oscillation of the vehicle about its c.g. damp out in less than 2 seconds.

Fig. 3 shows a stable condition; $K_\alpha = 1$ leads to $B_0 > 0$, and all the roots of the characteristic Eq. (10) have negative real parts. As noted earlier this ultimately reaches a steady-state value, $\dot{z}_{ss} = V_w$, which in the present case is $\dot{z}_{ss} = 132$ ft/sec for a step input in α_w of 0.10 rad.

The drift minimum case is shown in Fig. 4, where $K_\alpha = 1.80$ corresponds to $B_0 = 0$. The zero drift condition is clearly evident.

In Fig. 5, K_α is increased to 2.2, which leads to a positive \dot{z} , indicating that the vehicle now drifts into the wind. (Compare with Fig. 3.) As noted earlier, this is because B_0 goes negative. Figs. 6 and 7 show the load minimum condition ($K_\theta = 0$) for two values of K_α . The essentially zero values for α and δ are quite apparent (following the short-period transients). Also shown is the divergence in attitude, θ , in a negative direction, meaning that the vehicle turns into the wind. The positive values for \dot{z} (lateral drift into the wind) have been discussed earlier in connection with Eq. (19).

Further refinements in both design and concept are possible; for example, by using time-varying coefficients in the simulation or time-varying gains on the feedback parameters. This is rarely justified in the preliminary stages, although final validation of the design should utilize as detailed a simulation as possible. The precise tradeoffs between load alleviation and trajectory dispersion is a function of the particular mission and vehicle configuration.

3.2 EQUATIONS OF SHORT-PERIOD DYNAMICS

The equations of short-period dynamics are derived in Ref. 1. They represent perturbations from a nominal steady-state condition such that, by assuming small deviations, a set of linear differential equations is obtained. These are valid only for short time periods (time-slice approximation), since the mass and inertial properties of the vehicle are time-varying. The attitude control system is usually designed by assuming negligible coupling between the pitch, roll, and yaw channels. This is generally a very good approximation, since a conventional launch vehicle possesses a high degree of axial symmetry. Consequently, only the pitch plane equations are presented below. The design procedures for the yaw and roll channels will be similar to those developed for the pitch plane.

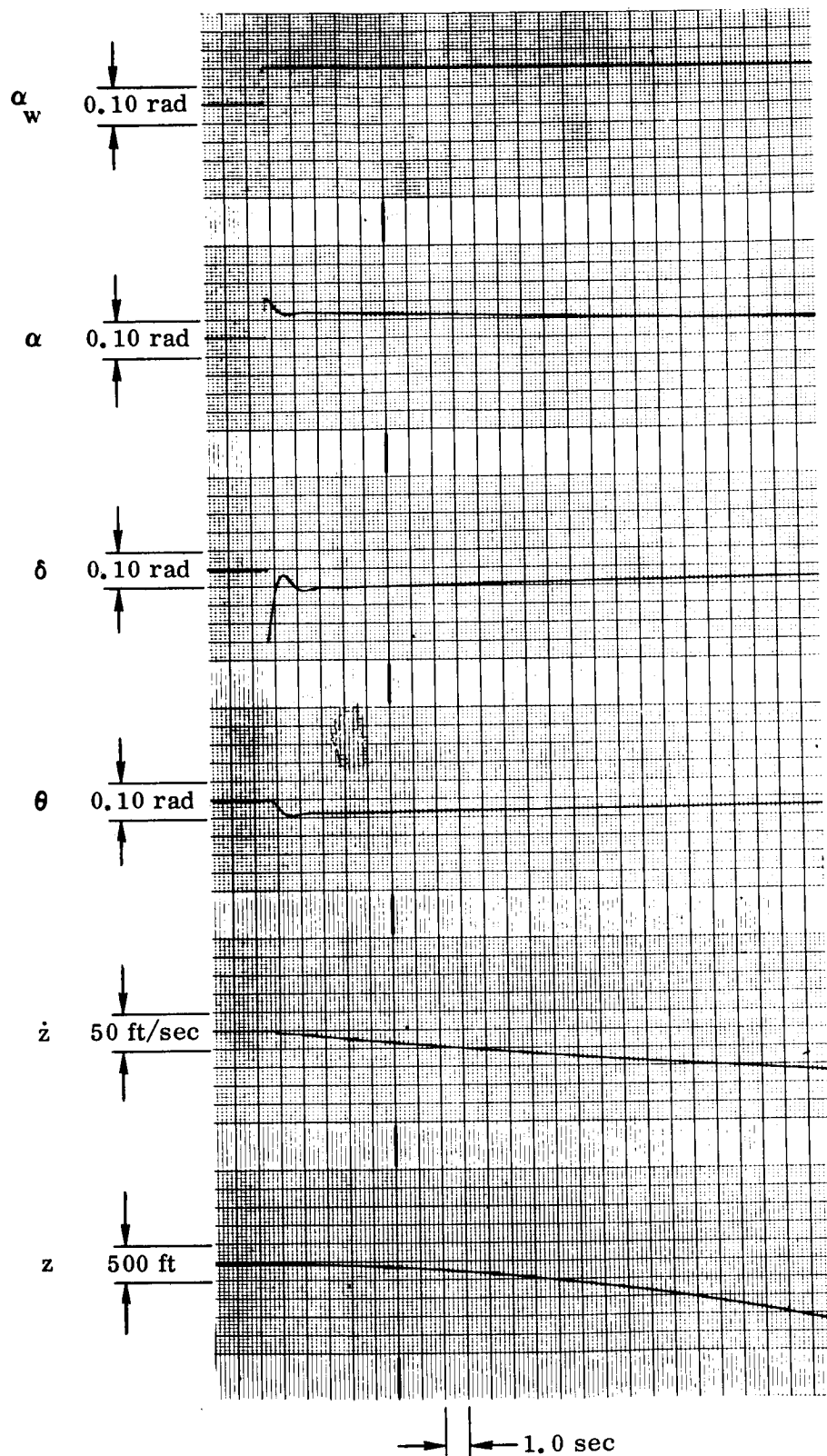


Figure 3. Response to Step Gust; $K_\alpha = 1$, $K_\theta = 1$

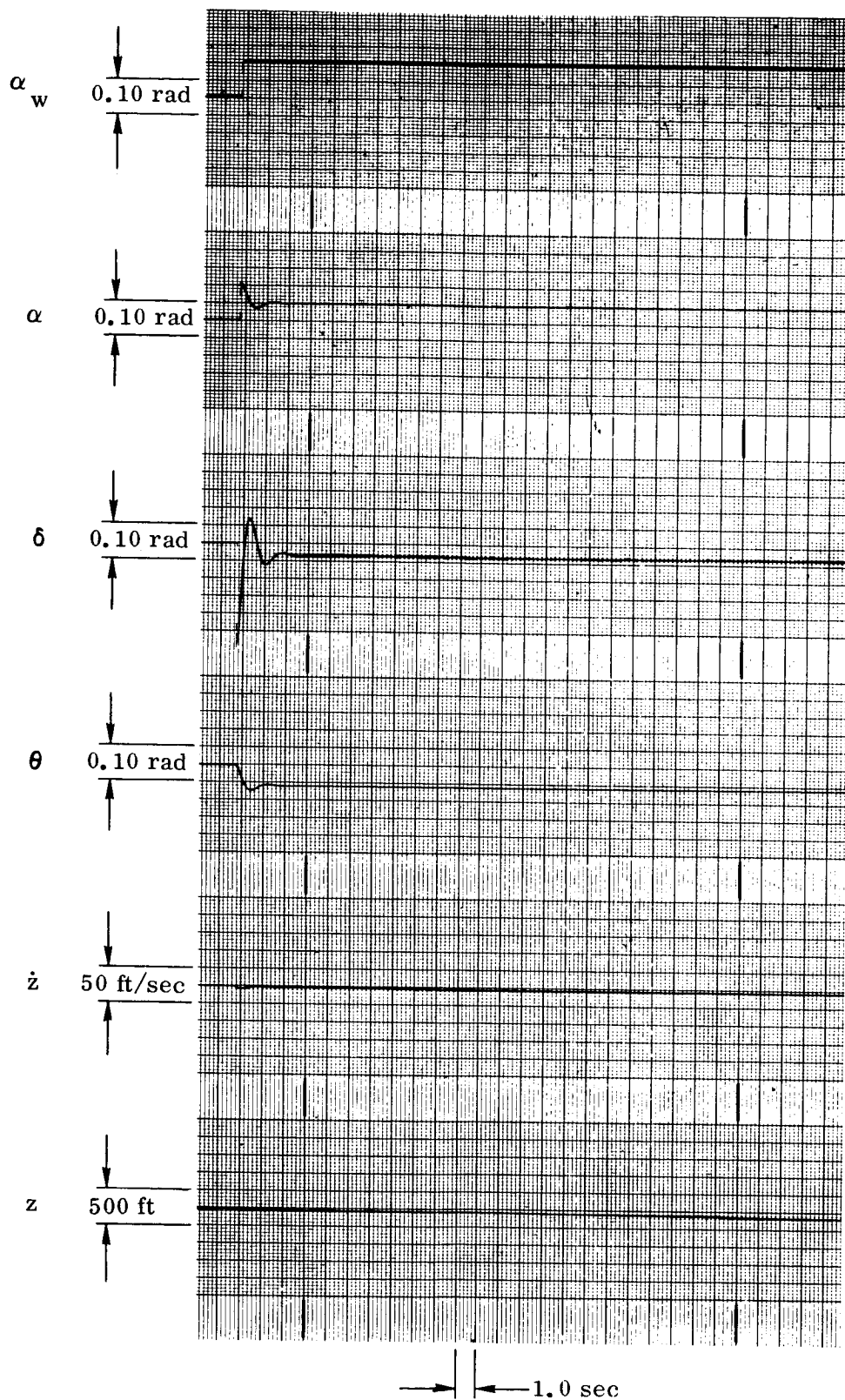


Figure 4. Response to Step Gust; $K_\alpha = 1.8$, $K_\theta = 1$

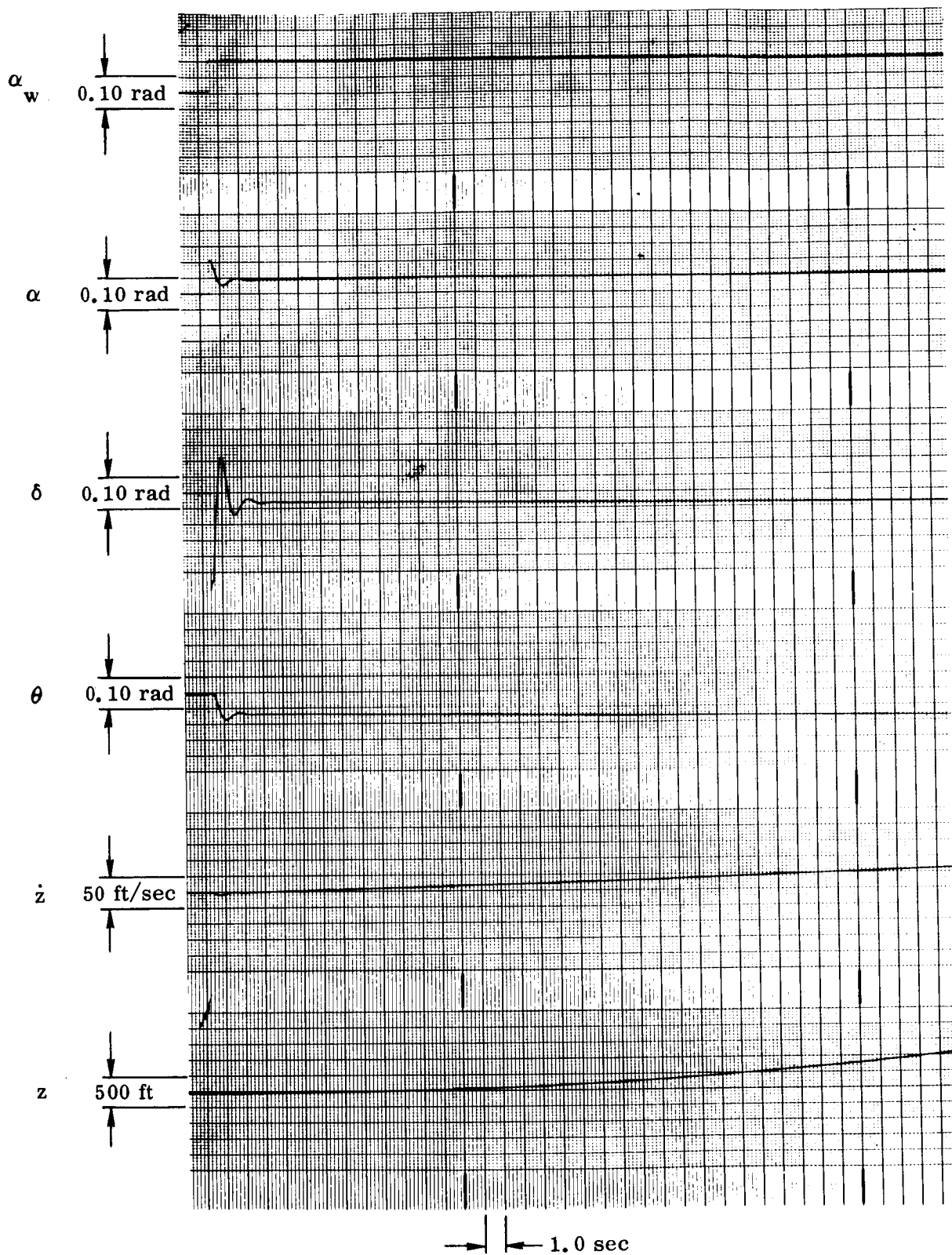


Figure 5. Response to Step Gust; $K_\alpha = 2.2$, $K_\theta = 1$

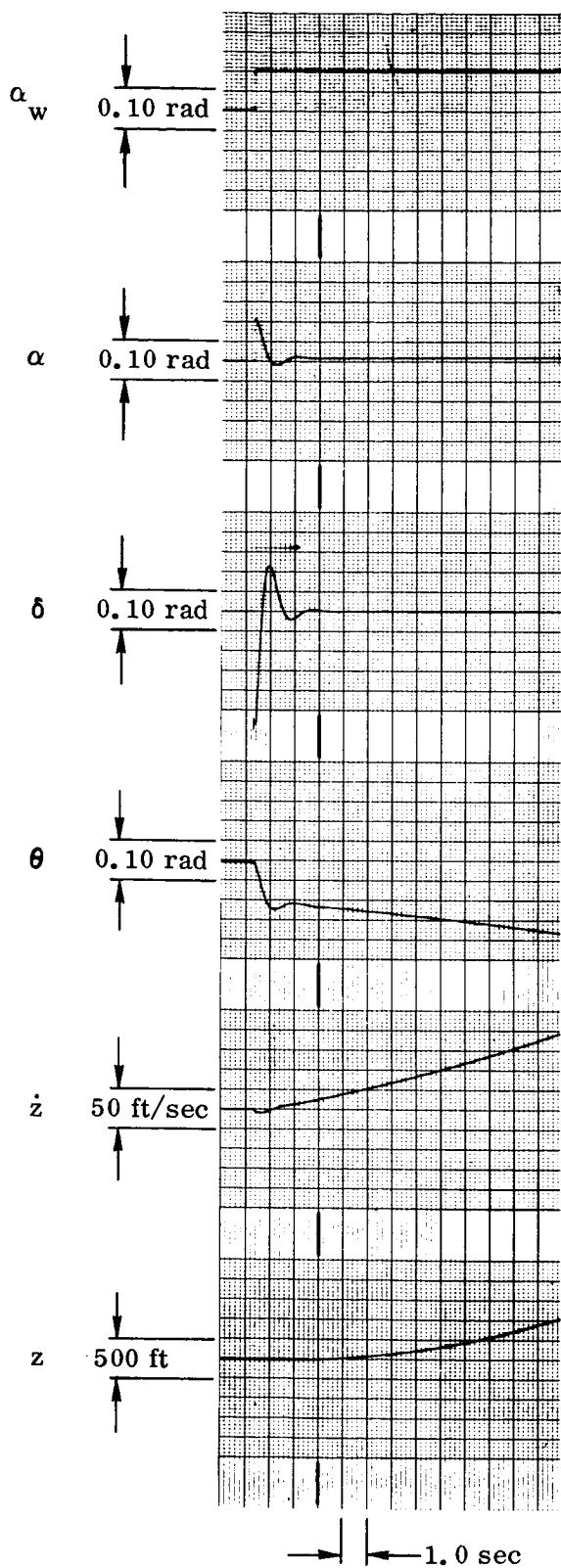


Figure 6. Response to Step Gust;
 $K_{\alpha} = 2.2, K_{\theta} = 0$

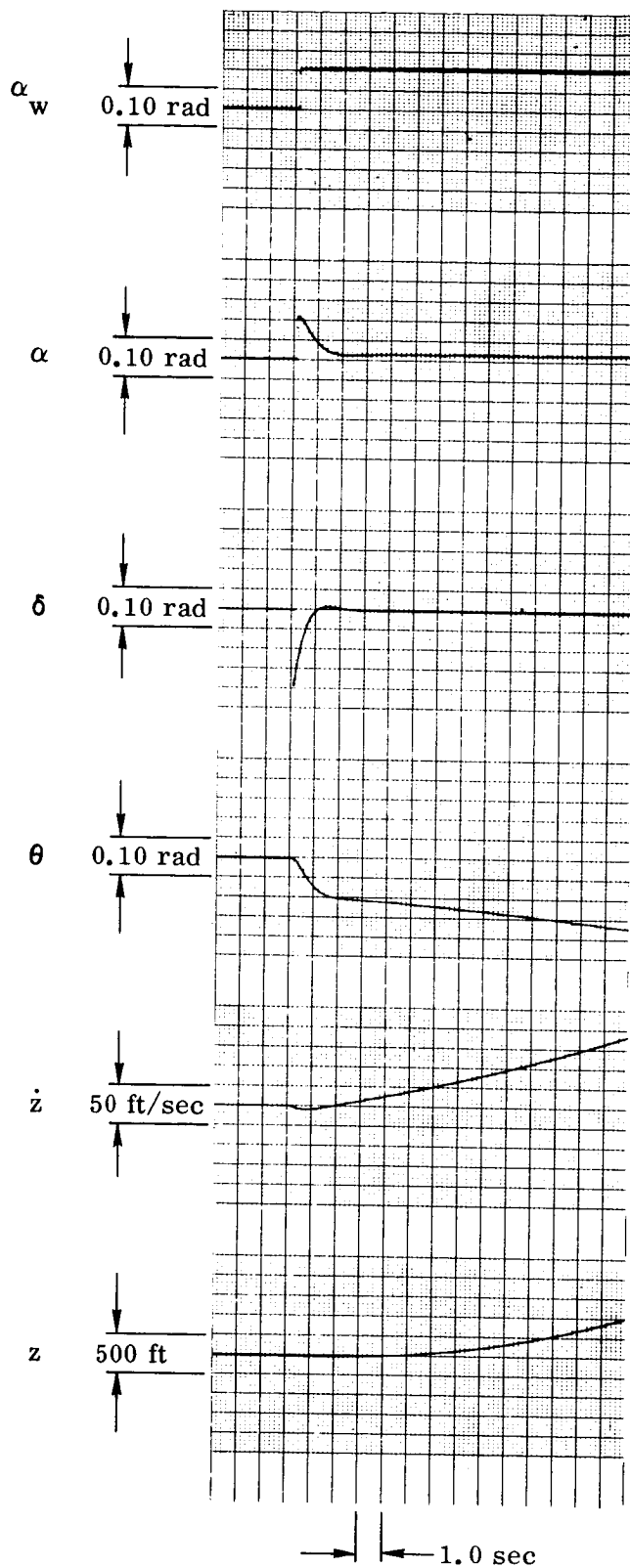


Figure 7. Response to Step Gust;
 $K_{\alpha} = 1, K_{\theta} = 0$

The following symbols are used in this section.

A_1, A_2 = reference areas; see Eqs. (25) and (26)

C_N = normal force coefficient

D = drag

ΣF_z = total perturbation force acting parallel to vehicle body axis, Z'

g = gravity acceleration

I_{xx} = moment of inertia of reduced vehicle (i.e., excluding sloshing masses) about pitch axis

I_0 = moment of inertia of rocket engine about its c.g.

I_R = moment of inertia of rocket engine about swivel point; $= I_0 + M_R \ell_R^2$

K_a = accelerometer gain

K_A = servoamplifier gain

K_b = load torque feedback gain

K_c = engine servo gain

K_I = integrator gain

K_R = rate gyro gain

K_α = angle of attack meter gain

ℓ = length parameter along vehicle longitudinal axis; positive in aft direction

ℓ_a = distance from nose of vehicle to origin of body axis system (see Fig. 8)

ℓ_A = distance from c.g. of vehicle to accelerometer location; positive forward

ℓ_c = distance from origin of body axis system to engine swivel point (see Fig. 8)

ℓ_m = distance from c.g. of vehicle to angle of attack sensor; positive forward

ℓ_R = distance from c.g. of rocket engine to engine swivel point

- ℓ_α = distance from center of pressure in pitch plane to origin of body axis system (see Fig. 8)
- ℓ_{pi} = distance from hinge point of i^{th} pendulum to origin of body axis system (see Fig. 9)
- L = length of vehicle
- L_{pi} = length of i^{th} pendulum (see Fig. 9)
- L_α = aerodynamic load per unit angle of attack
- $m(\ell)$ = reduced mass per unit length along vehicle longitudinal axis;

$$\int_0^L m(\ell) d\ell = m_0$$
- m_0 = reduced mass of vehicle; $= m_T - \sum_i m_{pi}$
- m_{pi} = mass of i^{th} pendulum
- m_T = total mass of vehicle
- m_R = mass of rocket engine
- $M^{(i)}$ = generalized mass of i^{th} bending mode
- ΣM_x = total perturbation moment about pitch axis of vehicle
- $q^{(i)}$ = generalized coordinate of i^{th} bending mode
- $Q^{(i)}$ = generalized force (moment) of i^{th} bending mode in (pitch, yaw, roll) plane
- s = Laplace operator
- t = time
- T_c = control (gimballed) thrust
- T_s = ungimballed thrust
- $T_T = T_c + T_s \equiv$ total thrust
- T_L = load feedback torque
- U_0 = forward velocity of vehicle

U_0 = thrust acceleration = $(T_T - D)/m_T$

W_w = wind velocity parallel to Z' axis

w = perturbation velocity of vehicle parallel to Z' axis

α = perturbation angle of attack

γ = perturbation flight path angle; $= \alpha - \theta$

Γ_{pi} = pendulum angle (see Fig. 9)

δ = rocket engine deflection angle

δ_c = command signal to rocket engine

ζ_a = relative damping factor for accelerometer

$\zeta^{(i)}$ = relative damping ratio for i^{th} bending mode

ζ_{cn} = relative damping ratio for engine servo controller

ζ_R = relative damping coefficient for rate gyro

ζ_α = relative damping factor for angle-of-attack sensor

θ = perturbation attitude angle

θ_c = attitude command signal

θ_a = accelerometer signal

θ_α = angle of attack signal

θ_F = feedback signal

θ_{PG} = position gyro signal

θ_{RG} = rate gyro signal

μ_c = control moment coefficient; $= \frac{T_c \ell_c}{I_{yy}}$

μ_α = aerodynamic moment coefficient; $= \frac{L_\alpha \ell_\alpha}{I_{yy}}$

$\xi(\ell, t)$ = bending deflection

ρ = atmospheric density

$\sigma^{(i)}$ = negative slope of i^{th} bending mode in (pitch, yaw, roll) plane;

$$= \frac{-\partial \varphi^{(i)}_p}{\partial \ell}$$

τ_p = time constant of position gyro

$\varphi^{(i)}$ = normalized mode shape function for the i^{th} bending mode

ω_a = undamped natural frequency for accelerometer

ω_α = undamped natural frequency for angle of attack meter

ω_i = undamped natural frequency of the i^{th} bending mode

ω_{cn} = undamped natural frequency of the engine servo controller

ω_R = undamped natural frequency of the rate gyro

ω_{pi} = undamped natural frequency of the i^{th} pendulum

Assuming that the origin of the body axis system coincides with the mass center, the equations that describe the vehicle motion are summarized below. (See Fig. 8.)

Rigid Body

$$\frac{\dot{w}}{U_0} = \frac{\sum F_z}{m_0 U_0} + \dot{\theta} \quad (20)$$

$$I_{yy} \ddot{\theta} = \sum M_y \quad (21)$$

$$\alpha = \frac{w}{U_0} + \alpha_w \quad (22)$$

$$\alpha_w = -\frac{W_w}{U_0} \quad (23)$$

$$\gamma = \alpha - \theta \quad (24)$$

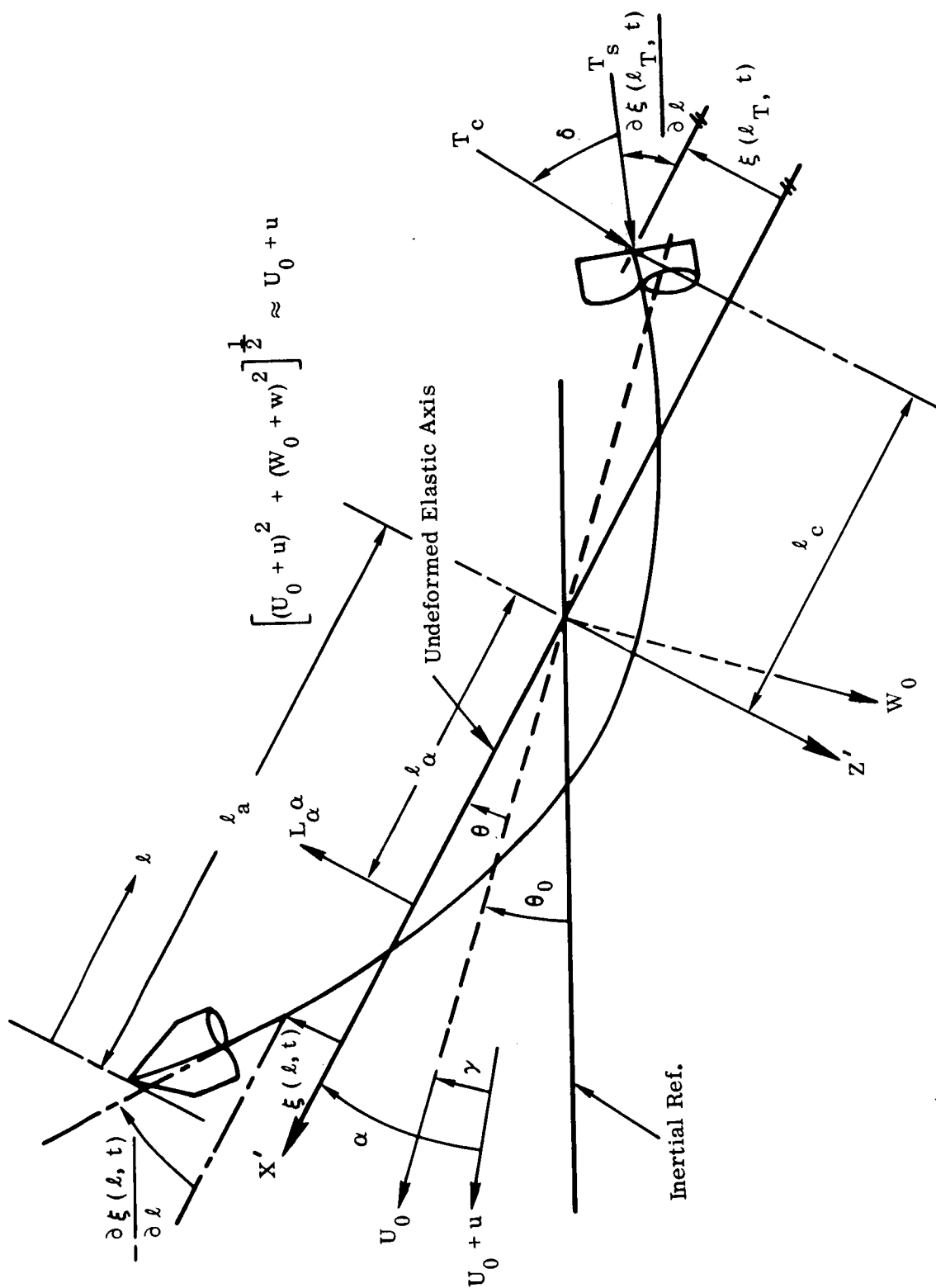


Figure 8. Elastic Vehicle in the Pitch Plane

$$\begin{aligned}
\Sigma F_z = & -m_T g \theta \cos \theta_0 + T_c \delta - T_T \sum_i q^{(i)} \sigma^{(i)}(\ell_T) - \frac{1}{2} \rho U_0^2 A_1 \\
& \times \left[\alpha \int_0^L \frac{\partial C_N(\ell)}{\partial \alpha} d\ell - \frac{\dot{\theta}}{U_0} \int_0^L \frac{\partial C_N(\ell)}{\partial \alpha} (\ell_a - \ell) d\ell \right. \\
& + \sum_i q^{(i)} \int_0^L \frac{\partial C_N(\ell)}{\partial \alpha} \sigma^{(i)}(\ell) d\ell - \sum_i \frac{\dot{q}^{(i)}}{U_0} \int_0^L \frac{\partial C_N(\ell)}{\partial \alpha} \varphi^{(i)}(\ell) d\ell \left. \right] \\
& + \sum_i m_{pi} \dot{U}_0 \Gamma_{pi} + m_R \left\{ \ell_R \ddot{\delta} + (\ell_c - \ell_R) \ddot{\theta} - \dot{w} + \dot{U}_0 \theta \right. \\
& \left. - \sum_i \left[\varphi^{(i)}(\ell_T) + \ell_R \sigma^{(i)}(\ell_T) \right] \ddot{q}^{(i)} \right\} \quad (25)
\end{aligned}$$

$$\begin{aligned}
\Sigma M_y = & \ell_c \left[T_c \delta - T_T \sum_i q^{(i)} \sigma^{(i)}(\ell_T) \right] - T_T \sum_i q^{(i)} \varphi^{(i)}(\ell_T) \\
& + \frac{1}{2} \rho U_0^2 A_2 \left[\alpha \int_0^L \frac{\partial C_N(\ell)}{\partial \alpha} (\ell_a - \ell) d\ell - \frac{\dot{\theta}}{U_0} \int_0^L \frac{\partial C_N(\ell)}{\partial \alpha} (\ell_a - \ell)^2 d\ell \right. \\
& + \sum_i q^{(i)} \int_0^L \frac{\partial C_N(\ell)}{\partial \alpha} (\ell_a - \ell) \sigma^{(i)}(\ell) d\ell - \sum_i \frac{\dot{q}^{(i)}}{U_0} \int_0^L \frac{\partial C_N(\ell)}{\partial \alpha} (\ell_a - \ell) \\
& \times \varphi^{(i)}(\ell) d\ell \left. \right] - \sum_i m_{pi} \ell_{pi} \dot{U}_0 \Gamma_{pi} + (I_R + m_R \ell_R \ell_c) \ddot{\delta} + m_R \ell_R \dot{U}_0 \delta \\
& - (I_R - m_R \ell_c^2) \ddot{\theta} - m_R (\ell_R + \ell_c) \dot{w} + m_R \ell_c \dot{U}_0 \theta \\
& - m_R \ell_R \dot{U}_0 \sum_i \sigma^{(i)}(\ell_T) q^{(i)} - \sum_i \left[m_R (\ell_R + \ell_c) \varphi^{(i)}(\ell_T) \right. \\
& \left. + (I_R + m_R \ell_R \ell_c) \sigma^{(i)}(\ell_T) \right] \ddot{q} \quad (26)
\end{aligned}$$

Sloshing (See Fig. 9)

$$\ddot{\Gamma}_{pi} + \omega_{pi}^2 \Gamma_{pi} = \frac{1}{L_{pi}} \left[U_0 \dot{\theta} - \dot{w} + \ddot{\theta} (\ell_{pi} - L_{pi}) + \sum_i \ddot{q}^{(i)} \varphi^{(i)}(\ell_{pi}) \right] \quad (27)$$

$$\omega_{pi}^2 = \frac{\dot{U}_0}{L_{pi}}$$

Bending

$$\xi(\ell, t) = \sum_i q^{(i)}(t) \varphi^{(i)}(\ell) \quad (28)$$

$$\ddot{q}^{(i)} + 2\zeta_i \omega_i \dot{q}^{(i)} + \omega_i^2 q^{(i)} = -\frac{Q^{(i)}}{M^{(i)}} \quad (29)$$

$$Q^{(i)} = \int_0^L \sum F_z \varphi^{(i)}(\ell) d\ell \quad (30)$$

\equiv generalized force for i^{th} bending mode

$$M^{(i)} = \int_0^L m(\ell) \left[\varphi^{(i)}(\ell) \right]^2 d\ell \quad (31)$$

\equiv generalized mass for i^{th} bending mode

$$\sigma^{(i)}(\ell) = -\frac{\partial \varphi^{(i)}(\ell)}{\partial \ell} \quad (32)$$

Electrohydraulic Actuator

$$\begin{aligned} & \left(s^3 + 2\zeta_c \omega_c s^2 + \omega_c^2 s + K_c \omega_c^2 \right) \delta \\ & = K_c \omega_c^2 \delta_c - \frac{1}{I_R} \left(s + 2\zeta_c \omega_c \right) T_L \end{aligned} \quad (33)$$

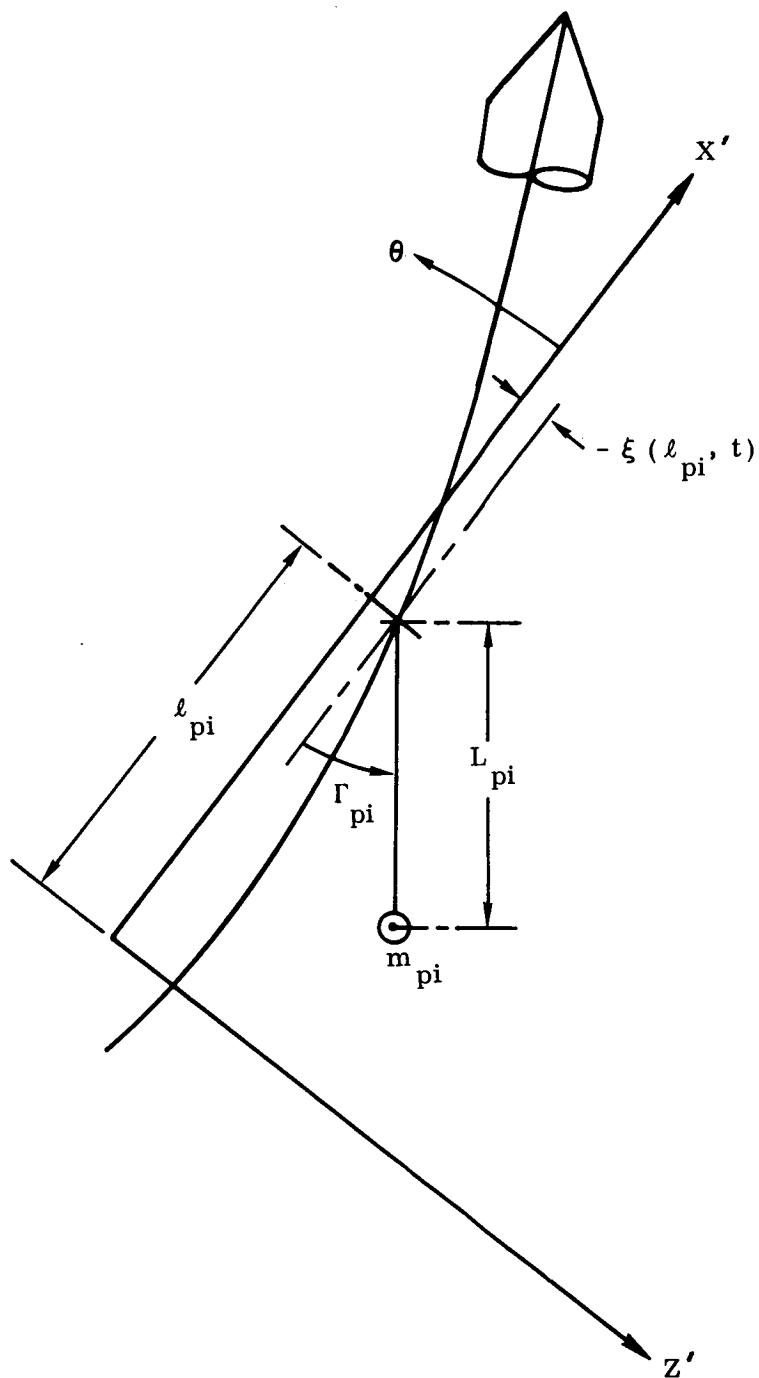


Figure 9. Schematic of Sloshing Pendulum, Pitch Plane

$$\begin{aligned}
T_L = & - \left(I_R - m_R \ell_c^2 \right) \ddot{\theta} - m_R \left(\ell_R + \ell_c \right) \dot{w} + m_R \ell_c \dot{U}_0 \theta \\
& - \sum_i \left[m_R \left(\ell_R + \ell_c \right) \varphi^{(i)} \left(\ell_T \right) + \left(I_R + m_R \ell_R \ell_c \right) \sigma^{(i)} \left(\ell_T \right) \right] \ddot{q}^{(i)} \\
& - m_R \ell_R \dot{U}_0 \sum_i \sigma^{(i)} \left(\ell_T \right) q^{(i)}
\end{aligned} \tag{34}$$

Feedback Signal

$$\theta_F = \theta_{RG} + \theta_{PG} + \theta_\alpha + \theta_a \tag{35}$$

Rate Gyro

$$\left(s^2 + 2\zeta_R \omega_R s + \omega_R^2 \right) \theta_{RG} = \omega_R^2 K_R s \left[\theta + \sum_i \sigma^{(i)} \left(\ell_G \right) q^{(i)} \right] \tag{36}$$

Position Gyro

$$\left(\tau_P s + 1 \right) \theta_{PG} = \theta + \sum_i \sigma^{(i)} \left(\ell_G \right) q^{(i)} \tag{37}$$

Accelerometer

$$\begin{aligned}
\left(s^2 + 2\zeta_a \omega_a s + \omega_a^2 \right) \theta_a = & \omega_a^2 K_a \left\{ \frac{\sum F_z}{m_T} - \ell_A \ddot{\theta} + \dot{U}_0 \theta \right. \\
& \left. - \sum_i \left[\varphi^{(i)} \left(\ell_A \right) \ddot{q}^{(i)} + \dot{U}_0 \sigma^{(i)} \left(\ell_A \right) q^{(i)} \right] \right\}
\end{aligned} \tag{38}$$

Angle of Attack Sensor

$$\left(s^2 + 2\zeta_\alpha \omega_\alpha s + \omega_\alpha^2 \right) \theta_\alpha = \omega_\alpha^2 K_\alpha \left[\alpha - \sum_i \sigma^{(i)} \left(\ell_m \right) q^{(i)} \right] \tag{39}$$

Engine Command Signal

$$\delta_c = K_A \left(\frac{K_I}{s} + 1 \right) (\theta_c - \theta_F) \tag{40}$$

The set of Eqs. (20) - (40) is a complete description of the short-period dynamics of the vehicle employing conventional autopilot control. These equations are characterized by the usual linearity assumptions and by the fact that inertial coupling between pitch, roll, and yaw is neglected. A complete six-degree-of-freedom formulation is contained in Ref. 1. Questions related to nonlinearities, stochastic effects, load relief, trajectories, etc., are treated in the companion monographs in this series.*

3.3 AUTOPILOT DESIGN

The autopilot design for a launch vehicle must take account of three main factors:

- a. Short-period stability.
- b. Aerodynamic loads.
- c. Compatability with guidance.

The latter usually implies that guidance commands in the form of thrust vector orientation are suitably translated into attitude (or attitude rate) commands to the control system. This problem is discussed briefly in Ref. 11. Compatability with guidance also implies that deviations from a reference trajectory are within tolerable bounds. In other words, the fuel expended in making guidance corrections should not exceed prescribed limits; otherwise, the payload (or mission) capability is impaired. This requirement generally conflicts with the need to limit aerodynamic loads, wherein the design philosophy is to let the vehicle "roll with the punch." Preliminary estimates of possible tradeoffs may be obtained by the methods described in Sec. 3.1. Means of reducing bending loads on the vehicle by using auxiliary feedback loops and manipulating autopilot gains are discussed in companion monographs in this series.**

In Secs. 3.3.1 - 3.3.3, the fundamental problem of designing an autopilot to stabilize the short-period motions of the vehicle is considered in detail. Having established the control system configuration in the light of these requirements, a complete, nonlinear, time-varying simulation is used to add whatever refinements are necessary from a loads or guidance point of view.

3.3.1 Dynamic Modes

Much of the literature on launch vehicle autopilots uses such terms as "quasi-normal modes," "artificially uncoupled modes," and "elastic and inertial coupling," without giving them a precise meaning. It would seem appropriate, therefore, to lay

*The complete list of monographs on Design Criteria is contained in Ref. 1.

**See Vol. III, part 2, "Load Relief," and part 10, "Response Studies."

some groundwork for the proper use of these terms. Basically, the vector matrix equation for any conservative dynamic system may be expressed as

$$M \ddot{x} + K x = f \quad (41)$$

The eigenvalues of the system are obtained from the determinant equation

$$|K - \omega^2 M| = 0 \quad (42)$$

yielding n eigenvalues, $\omega_1, \omega_2, \dots, \omega_n$, and n corresponding eigenvectors, v_1, v_2, \dots, v_n . The motion associated with a particular eigenvalue (frequency) is called a principal mode. By defining a new variable in accordance with

$$x = \sum_{r=1}^n c_r v_r \quad (43)$$

Eq. (41) reduces to the n equations**

$$\ddot{c}_r + \omega_r^2 c_r = \frac{v_r^T f}{v_r^T M v_r} \quad (44)$$

$$r = 1, 2, \dots, n$$

in which the c_r , called the normal coordinates, are uncoupled. The quantity $v_r^T f$ is termed the generalized force corresponding to the r^{th} mode, while $v_r^T M v_r$ is the generalized mass corresponding to the r^{th} mode.

In the usual method of analyzing the short-period motion of a launch vehicle, the bending modes are computed in terms of normal coordinates with the sloshing pendulums and rocket engines removed. Also, the sloshing modes are computed for a rigid vehicle. In this sense, we say that the bending and sloshing modes have been artificially uncoupled. When obtaining the equations of motion, however, this coupling is reintroduced via the forcing function terms. For example, looking at Eq. (29), we see that the generalized force introduces coupling with the other bending modes and the sloshing modes in accordance with Eq. (25). Depending on the manner in which these terms arise, we speak of aerodynamic or inertial coupling, etc.

As a result, it is not strictly valid to analyze a specific mode independently of the others in the system. However, when one mode is well separated in frequency from the others, the degree of coupling is minimal, and the general features of this

*Assuming that x is an n vector.

**Making use of the orthogonality properties of the eigenvectors, v_r .

mode may be analyzed independently. The refinements introduced by adding the coupling motions do not in general vitiate the qualitative dynamic features thus obtained. This is, therefore, a useful approach and has been widely used. It is basic to the discussions contained in the following sections.

3.3.1.1 Rigid Body

For purposes of a preliminary analysis, it is convenient to assume that the launch vehicle is completely rigid. The sloshing and engine inertia effects are removed by assuming that $m_R, m_{pi} \rightarrow 0$. In this case, Eqs. (25) and (26) reduce to

$$\Sigma F_z = -m_T g \theta \cos \theta_0 + T_c \delta - \frac{1}{2} \rho U_0^2 A_1 \left[\alpha \int_0^L \frac{\partial C_N(\ell)}{\partial \alpha} d\ell - \frac{\dot{\theta}}{U_0} \int_0^L \frac{\partial C_N(\ell)}{\partial \alpha} (\ell_a - \ell) d\ell \right]$$

$$\Sigma M_y = T_c \ell_c \delta + \frac{1}{2} \rho U_0^2 A_2 \left[\alpha \int_0^L \frac{\partial C_N(\ell)}{\partial \alpha} (\ell_a - \ell) d\ell - \frac{\dot{\theta}}{U_0} \int_0^L \frac{\partial C_N(\ell)}{\partial \alpha} (\ell_a - \ell)^2 d\ell \right]$$

The terms containing $\dot{\theta}/U_0$ are generally negligible compared with α . Consequently, if we write

$$L_\alpha = \frac{1}{2} \rho U_0^2 A_1 \int_0^L \frac{\partial C_N(\ell)}{\partial \alpha} d\ell \quad (45)$$

$$\ell_\alpha L_\alpha = \frac{1}{2} \rho U_0^2 A_2 \int_0^L \frac{\partial C_N(\ell)}{\partial \alpha} (\ell_a - \ell) d\ell \quad (46)$$

then the force and moment equations reduce to

$$\Sigma F_z = -m_T g \theta \cos \theta_0 + T_c \delta - L_\alpha \alpha \quad (47)$$

$$\Sigma M_y = T_c \ell_c \delta + L_\alpha \ell_\alpha \alpha \quad (48)$$

L_α is thus the aerodynamic load per unit angle of attack, and ℓ_α serves to locate the center of pressure. Eqs. (20) and (21) then take the form* (assuming $\alpha_w = 0$)

$$\dot{\alpha} = -\frac{g \cos \theta_0}{U_0} \theta + \frac{T_c}{m_T U_0} - \frac{L_\alpha}{m_T U_0} \alpha + \dot{\theta} \quad (49)$$

$$\ddot{\theta} = \mu_c \delta + \mu_\alpha \alpha \quad (50)$$

where

$$\mu_c = \frac{T_c \ell_c}{I_{yy}} \quad (51)$$

$$\mu_\alpha = \frac{L_\alpha \ell_\alpha}{I_{yy}} \quad (52)$$

Eliminating α between Eqs. (49) and (50), we obtain the transfer function relating θ to δ as follows.

$$\frac{\theta}{\delta} = \frac{\mu_c \left[s + \frac{L_\alpha}{m_T U_0} \left(1 + \frac{\ell_\alpha}{\ell_c} \right) \right]}{\left[s^3 + \frac{L_\alpha}{m_T U_0} s^2 - \mu_\alpha s + \frac{\mu_\alpha g \cos \theta_0}{U_0} \right]} \quad (53)$$

When ℓ_α is positive (center of pressure forward of the c.g.), μ_α is positive and it is immediately apparent that the vehicle is aerodynamically unstable.

In regions of negligible aerodynamic pressure, Eq. (53) reduces to

$$\frac{\theta}{\delta} = \frac{\mu_c}{s^2} \quad (54)$$

*Note that $m_T = m_0$ when there is no sloshing.

When the aerodynamic pressure is not negligible, the forward velocity, U_0 , is usually high enough that Eq. (53) is represented with sufficient accuracy by

$$\frac{\theta}{\delta} = \frac{\mu_c}{s^2 - \mu_\alpha} \quad (55)$$

For example, using the data of Table 1 (with $\theta_0 = 80$ deg), Eq. (53) becomes

$$\frac{\theta}{\delta} = \frac{\mu_c (s + 0.0678)}{(s - 0.0042) (s^2 + 0.0354 s - 3.75)}$$

The dipole at the origin and the small damping term in the quadratic evidently have little effect on the response characteristics of θ . Approximation (55) is therefore very good.

Designing an autopilot for the simplified system dynamics represented by Eq. (55) is not particularly challenging. An appropriate control system configuration is shown in Fig. 10. Here a simple first-order lag was used to simulate the electrohydraulic servoactuator, and gyro instrumentation dynamics were neglected. The characteristic equation for this system is found to be

$$s^3 + K_c s^2 + (K_A K_c K_R \mu_c - \mu_\alpha) s + K_c (K_A \mu_c - \mu_\alpha) = 0 \quad (56)$$

and Routh's criterion shows that stability is ensured if the relations

$$K_A \mu_c > \mu_\alpha \quad (57)$$

$$\frac{1}{K_R} < K_c \quad (58)$$

are both satisfied. The first of these is basically a static stability criterion; it states that the restoring moment per unit attitude change must be greater than the overturning moment. The second is a dynamic stability requirement; it stipulates that the lead from the rate gyro must be greater than the lag from the actuator. A root locus diagram for this system is shown in Fig. 11. Diagrams A and B differ only in the relative values of μ_α and K_R . In either event, $K_A = \mu_\alpha / \mu_c$ is the gain for neutral stability. It is also apparent that an indefinite increase in K_A does not lead to instability. This conclusion is valid only for the simplified case considered here. The addition of lags due to filtering and higher-order dynamic effects will set an upper limit on K_A for stability.

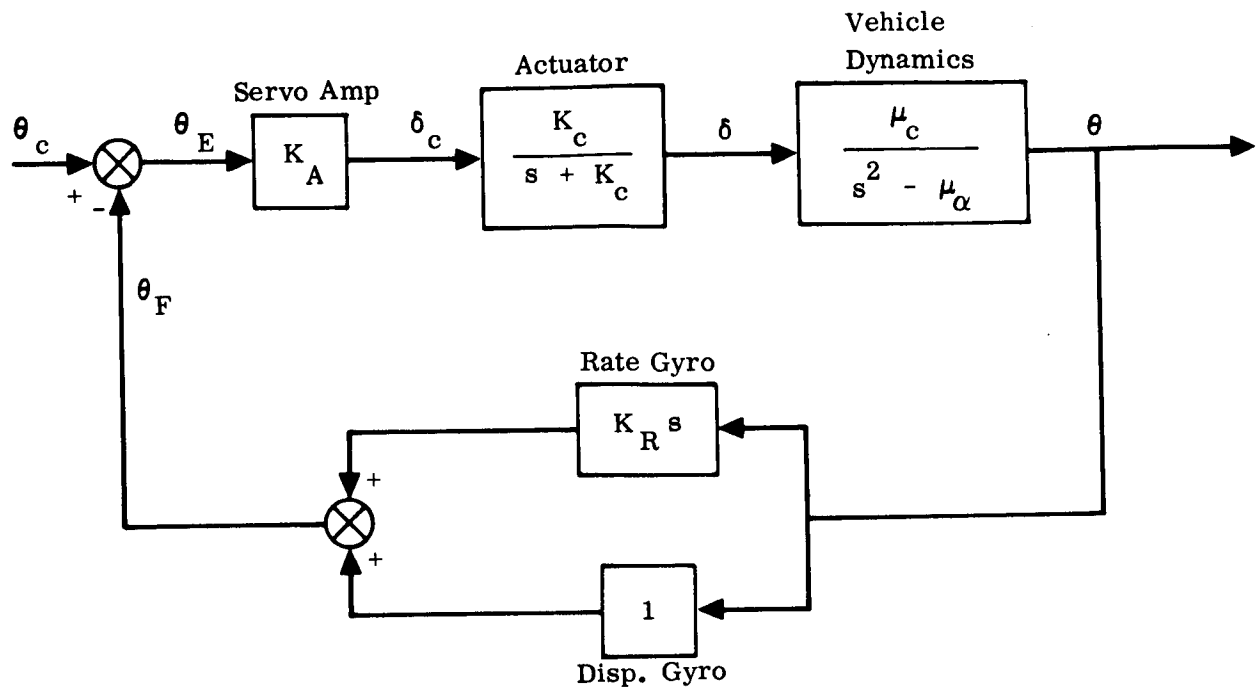


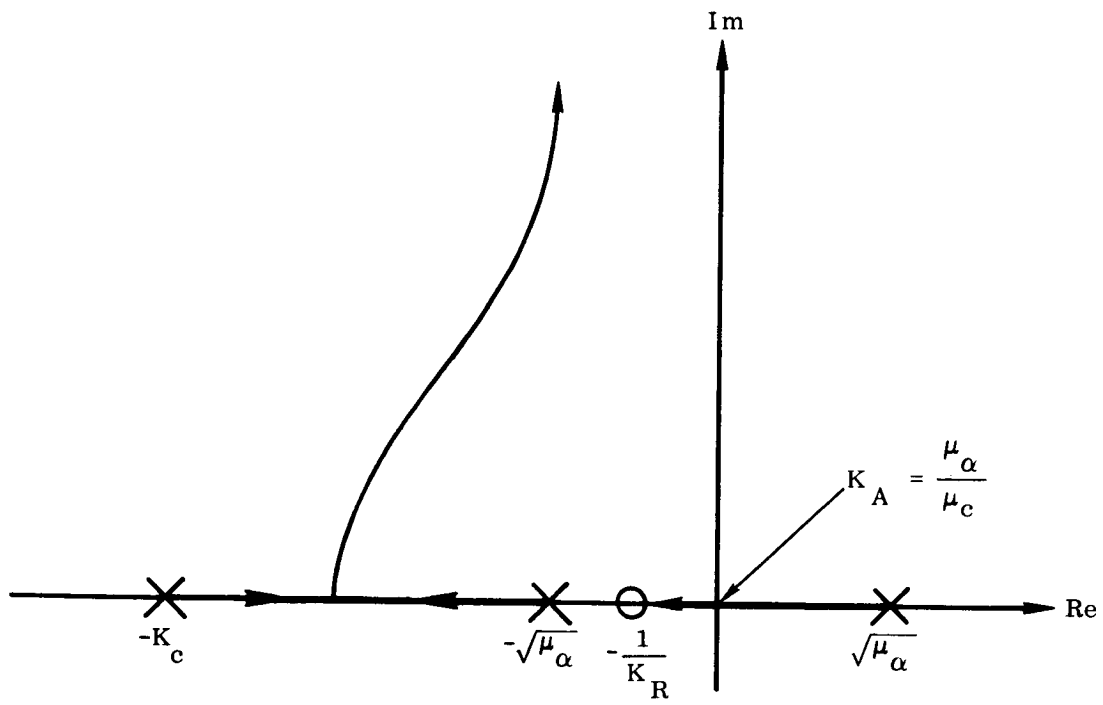
Figure 10. Autopilot for Simplified Rigid Body

For example, simple passive filtering is often employed to stabilize the bending modes. Figure 12 shows how a simple passive filter influences the rigid body mode. The filter introduces a real pole on the imaginary axis in the s plane. This has the effect of bending the root locus into the right-half plane for sufficiently high values of open-loop gain. Adding still another passive filter yields the root locus shown in Fig. 13. The deterioration in gain and phase margin is quite apparent. Consequently, the use of passive filters to suppress bending mode signals has definite limitations.

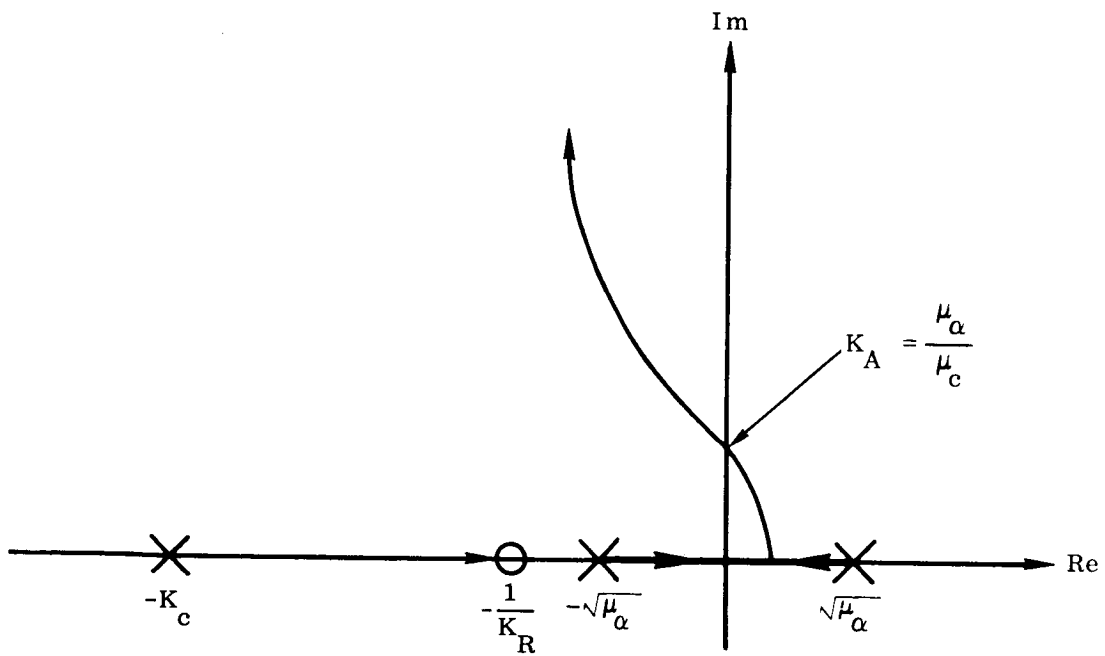
Again considering the autopilot schematic of Fig. 10, it is found that the steady-state response of the system to a unit step command, θ_c , is given by

$$\theta_{ss} = \frac{1}{1 - \frac{\mu_\alpha}{\mu_c K_A}} \quad (59)$$

Obviously, the higher the value of K_A , the smaller the steady-state error. Since there are definite upper limits to permissible values of K_A , one must seek to null the error by other means. This may, in fact, be done by adding integral control in the forward loop such that



(A)



(B)

Figure 11. Root Locus for Simplified Autopilot

$$\frac{\theta_F}{\theta_E} = \frac{K_0 (s + \frac{1}{K_R})}{s^2 (s + K_C) (s + \frac{1}{\tau})}$$

$$K_0 = \frac{K_A K_C K_R \mu_c}{\tau}$$

$$K_R = \frac{1}{3}$$

$$K_C = 15$$

$$\tau = 0.04$$

Numbers on root locus
denote values of $K_A \mu_c$

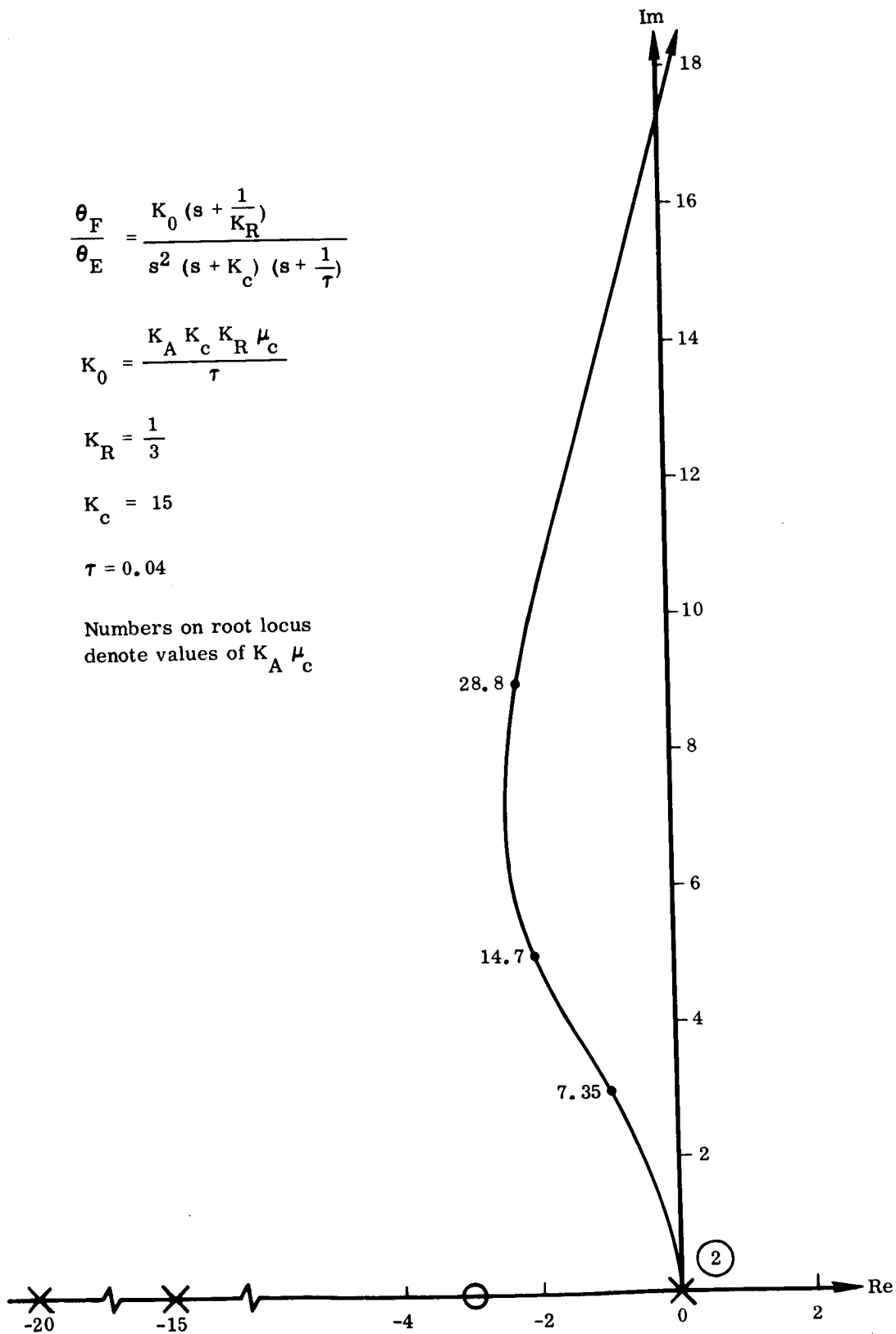


Figure 12. Root Locus Showing Influence of One Lag Filter

$$\frac{\theta_F}{\theta_E} = \frac{K_0 (s + \frac{1}{K_R})}{s^2 (s + K_c) (s + \frac{1}{\tau})^2}$$

$$K_0 = \frac{K_A K_c K_R \mu_c}{\tau^2}$$

$$K_R = \frac{1}{3}$$

$$K_c = 15$$

$$\tau = 0.04$$

Numbers on root locus
denote values of $K_A \mu_c$

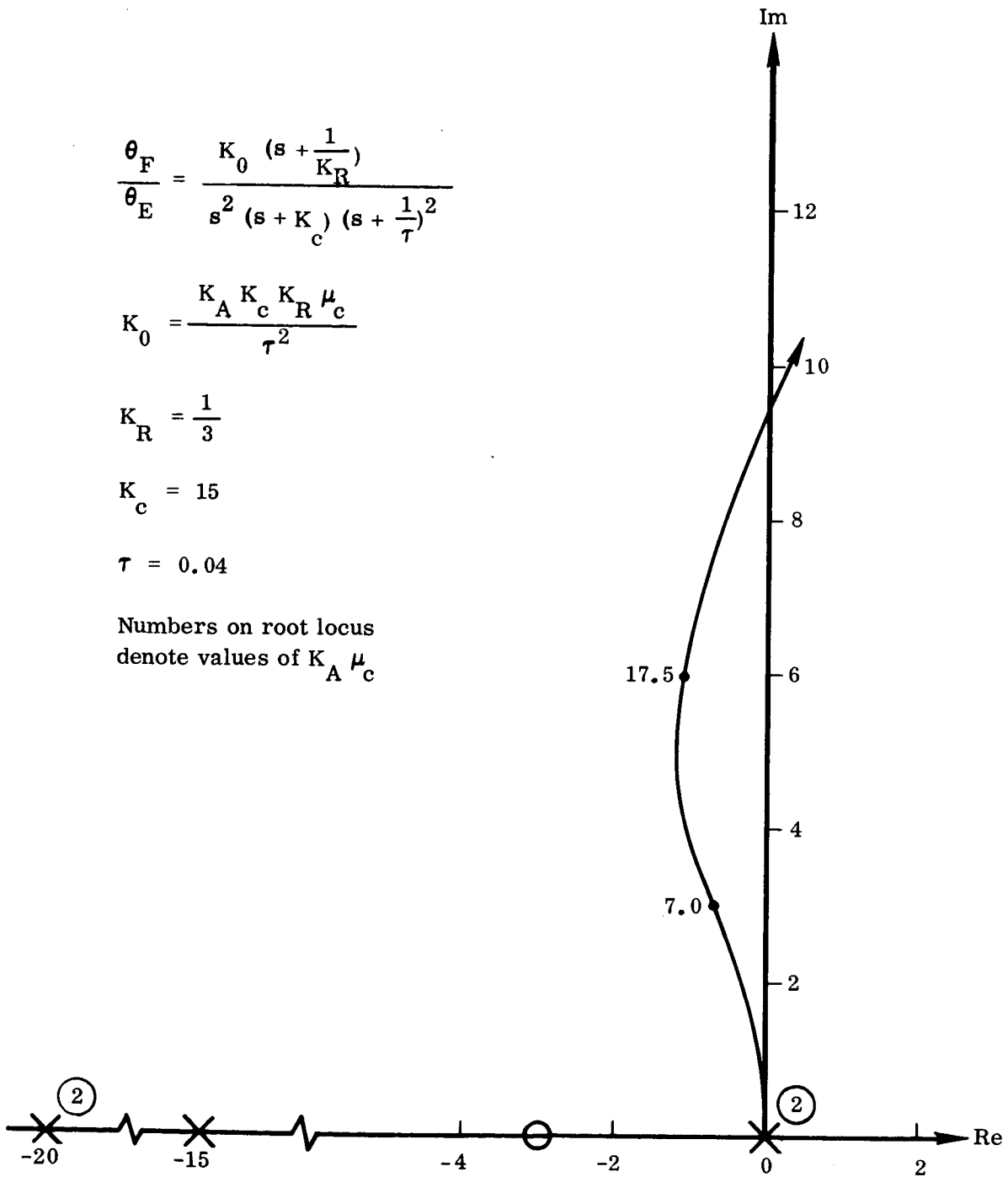


Figure 13. Root Locus Showing Influence of Two Lag Filters

$$\delta_c = K_A \left(\frac{K_I}{s} + 1 \right) \theta_E \quad (60)$$

It is easily verified that this results in zero steady-state error for all position inputs.*

In studying the simplified short-period dynamics of the vehicle, it is often convenient to assume that $\alpha \approx \theta$. This may be justified as follows. From Eqs. (49) and (50), (assuming for simplicity that $\theta_0 = 90$ deg) we find

$$\frac{\alpha}{\theta} = \frac{\tau_1 s (\tau_2 s + 1)}{(\tau_1 s + 1)} \quad (61)$$

where

$$\tau_1 = \frac{m_T U_0}{L_\alpha \left(1 + \frac{l_\alpha}{l_c} \right)}$$

$$\tau_2 = \frac{T_c}{m_T U_0 \mu_c}$$

A Bode plot of this transfer function is shown in Fig. 14. Using the data for a typical large booster vehicle (Table 1), it is found that $\tau_1 = 15$ and $\tau_2 = 0.01$. Thus, in the frequency range 0.067 - 100 rad/sec, $\theta = \alpha$ is a good approximation for this class of vehicle. This is equivalent to assuming that the change in flight path angle is negligible compared with the perturbations in θ (or α).

With this approximation, a gust input is represented by the simplified autopilot schematic of Fig. 15. It is readily found that

$$\frac{\theta}{\theta_w} = \frac{(s^2 - \mu_\alpha)(s + K_c)}{s^3 + K_c s^2 + (K_A K_c K_R \mu_c - \mu_\alpha) s + K_c (K_A \mu_c - \mu_\alpha)} \quad (62)$$

*In the usual terminology of feedback control, the system is now a Type 1.

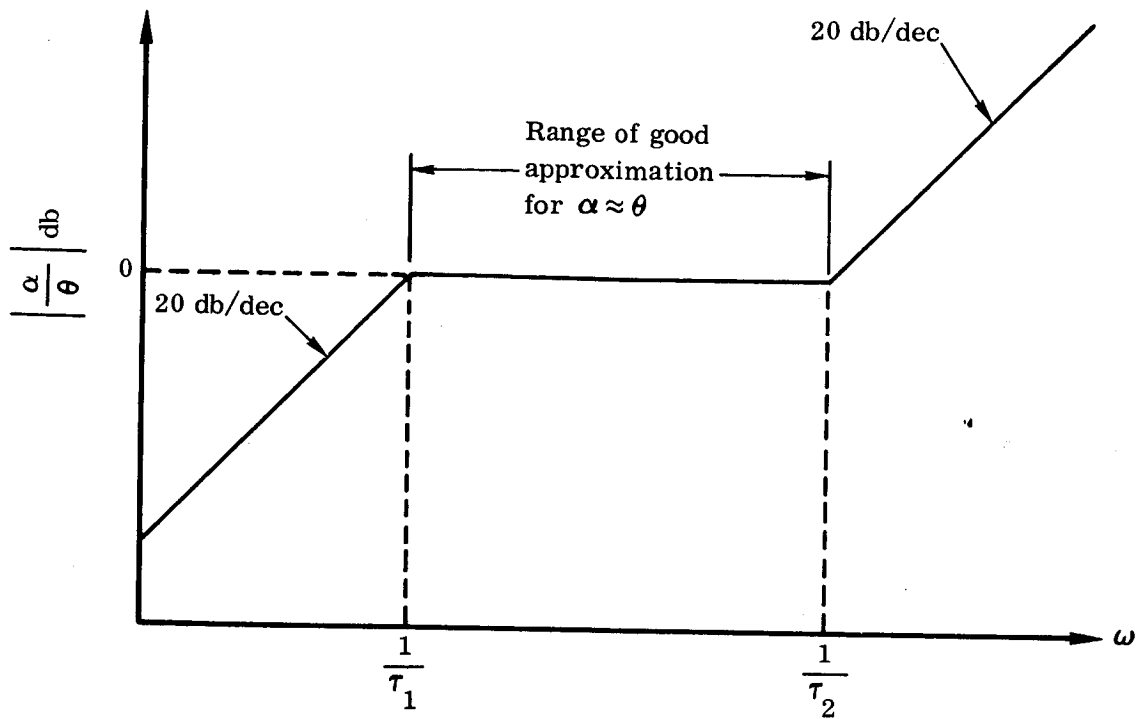


Figure 14. Bode Plot for Eq. (61)

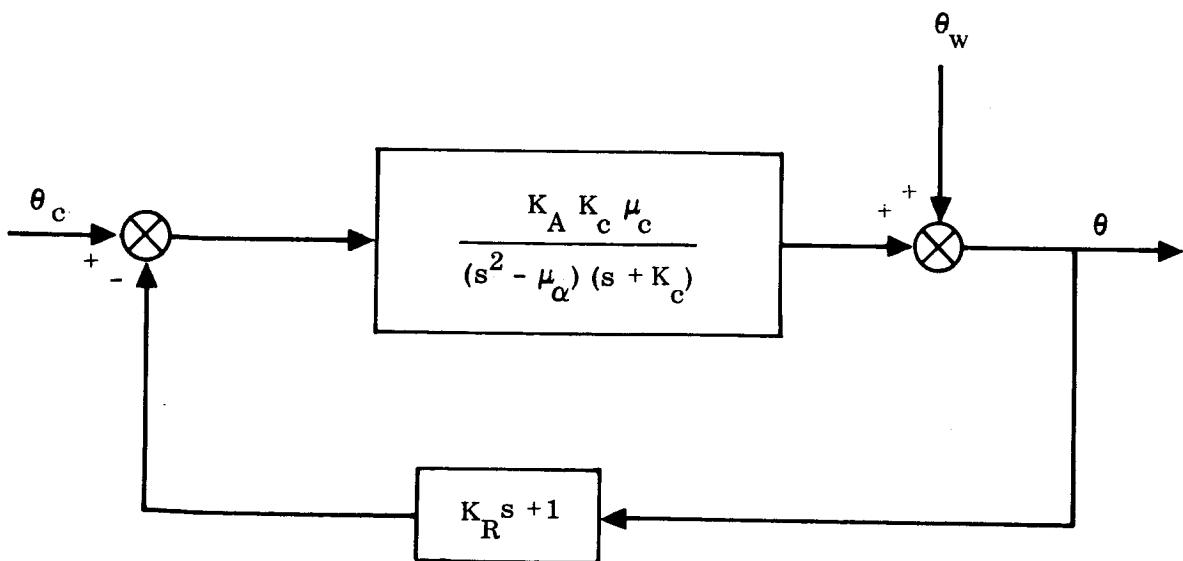


Figure 15. Configuration for Disturbance Input

It should be noted that the closed-loop poles in the above transfer function may be obtained from a root locus such as Fig. 11, and these are identical to the closed-loop poles for θ/θ_c . However,

$$\frac{\theta}{\theta_c} = \frac{K_A K_c \mu_c}{s^3 + K_c s^2 + (K_A K_c K_R \mu_c - \mu_\alpha) s + K_c (K_A \mu_c - \mu_\alpha)} \quad (63)$$

In other words, the zeros in the gust response make it differ from the command input response. This has the effect of decreasing the response time and tending to make the response more oscillatory.* An important measure of performance quality is the maximum overshoot in response to a disturbance input. Some crude "order-of-magnitude" values may be obtained as follows.

Substituting the numerical values of Table 1 with $K_A = 2$, Eq. (62) becomes

$$\frac{\theta}{\theta_w} = \frac{(s^2 - 3.75)(s + 15)}{(s + 11.07)(s^2 + 3.93s + 7.22)} \quad (64)$$

In computing the time response of the fundamental mode, which has a frequency on the order of 2.5 rad/sec, the zero at -15 effectively cancels the pole at -11.07. Consequently, Eq. (64) may be approximated by

$$\frac{\theta}{\theta_w} = \frac{(s^2 + c)}{[(s + a)^2 + b^2]} \quad (65)$$

$$a = 1.965$$

$$b = 1.83$$

$$c = -3.75$$

If now we take θ_w to be a unit step input, then

$$\theta(t) = \frac{c}{\beta_0^2} + \frac{1}{b\beta_0} \left[(a^2 - b^2 + c)^2 + 4a^2b^2 \right]^{\frac{1}{2}} e^{-at} \sin(bt + \psi) \quad (66)$$

where

$$\beta_0^2 = a^2 + b^2$$

*A detailed discussion of this condition is contained in Sec. 3.1.3 of Vol. II, part 1, "Linear Systems."

$$\psi = \tan^{-1} \left(\frac{-2ab}{a^2 - b^2 + c} \right) - \tan^{-1} \left(\frac{b}{-a} \right)$$

It is readily found that $\theta(t)$ is a maximum when

$$t = \frac{1}{b} \left[\tan^{-1} \left(\frac{b}{a} \right) - \psi \right]$$

Using the given numerical values, we find that*

$$\theta(t)_{\max} = -0.648$$

and occurs at $t = 1.09$ sec. The final steady-state value is

$$\theta_{ss} = -0.52$$

which indicates about a 25-percent overshoot. For μ_α negative (aerodynamically stable vehicle) the steady-state attitude is positive, and the percent overshoot is almost negligible for the data used here. Naturally, these results must be interpreted with due regard for the approximations involved.

If integral control is used in the forward loop,** the closed-loop transfer function becomes

$$\frac{\theta}{\theta_w} = \frac{s(s^2 - \mu_\alpha)s + K_c}{s(s^2 - \mu_\alpha)(s + K_c) + K_A K_c K_R \mu_c (s + K_I) \left(s + \frac{1}{K_R}\right)} \quad (67)$$

from which it is evident that the steady-state value is zero for a step input.

3.3.1.2 Fuel Sloshing

The forces and moments produced by sloshing of the liquid fuel may be duplicated by an equivalent mass and pendulum whose parameters depend on tank shape, liquid level, etc. Since a derivation of this result is not available in the open literature, a complete analysis for one simple case is given in Appendix B.

* $\psi = 1.90$ rad; $\beta_0 = 2.69$.

**See Eq. (60).

For purposes of autopilot analysis, it is assumed that the appropriate mechanical (pendulum) parameters are given. Retaining the simplified rigid-body approximations of Sec. 3.3.1.1, the appropriate equations of motion, which include the effects of sloshing, may be expressed as

$$\dot{w} - U_0 \dot{\theta} = \frac{\Sigma F_z}{m_0} \quad (68)$$

$$\ddot{\theta} = \frac{\Sigma M_y}{I_{yy}} \quad (69)$$

$$\ddot{\Gamma}_{pi} = \frac{1}{L_{pi}} \left[-\frac{\Sigma F_z}{m_0} + \frac{(\ell_{pi} - L_{pi})}{I_{yy}} \Sigma M_y - \dot{U}_0 \Gamma_{pi} \right] \quad (70)$$

$$\Sigma F_z = T_c \delta - L_\alpha \alpha + \Sigma_j m_{pj} \dot{U}_0 \Gamma_{pj} \quad (71)$$

$$\Sigma M_y = T_c \ell_c \delta + L_\alpha \ell_\alpha \alpha - \Sigma_j m_{pj} \ell_{pj} \dot{U}_0 \Gamma_{pj} \quad (72)$$

Making use of the approximation

$$\alpha \approx \theta \quad (73)$$

the above equations lead to

$$\ddot{\theta} = \mu_c \delta + \mu_\alpha \theta - \Sigma_j \mu_{pj} \Gamma_{pj} \quad (74)$$

$$\begin{aligned} \ddot{\Gamma}_{pi} = \frac{1}{L_{pi}} \left[-\frac{T_c}{m_0} \delta + \frac{L_\alpha}{m_0} \theta - \Sigma_j \frac{m_{pj} \dot{U}_0}{m_0} \Gamma_{pj} \right. \\ \left. + \frac{(\ell_{pi} - L_{pi})}{I_{yy}} \left(T_c \ell_c \delta + L_\alpha \ell_\alpha \theta \right) - \Sigma_j m_{pj} \ell_{pj} \dot{U}_0 \Gamma_{pj} - \dot{U}_0 \Gamma_{pi} \right] \end{aligned} \quad (75)$$

where μ_c and μ_α are defined by Eqs. (51) and (52) respectively, and

$$\mu_{pj} = \frac{m_{pj} \ell_{pj} \dot{U}_0}{I_{yy}} \quad (76)$$

In order to obtain some insight into the influence of sloshing, some further approximations may be introduced. First of all, it is generally true that sloshing effects do not become significant until the launch vehicle is well above the regions of maximum dynamic pressure. This is because liquid sloshing does not become appreciable until the liquid level is relatively low in the tank. When this happens, the vehicle is usually well above the sensible atmosphere. Also, in order to exhibit the problem in its simplest form, it will be assumed that there is only one fuel tank (and hence only one slosh pendulum), in which case the equations for θ and Γ reduce to

$$\ddot{\theta} = \mu_c \delta - \mu_p \Gamma \quad (77)$$

$$\begin{aligned} \ddot{\Gamma} = & -\frac{1}{L_p} \left[\frac{T_c}{m_0} - (\ell_p - L_p) \mu_c \right] \delta - \frac{1}{L_p} \left[\left(1 + \frac{m_p}{m_0} \right) \dot{U}_0 \right. \\ & \left. + (\ell_p - L_p) \mu_p \right] \Gamma \end{aligned} \quad (78)$$

Eliminating Γ between these equations, we find

$$\frac{\theta}{\delta} = \frac{\mu_c (s^2 + \omega_r^2)}{s^2 (s^2 + \omega_p^2)} \quad (79)$$

where

$$\omega_p^2 = \frac{1}{L_p} \left[\left(1 + \frac{m_p}{m_0} \right) \dot{U}_0 + (\ell_p - L_p) \mu_p \right] \quad (80)$$

$$\omega_r^2 = \omega_p^2 - \frac{\mu_p}{L_p} \left(\ell_p - L_p - \frac{r^2}{\ell_c} \right) \quad (81)$$

$$r^2 = \frac{I_{yy}}{m_0} \quad (82)$$

The autopilot configuration is as shown in Fig. 10, except that the vehicle dynamics are now represented by the transfer function of Eq. (79). Fig. 16 shows the location of the poles and zeros of the open-loop transfer function for this case. The effect of the sloshing pendulum is represented by the pole-zero pair on the imaginary axis.

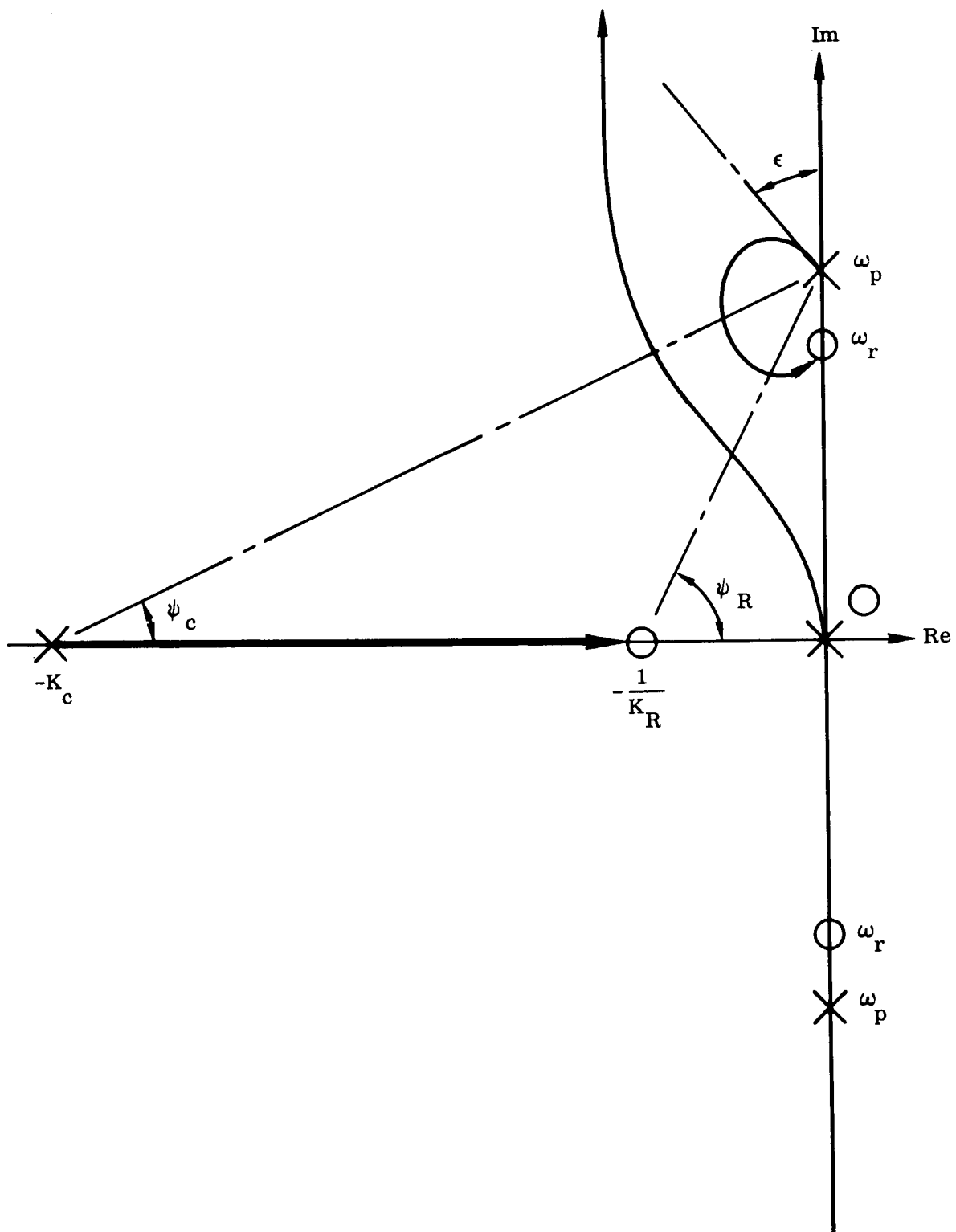


Figure 16. Pole-zero Configuration for Rigid Body and One Slosh Dipole

Some overall features of the stability problem may now be quickly ascertained. In the case shown in Fig. 16, the slosh pole is above the slosh zero ($\omega_p > \omega_r$). As a result, the angle of departure of the slosh pole is into the left-half plane, and therefore the system is stable. In fact, angle ϵ of Fig. 16 is given by

$$\epsilon = \psi_R - \psi_c$$

whenever $\omega_p > \omega_r$. For the case when $\omega_p < \omega_r$,

$$\epsilon = (\psi_R - \psi_c) + 180 \text{ deg}$$

Therefore, as long as $K_c K_R > 1$, the system is stable if $\omega_p > \omega_r$.

We now examine the physical significance of this result. From Eq. (81), we note that $\omega_p > \omega_r$ if

$$\frac{\mu_p}{L_p} \left(\ell_p - L_p - \frac{r^2}{\ell_c} \right) > 0 \quad (83)$$

If the pendulum hinge point is below the vehicle c.g. ($\ell_p < 0$ and $\mu_p < 0$), the above inequality is always satisfied and the system is stable. When the pendulum hinge point is above the vehicle c.g., two cases must be distinguished. For $\ell_p > 0$ and

$$\left(\ell_p - L_p \right) > \frac{r^2}{\ell_c} \quad (84)$$

inequality (83) is still satisfied, and therefore the system is stable. However, in the case

$$\left(\ell_p - L_p \right) < \frac{r^2}{\ell_c}, \quad \ell_c > 0 \quad (85)$$

inequality (83) is not satisfied, and, in fact, it follows that $\omega_r > \omega_p$. This is therefore the unstable condition.

The point on the vehicle a distance r^2/ℓ_c forward of the c.g. is the "center of percussion" for the vehicle. Consequently, if the pendulum hinge point is forward of the c.g., the pendulous mass must "straddle" the center of percussion in order for the motion to be stable.

When there are several fuel tanks on the vehicle (and therefore several slosh pendulums), the algebra involved in calculating the θ/δ transfer function becomes enormously complicated. However, it may be shown⁽⁸⁾ that the rules derived above remain valid for any number of pendulums. A number of considerations limit the range of usefulness of these rules. First of all, for high slosh frequencies, the additional phase lag introduced by the actuator and instrumentation dynamics must be taken into account. This will, of course, modify the angle of departure from the slosh poles, and the rules given above may not apply. Second, it must be remembered that aerodynamic effects were neglected, and in some instances this may vitiate the results. Also, it was assumed that there was zero slosh damping. In reality, there is always a small amount of damping due to the wiping action of the liquid against the tank wall. The pole-zero configuration in this case is shown in Fig. 17 (for a two-tank vehicle). The presence of slosh damping serves to bring the slosh dipole into the left-half s plane such that a locus that would otherwise be in the right-half plane is now completely contained within the left-half plane. Normally, the inherent damping due to wall friction is very small, and additional damping is introduced by mechanical baffles spaced at appropriate intervals along the tank wall. Since the slosh pole-zero pairs are normally very close to one another, any unstable oscillation would build up very slowly. As a result, annular baffles spaced at moderate intervals would be sufficient to damp out any unstable oscillation before it grew to unacceptable proportions.

An unstable slosh condition could be made stable by appropriate filtering. For example, in Fig. 18, the slosh zero is above the slosh pole ($\omega_z > \omega_p$), but the additional filtering, represented by the real poles at $-1/\tau_1$ and $-1/\tau_2$, brings the departure angle at the slosh pole into the left-half plane. However, the deterioration in rigid-body response (lower gain and phase margins) is generally unacceptable.

Finally, it should be noted that the slosh parameters (hinge point, pendulum mass and length) are a function of fluid level and therefore vary with flight time. For this reason, a complete design validation requires a full nonlinear, time-varying computer simulation.

3.3.1.3 Engine Inertia

The influence of engine inertia on the dynamic properties of a simplified autopilot may best be displayed by including the $\ddot{\delta}$ term in the pitching moment equation*; viz.,

$$I_{yy} \ddot{\theta} = T_c l_c \ddot{\delta} + L_\alpha l_\alpha \theta + m_R l_R l_c \ddot{\delta}$$

*Strictly speaking, the added term is of the form $(I_R + m_R l_R l_c) \ddot{\delta}$. However, quantity $m_R l_R l_c$ is generally much greater than I_R . We have also used the $\alpha \approx \theta$ approximation.

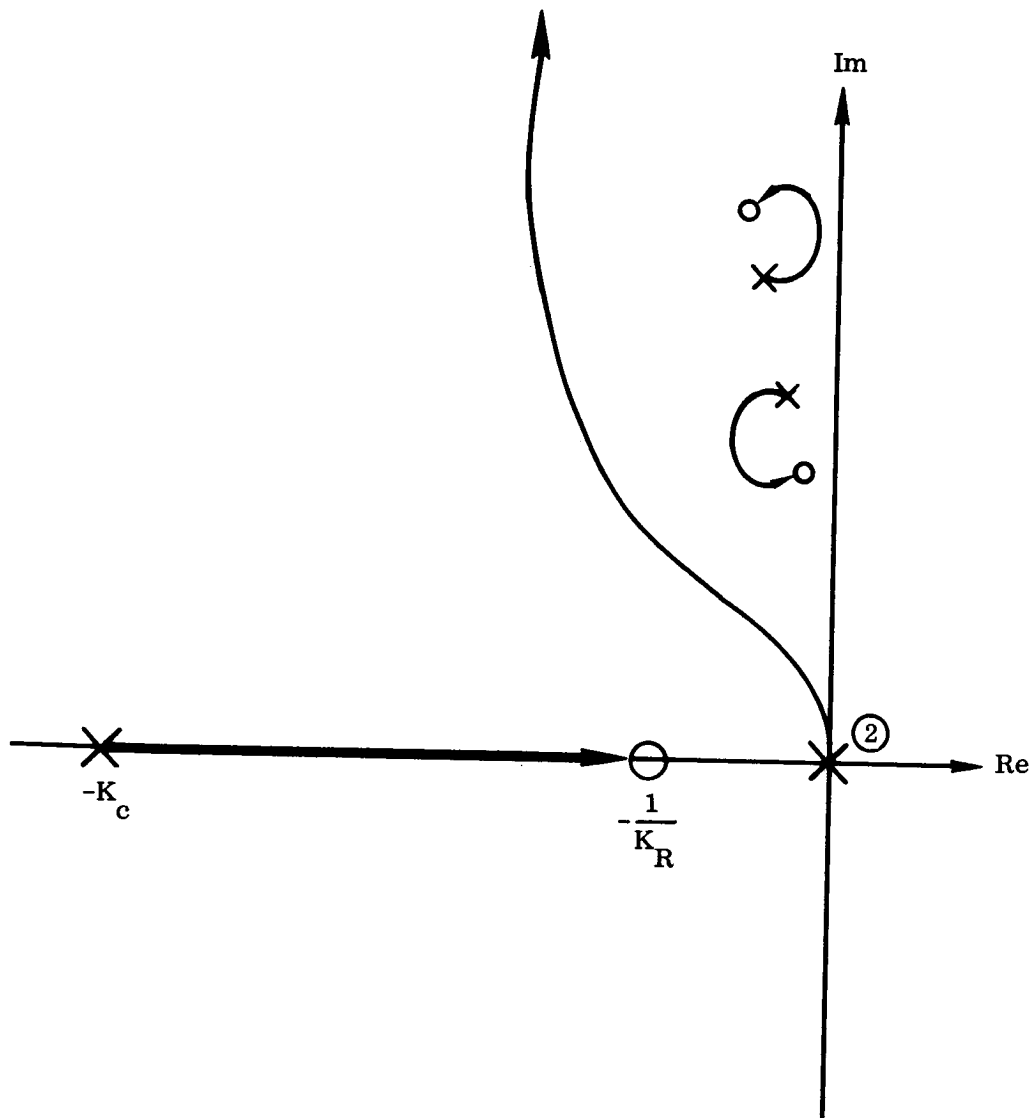


Figure 17. Root Loci Showing Influence of Slosh Damping

or, in transfer function form

$$\frac{\theta}{\delta} = \mu_c \frac{m_R \ell_R}{T_c} \frac{\left(s^2 + \frac{T_c}{m_R \ell_R} \right)}{\left(s^2 - \mu_\alpha \right)} \quad (86)$$

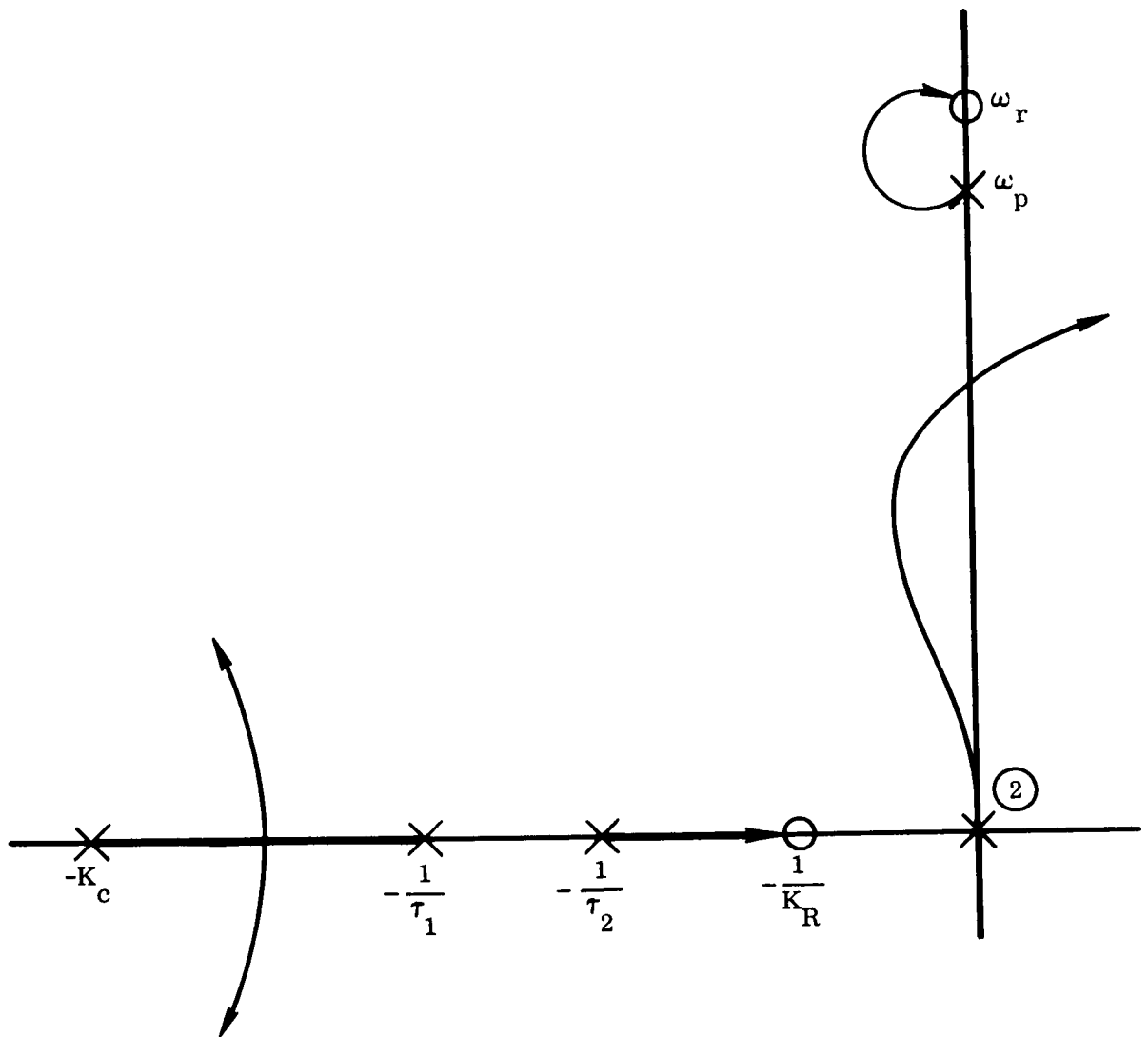


Figure 18. Sloop Stabilization by Passive Filtering

Using this to represent the vehicle dynamics in the simplified autopilot schematic of Fig. 10, the corresponding root locus appears as shown in Fig. 19. The engine inertia effect manifests itself in the presence of a pair of zeros on the imaginary axis. Therefore, the closed-loop frequency for the system is always less than $\sqrt{T_c/m_R l_R}$, no matter how high the gain. Quantity $\sqrt{T_c/m_R l_R}$ is often referred to as the "tail wags dog" (TWD) zero. It is equal to the frequency at which the transverse inertia forces resulting from the gimbaling of the rocket engine cancel the thrust forces due to the rocket angular deflection.

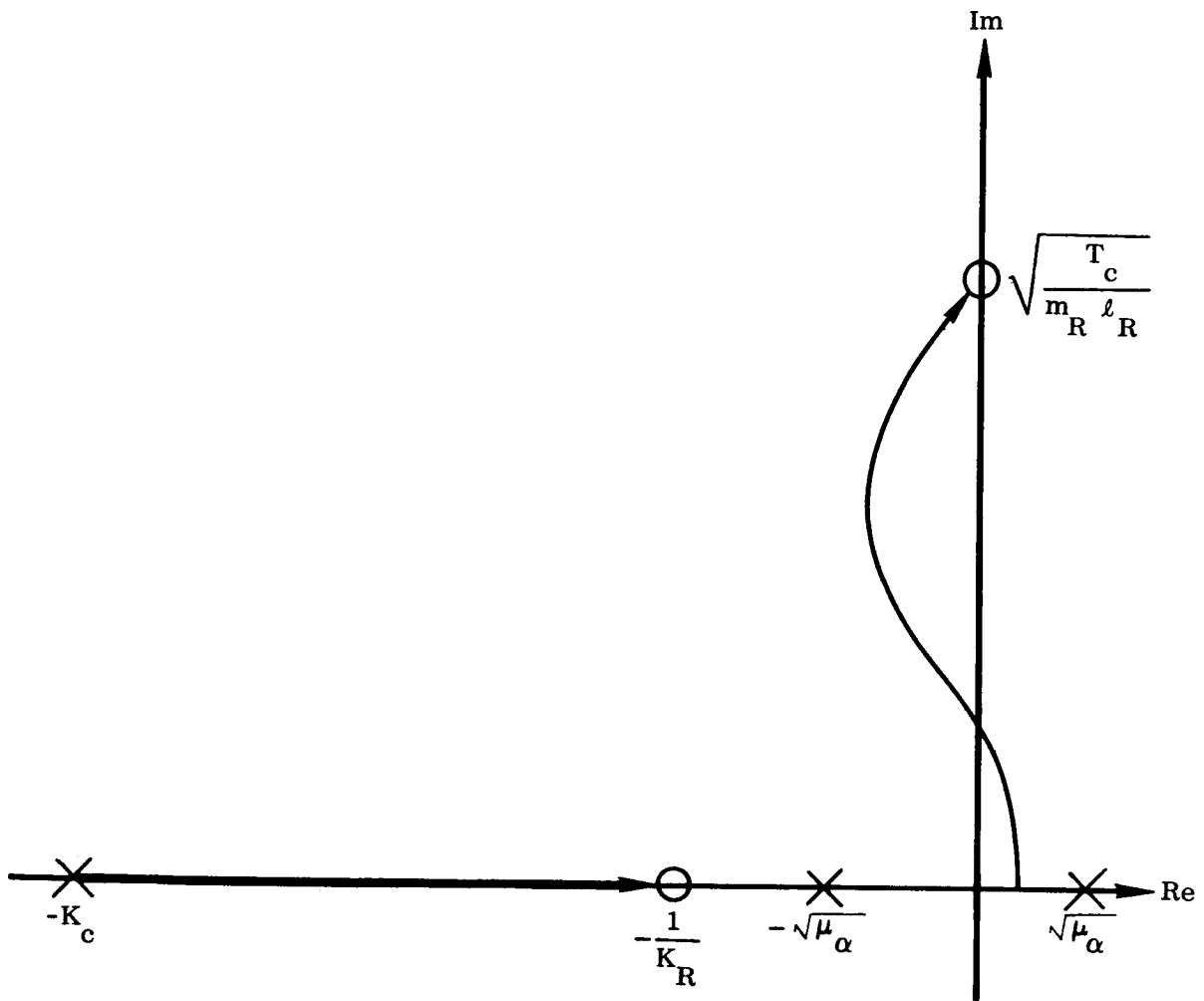


Figure 19. Root Locus of Simplified Autopilot Showing Influence of Engine Inertia

This effect is seldom important for the rigid-body modes in the current generation of launch vehicles. It could conceivably be significant for vehicles where the rocket engine mass is very large. In such cases, a TWD zero of the same order of magnitude as the control frequencies could result and could seriously compromise the control problem. Generally, however, the TWD zero is most important in the bending stability problem. This question, which is the crucial one in the design of launch vehicle autopilots, is considered next.

3.3.1.4 Vehicle Flexibility

The flexibility of the vehicle enters the control problem primarily because the sensing instrumentation (gyros) picks up not only the rigid-body motion but also the local elastic distortions. Theoretically, because the vehicle is a continuous body, the elastic motion is described by a system with an infinite number of degrees of freedom (bending modes). In practice, either a truncation of the infinite series or a lumped mass model is used to yield a system with a finite number of elastic modes. The number of modes that are significant in a given situation depends on the bandwidth of the primary dynamic modes. The high-frequency-attenuation properties of the basic system transfer function, together with inherent structural damping, is sufficient to dismiss the higher elastic modes from further consideration. In the current generation of launch vehicles, five elastic modes are usually sufficient to describe the significant dynamic properties of the vehicle. Often no more than three modes are needed.

How vehicle flexibility influences the autopilot design can be demonstrated by assuming that only one bending mode is significant. In this case, the added degree of freedom is described by Eq. (29). The generalized force, $Q^{(i)}$, is a function of the normal forces on the vehicle, ΣF_z , and indicates how a particular bending mode is coupled to all the other dynamic modes of the system. Considering only first-order effects, the i^{th} bending mode is excited primarily by rocket engine deflection. Thus we write

$$Q^{(i)} = \int_0^L \left[T_c \delta + m_R \ell_R \ddot{\delta} \right] \varphi^{(i)}(\ell) d\ell$$

$$= (T_c \delta + m_R \ell_R \ddot{\delta}) \varphi^{(i)}(\ell_T)$$

since the point of application of these forces is at the rocket engine swivel point, $\ell = \ell_T$. However, the bending modes are generally normalized at $\ell = \ell_T$ such that $\varphi^{(i)}(\ell_T)$ is always unity. Eq (29) therefore becomes

$$\left(s^2 + 2 \zeta_i \omega_i s + \omega_i^2 \right) q^{(i)} = - \frac{1}{M^{(i)}} \left(m_R \ell_R s^2 + T_c \right) \delta \quad (87)$$

As is evident from Eqs. (21) and (31), the rigid-body pitching motion is also coupled to all the other dynamic modes of the system. Again, if we consider only first-order effects, this may be described with sufficient accuracy by*

$$I_{yy} \ddot{\theta} = T_c \ell_c \delta + L_{\alpha} \ell_{\alpha} \theta + m_R \ell_R \ell_c \ddot{\delta} \quad (88)$$

*We continue to use the approximation, $\alpha \approx \theta$.

The gyro outputs are

$$\theta_{PG} = \theta + \sigma_G^{(i)} q^{(i)} \quad (89)$$

$$\left(s^2 + 2\zeta_R \omega_R s + \omega_R^2\right) \theta_{RG} = K_R \omega_R^2 s \left[\theta + \sigma_G^{(i)} q^{(i)}\right] \quad (90)$$

and the feedback signal is

$$\theta_F = \theta_{RG} + \theta_{PG} \quad (91)$$

Here we have written $\sigma_G^{(i)}$ for $\sigma^{(i)}(l_G)$ where l_G denotes the point on the vehicle where the gyro is located.

We now seek to obtain the open-loop transfer function, θ_F/θ_E . The additional relations pertinent to this objective are

$$\theta_E = \theta_c - \theta_F \quad (92)$$

$$\delta_c = K_A \left(\frac{s + K_I}{s}\right) \theta_E \quad (93)$$

$$\left(s^3 + 2\zeta_c \omega_c s^2 + \omega_c^2 s + K_c \omega_c^2\right) \delta = K_c \omega_c^2 \delta_c \quad (94)$$

For the moment, the effect of load torque feedback to the servoactuator is neglected. A schematic diagram for the system is shown in Fig. 20.

From Eqs. (89) - (91) we obtain

$$\theta_F = \left[\frac{K_R \omega_R^2 s}{\left(s^2 + 2\zeta_R \omega_R s + \omega_R^2\right)} + 1 \right] \left(\theta + \sigma_G^{(i)} q^{(i)}\right) \quad (95)$$

The first factor on the right-hand side of this equation may be expressed as

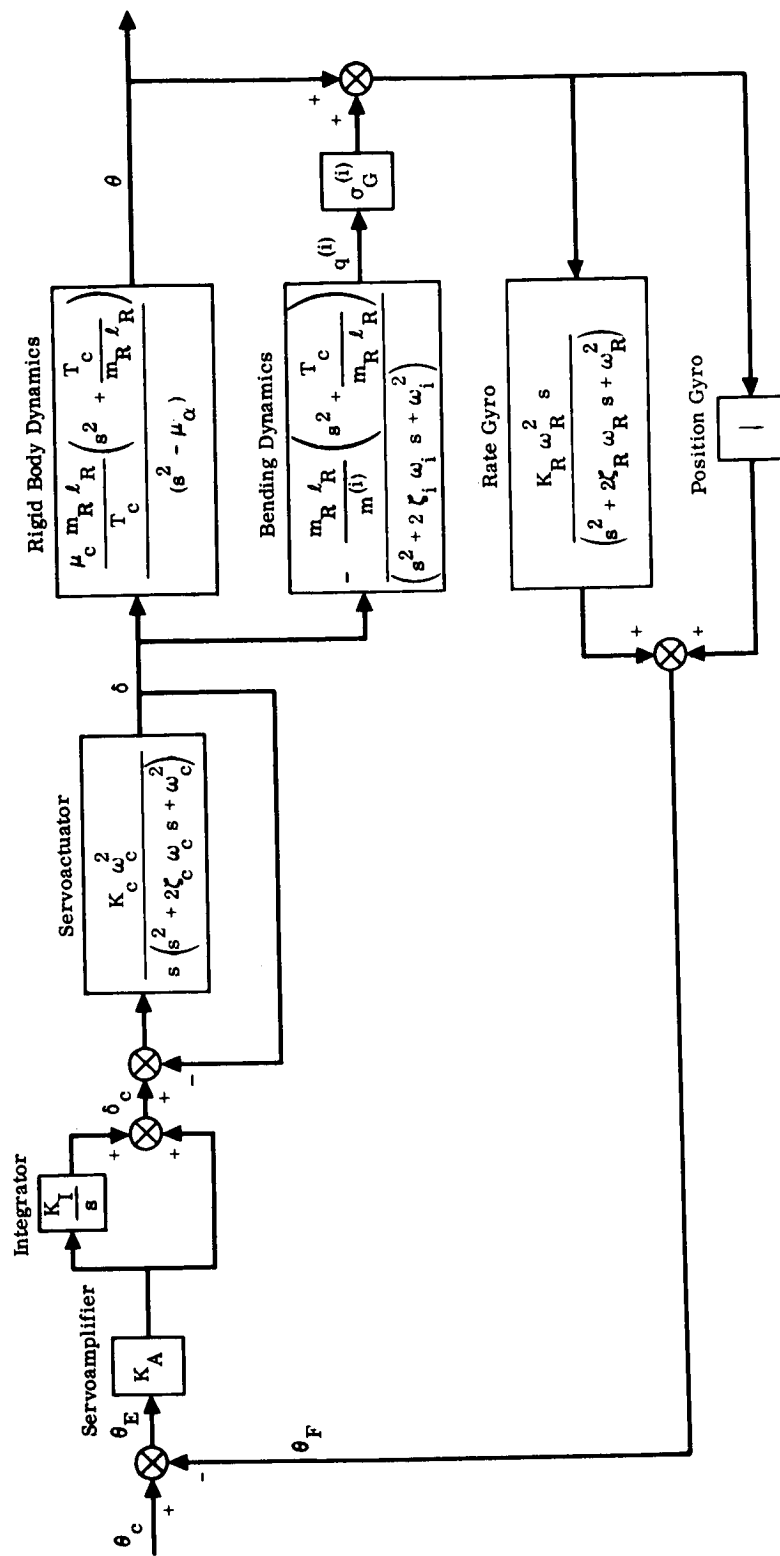


Figure 20. Launch Vehicle Autopilot

$$\frac{K_R \omega_R^2 s}{s^2 + 2 \zeta_R \omega_R s + \omega_R^2} + 1 = \frac{s^2 + 2 \zeta_R' \omega_R s + \omega_R^2}{s^2 + 2 \zeta_R \omega_R s + \omega_R^2}$$

$$= \frac{\omega_R^2 \left[\frac{s}{\omega_R (\zeta_R' - \sqrt{\zeta_R'^2 - 1})} + 1 \right] \left[\frac{s}{\omega_R (\zeta_R' + \sqrt{\zeta_R'^2 - 1})} + 1 \right]}{s^2 + 2 \zeta_R \omega_R s + \omega_R^2}$$

where

$$\zeta_R' = \frac{1}{2} (K_R \omega_R + 2 \zeta_R)$$

Normally, $\zeta_R \ll K_R \omega_R$. We have, therefore,

$$\omega_R (\zeta_R' - \sqrt{\zeta_R'^2 - 1})$$

$$= \omega_R \zeta_R' - \omega_R \zeta_R' \left[1 - \frac{1}{2 \zeta_R'^2} + \dots \right]$$

$$\cong \frac{\omega_R}{2 \zeta_R'} \cong \frac{1}{K_R}$$

Consequently, Eq. (95) may be expressed as

$$\theta_F = \frac{K_R \omega_R^2 \left(s + \frac{1}{K_R} \right)}{\left(s^2 + 2 \zeta_R \omega_R s + \omega_R^2 \right)} \left(\theta + \sigma_G^{(i)} q^{(i)} \right) \quad (96)$$

From Eqs. (87) and (88), we find

$$\theta + \sigma_G^{(i)} q^{(i)} = \left[\frac{\mu_c m_R \ell_R A^{(i)}}{T_c} \right] \frac{\left(s^2 + \frac{T_c}{m_R \ell_R} \right) \left(s^2 + 2 \zeta_k \omega_k s + \omega_k^2 \right)}{\left(s^2 - \mu_\alpha \right) \left(s^2 + 2 \zeta_i \omega_i s + \omega_i^2 \right)} \delta \quad (97)$$

where

$$A^{(i)} = 1 - \frac{T_c \sigma_G^{(i)}}{\mu_c M^{(i)}} \quad (98)$$

$$\omega_k^2 = \frac{\omega_i^2 + \frac{T_c \sigma_G^{(i)}}{\mu_c M^{(i)}} \mu_\alpha}{1 - \frac{T_c \sigma_G^{(i)}}{\mu_c M^{(i)}}} \quad (99)$$

$$\zeta_k \omega_k = \frac{\zeta_i \omega_i}{A^{(i)}} \quad (100)$$

Combining Eqs. (93) and (94),

$$\frac{\delta}{\theta_E} = \frac{K_A K_c \omega_c^2 (s + K_I)}{s (s^3 + 2 \zeta_c \omega_c s^2 + \omega_c^2 s + K_c \omega_c^2)} \quad (101)$$

Making use of Eqs. (96), (97), and (101), we obtain the complete open-loop transfer function as follows.

$$\begin{aligned} \frac{\theta_F}{\theta_E} &= \frac{K_0 (s + K_I) \left(s + \frac{1}{K_R}\right) \left(s^2 + \frac{T_c}{m_R l_R}\right)}{s (s^2 - \mu_\alpha) (s^2 + 2 \zeta_R \omega_R s + \omega_R^2) (s^3 + 2 \zeta_c \omega_c s^2 + \omega_c^2 s + K_c \omega_c^2)} \\ &\quad \times \frac{(s^2 + 2 \zeta_k \omega_k s + \omega_k^2)}{(s^2 + 2 \zeta_i \omega_i s + \omega_i^2)} \end{aligned} \quad (102)$$

$$K_0 = \frac{K_A K_c K_R \mu_c m_R \ell_R \omega_c^2 \omega_R^2 A^{(i)}}{T_c} \quad (103)$$

For studies in the low-frequency range, we may take $\omega_R, \omega_c \rightarrow \infty$ and $m_R \rightarrow 0$. In this case, the transfer function reduces to

$$\frac{\theta_F}{\theta_E} = \frac{K_1 \left(s + K_I\right) \left(s + \frac{1}{K_R}\right) \left(s^2 + 2\zeta_k \omega_k s + \omega_k^2\right)}{s \left(s^2 - \mu_\alpha\right) \left(s + K_c\right) \left(s^2 + 2\zeta_i \omega_i s + \omega_i^2\right)} \quad (104)$$

$$K_1 = K_A K_c K_R \mu_c A^{(i)} \quad (105)$$

We see that by taking account of one bending mode, an additional pole-zero pair has been introduced in the open-loop transfer function. In general, by considering n bending modes, n pole-zero pairs of this type will appear in the open-loop transfer function. However, in this case, the algebra becomes enormously complicated, and the use of a computer is mandatory.

Extensive experience with this problem has shown that the effects of each bending mode can be analyzed separately. Indeed, the rigid-body and slosh modes can also be examined independently of the bending modes. The results of a complete analog or digital computer simulation usually lead to only minor refinements.

The analysis of the bending modes one at a time is permissible since they are orthogonal. Coupling occurs only through the aerodynamic and engine inertia forces. Coupling between slosh and bending forces, for example, is negligible, because these modes are highly tuned (very low relative damping factor).

Therefore the analysis of only one mode at a time not only is instructive in obtaining a basic insight to system dynamics; it also leads to results that are very close to the final values obtained by complete computer simulation.

It is fairly straightforward to determine the stability properties of the system with one bending mode included. Focusing attention on the low-frequency range, we use the open-loop transfer function, Eq. (104), and adopt the approximation* $K_I \approx 0$. Quantity $T_c \sigma_G^{(i)} / \mu_c M^{(i)}$ is of critical importance, and we distinguish three cases:

*This is equivalent to neglecting the pole-zero pair in the vicinity of the origin in the s plane.

$$\text{Case 1} \quad \frac{T_c \sigma_G^{(i)}}{\mu_c M^{(i)}} < 0$$

$$\text{Case 2} \quad 0 < \frac{T_c \sigma_G^{(i)}}{\mu_c M^{(i)}} < 1$$

$$\text{Case 3} \quad 1 < \frac{T_c \sigma_G^{(i)}}{\mu_c M^{(i)}}$$

For Case 1, it is easy to see that $A^{(i)} > 0$ and $\omega_k < \omega_i$. The pole-zero configuration appears as shown in Fig. 21. As long as $\psi_R > \psi_c$, the angle of departure of the root locus from the bending pole is into the left-half plane. In this case, we say that the bending mode is phase-stabilized. As long as the open-loop gain is above some critical value, the system is stable.*

Examining Case 2, we see that $A^{(i)} > 0$ and $\omega_k > \omega_i$ are implied. The pole-zero configuration then appears as shown in Fig. 22. The angle of departure of the root locus from the bending pole is into the right-half plane, and the mode is therefore unstable for all values of open-loop gain. If we consider the effect of bending mode damping, the situation might appear as shown in Fig. 23. Here one chooses an open-loop gain sufficiently low that the closed-loop poles are still in the left-half plane. This is called gain-stabilizing the bending modes. Note that the open-loop gain must still be high enough to yield acceptable rigid-body response. This approach has been found to be most useful for the higher bending modes and when aerodynamic effects are small ($\mu_\alpha \approx 0$).

Turning to Case 3, we see that $A^{(i)} < 0$ and $\omega_k^2 < 0$ are implied. This means that the open-loop gain, K_1 , Eq. (105), is negative and that the bending-mode zeros are on the real axis in the s plane (Fig. 24). Because the open-loop gain is negative, the root locus is now determined by the zero-degree angle criterion (rather than the usual 180 degrees). The angle of departure from the bending pole is still into the right-half plane, as in Case 2, and the root locus has the general form shown. The system is therefore unstable.

*For simplicity, we assume that the mode damping, ζ_1 , is zero.

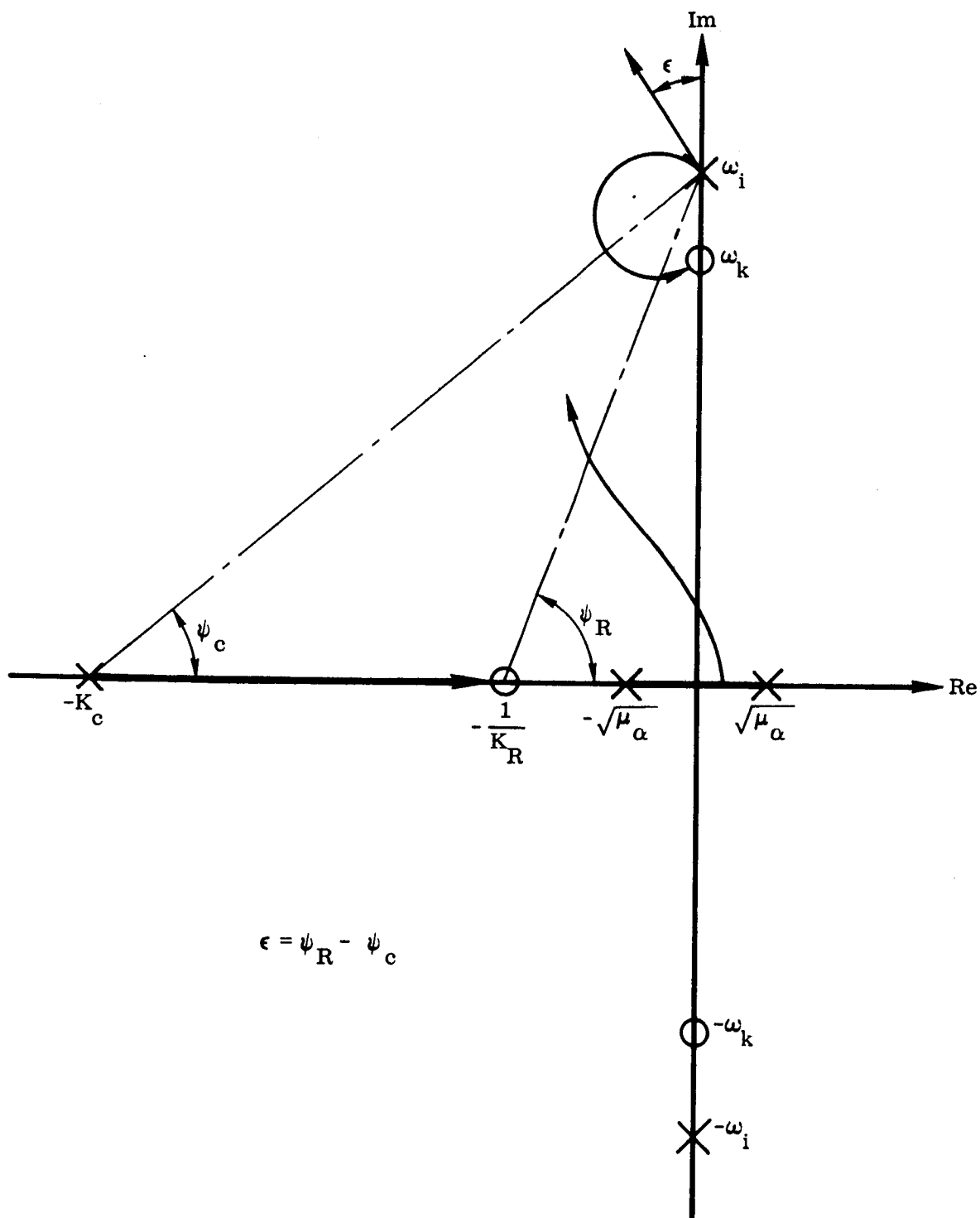


Figure 21. Pole-zero Configuration for Case 1

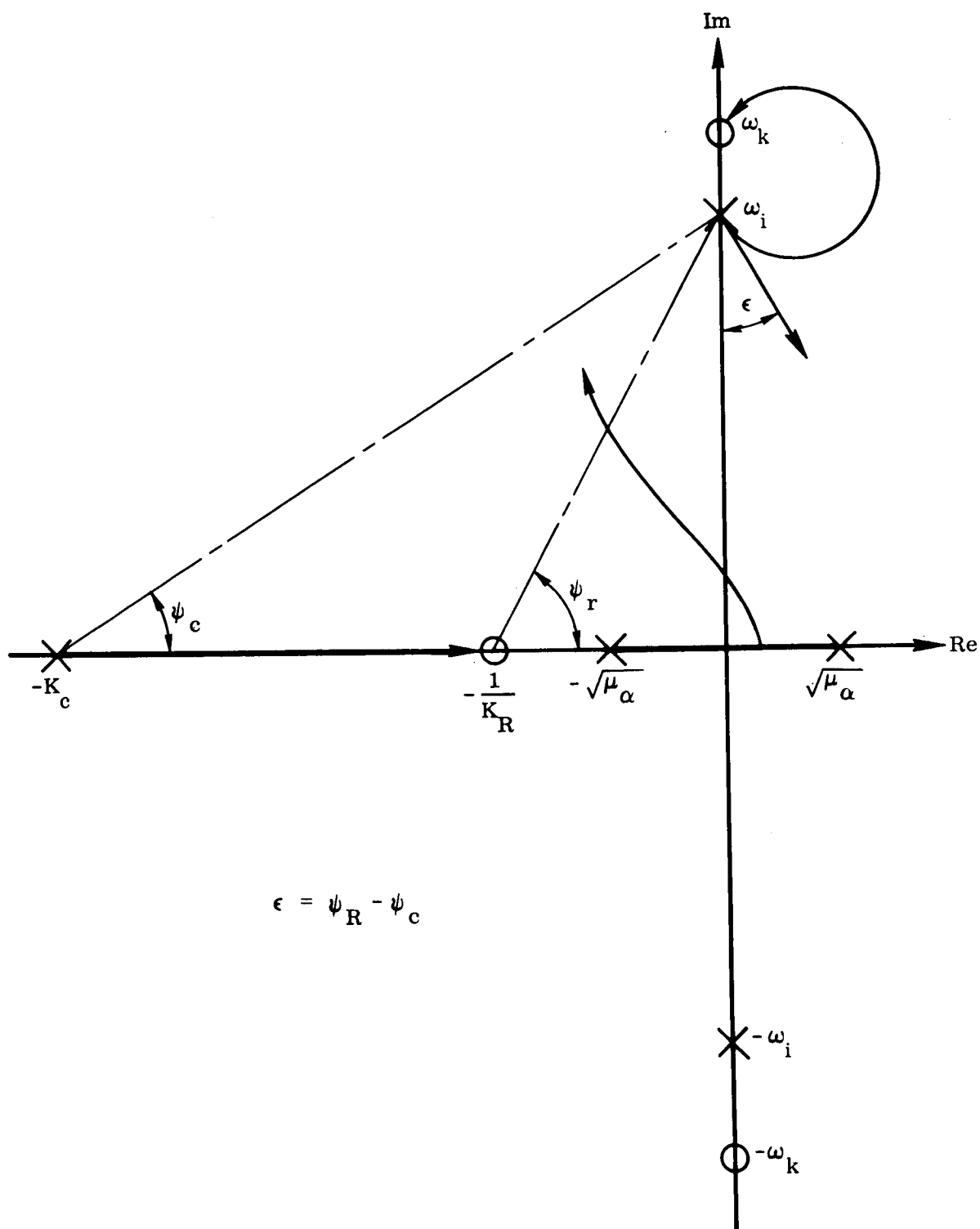


Figure 22. Pole-zero Configuration for Case 2

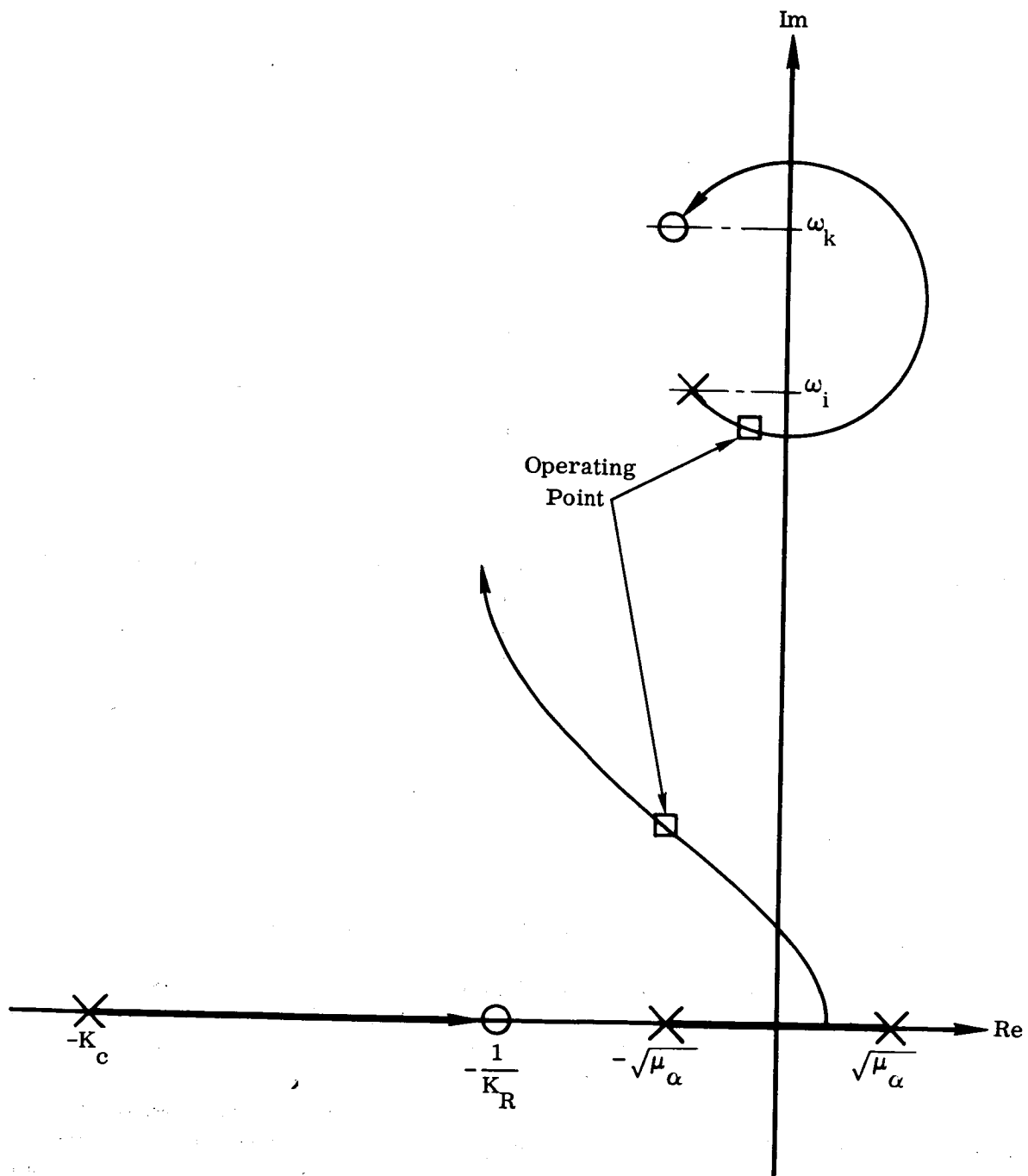


Figure 23. Gain-stabilizing an Unstable Bending Mode

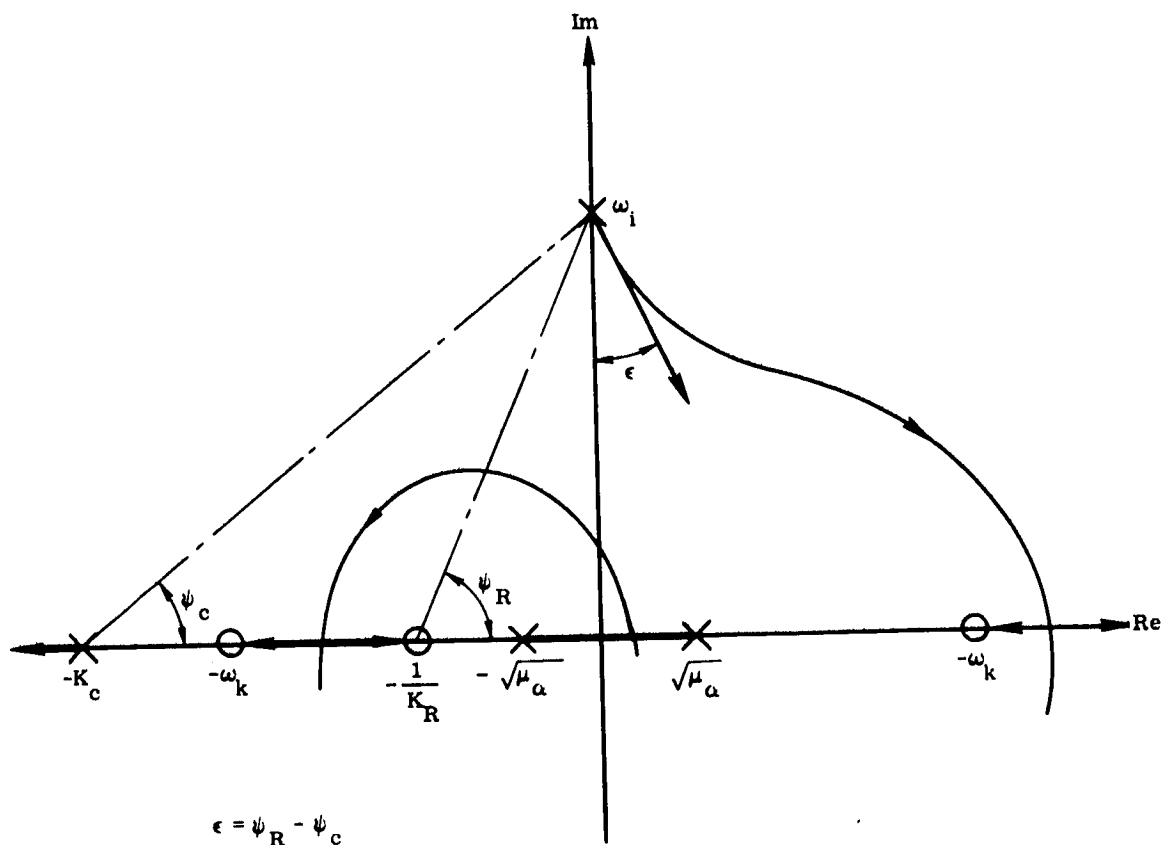


Figure 24. Pole-zero Configuration for Case 3

In the low-frequency range, only the condition represented by Case 1 is stable. This may always be ensured by locating the gyro so that $\sigma_G^{(1)}$ is negative; this generally means an aft location on the vehicle (at least for the lower bending modes).

To analyze the higher bending modes, we must use the more general transfer function represented by Eq. (102).^{*} Assuming that $\sigma_G^{(1)}$ is negative, the pole-zero configuration and departure angles at the bending poles are as shown in Fig. 25. Note that for increasing ω_1 , the departure angle tends to rotate in a clockwise fashion. This

^{*}We still use the approximation $K_I \approx 0$.

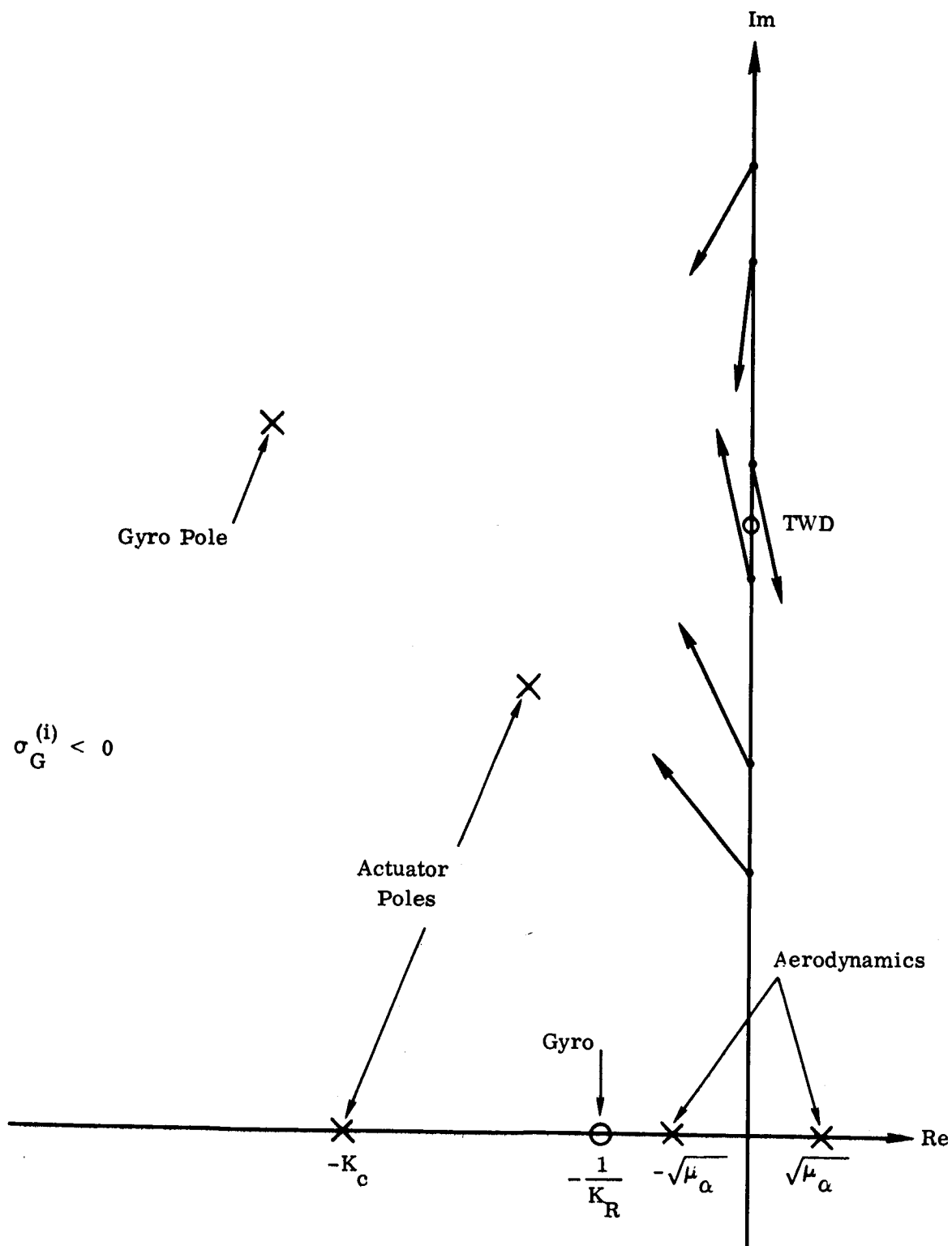


Figure 25. Stability Analysis of Higher Bending Modes, $\sigma_G^{(i)}$ Negative

is because for the higher frequencies, the phase lags due to gyro dynamics and higher-order actuator effects become more significant. Note that when the bending-mode frequency passes the TWD zero, a 180-degree phase reversal is introduced. When $\sigma_G^{(i)}$ is positive, the departure angles at the bending poles are 180 degrees from those shown in Fig. 25. This condition is depicted in Fig. 26. It is apparent that the simple expedient of checking the sign of $\sigma_G^{(i)}$ is no longer sufficient to ensure bending mode stability where the higher bending modes are concerned. In fact, for actual vehicles, some bending modes are always stable while others are unstable. It is therefore not feasible to phase-stabilize all the bending modes, and some combination of proper gyro location, filtering, and gain selection must be used. These factors are taken up in detail in the next section.

3.3.2 Stabilization Techniques

The bending-mode stability problem is the most difficult part of launch vehicle autopilot design, primarily because the bending-mode properties are not known with great precision (especially the higher modes), and they vary with flight time. As long as there is a fair separation in frequency between the bending and rigid-body modes, a proper selection of gain, sensor location, and filtering will yield an acceptable design. In the current generation of launch vehicles, the ratio of fundamental bending to rigid-body mode frequency is on the order of 2.5 to 3. When this figure becomes lower, it is increasingly more difficult to ensure adequate rigid-body response and at the same time stabilize the bending modes. In this case, gain-stabilizing the (relatively) higher bending modes is not effective, because there is little latitude in utilizing the structural damping, ζ_i , when the frequencies are fairly low. It is therefore necessary to use more sophisticated techniques. These are discussed in another monograph in this series.* The more conventional approaches are considered next.

3.3.2.1 Filters

Sec. 3.3.1.4 showed that the lower bending modes can always be phase-stabilized if the gyros are located at the aft end of the vehicle ($\sigma_G^{(i)}$ negative). However, it is often necessary to locate the instrumentation package near the nose of the vehicle, in which case (at least for the lowest bending mode), $\sigma_G^{(i)}$ is positive, and the mode is unstable. This corresponds to Cases 2 and 3, illustrated in Figs. 22 and 24 respectively. It is possible, however, to stabilize these modes by appropriate passive filtering. The main requirement is to rotate the departure angle from the bending pole into the left-half plane. Referring to Fig. 22, if a simple lag filter is added to the open-loop transfer function, the situation depicted in Fig. 27 is obtained. The original departure angle from the bending pole is shown by the dotted line. Introducing the simple lag filter (i.e., the pole at $-\frac{1}{\tau_F}$) adds ψ_F degrees of phase lag to the bending pole departure angle, with the result that it is now directed into the left-half plane. Thus the bending mode has been phase-stabilized. There is a penalty

*Vol. III, part 8, "Adaptive Control."

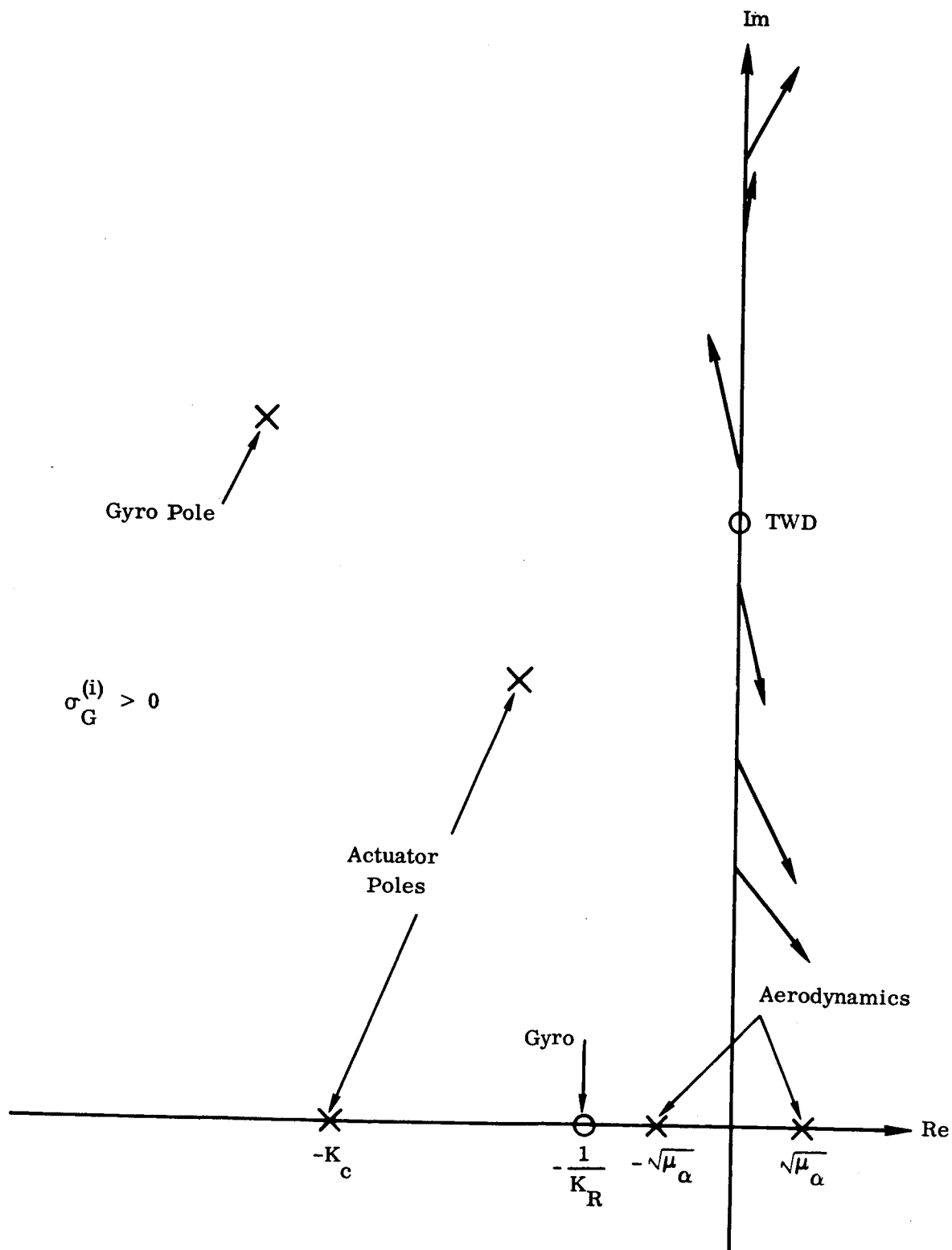


Figure 26. Stability Analysis of Higher Bending Modes, $\sigma_G^{(i)}$ Positive

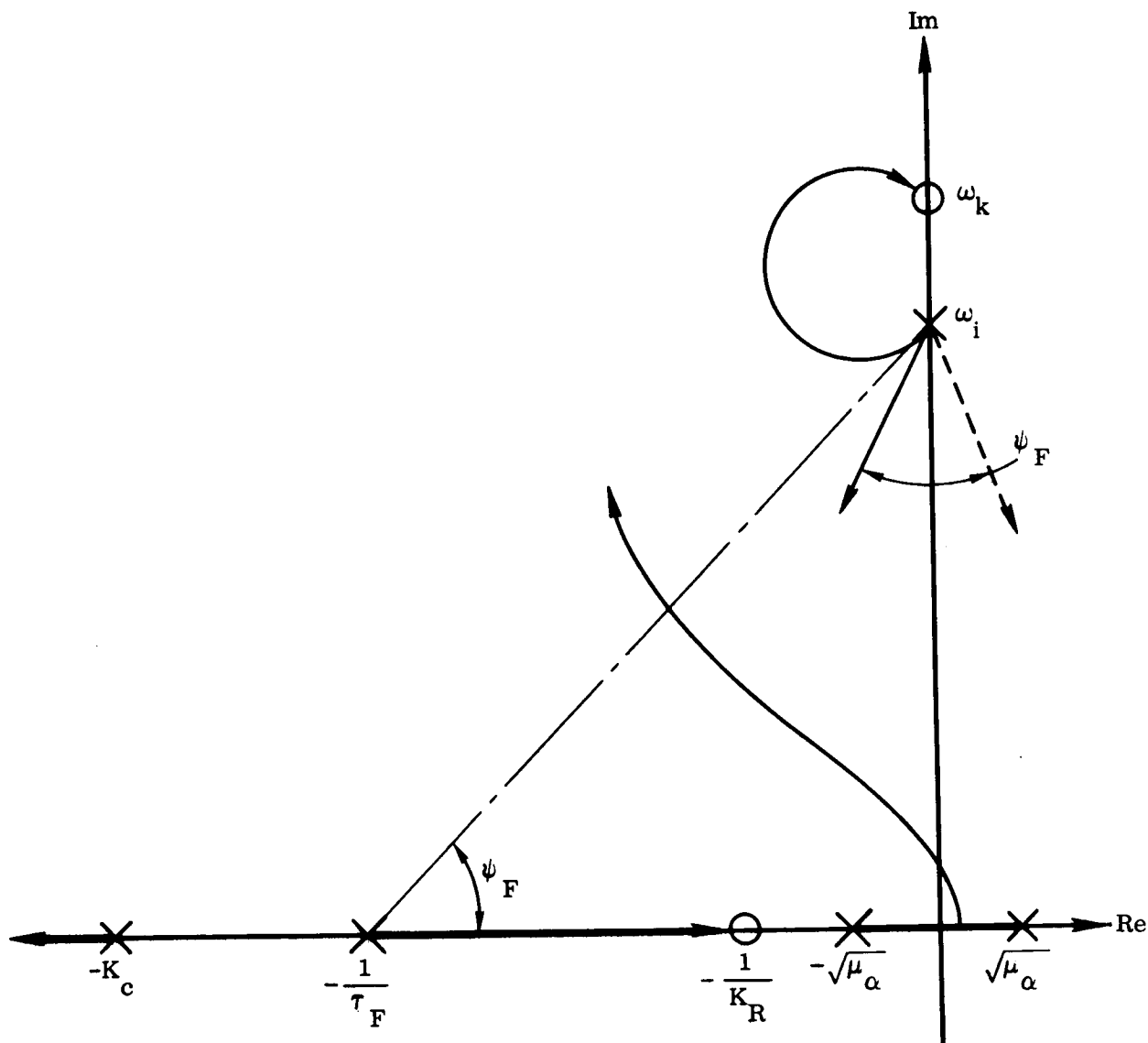


Figure 27. Stabilizing an Unstable Bending Mode by Passive Filters (Case 2)

incurred here, in that the use of a passive filter decreases the gain and phase margins for the rigid-body mode. In short, too large a value for the time constant, τ_F , will seriously deteriorate rigid-body performance. A successful use of this approach, therefore, requires a fair separation (about 3 or 4 to 1) between bending and rigid-body frequencies. For

$$\frac{T_c \sigma_G^{(i)}}{\mu_c M^{(i)}} > 1$$

which corresponds to Case 3 of Sec. 3.3.1.4, the bending zeros are on the real axis. This configuration is shown in Fig. 24. By adding a simple lag filter as before, we obtain the condition shown in Fig. 28. The passive filter again adds ψ_F degrees of phase lag, which rotates the bending mode departure angle into the left-half plane. The bending mode is now only gain-stabilized, since, for sufficiently high open-loop gain, the bending mode becomes unstable.

It is helpful to examine some of these situations quantitatively. For this purpose we will use the basic data for a typical launch vehicle, as given in Appendix A. In all cases, the open-loop transfer function is

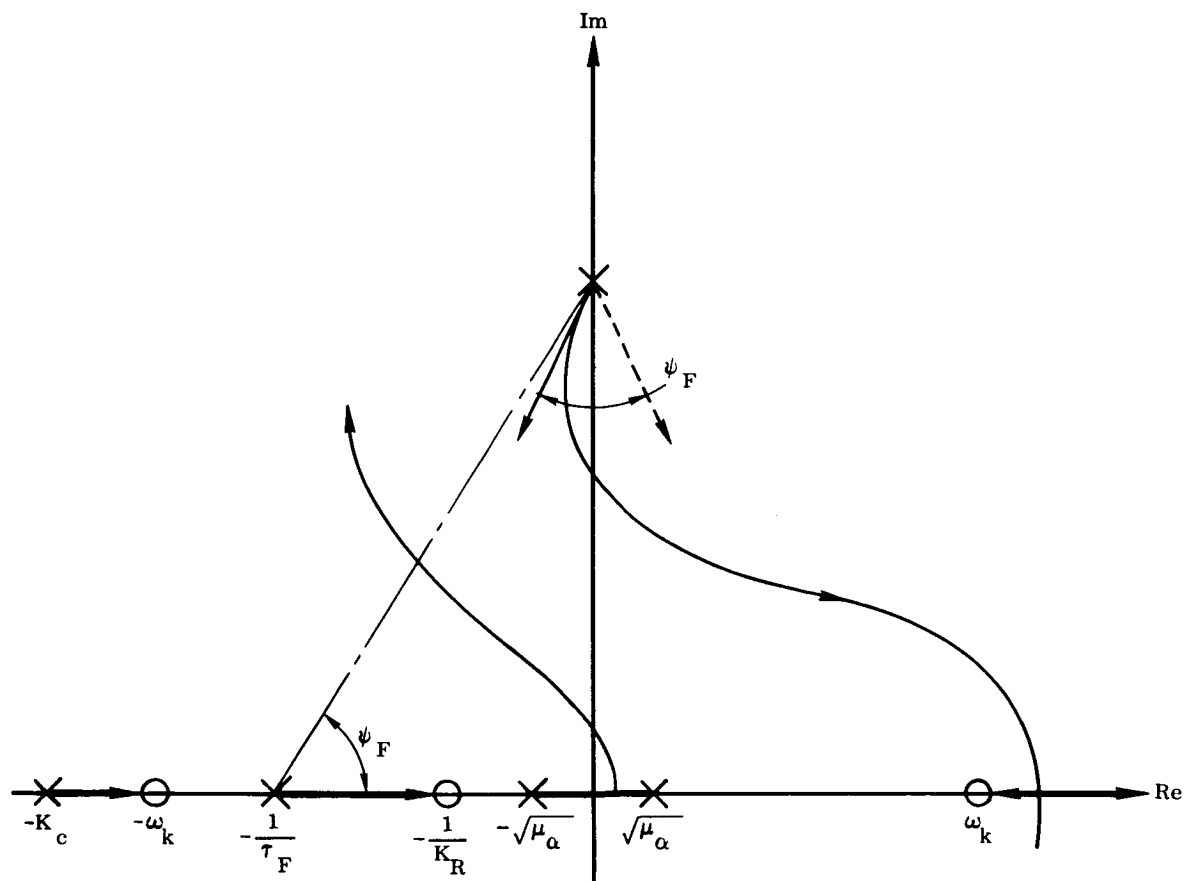


Figure 28. Stabilizing an Unstable Bending Mode by Passive Filters (Case 3)

$$\frac{\theta_F}{\theta_E} = \frac{K_1 (s + K_I) \left(s + \frac{1}{K_R}\right) (s^2 + 2 \zeta_k \omega_k s + \omega_k^2)}{s (s^2 - \mu_\alpha) (s + K_c) \left(s + \frac{1}{\tau_1}\right) \left(s + \frac{1}{\tau_2}\right) (s^2 + 2 \zeta_1 \omega_1 s + \omega_1^2)} \quad (106)$$

$$K_1 = \frac{K_A K_c K_R \mu_c A^{(1)}}{\tau_1 \tau_2}$$

with

$$K_c = 30$$

$$K_R = 0.333$$

$$K_I = 0.40$$

We will examine four cases:

A. $t = 72 \text{ sec}$ Rate Gyro @ SN966

$$\tau_1 = 0.0265 \text{ sec}$$

$$\tau_2 = 0$$

B. $t = 152 \text{ sec}$ Rate Gyro @ SN966

$$\tau_1 = 0.0265 \text{ sec}$$

$$\tau_2 = 0$$

C. $t = 72 \text{ sec}$ Rate Gyro @ SN400

$$\tau_1 = 0.04 \text{ sec}$$

$$\tau_2 = 0.04 \text{ sec}$$

D. $t = 152 \text{ sec}$ Rate Gyro @ SN400

$$\tau_1 = 0.04 \text{ sec}$$

$$\tau_2 = 0.04 \text{ sec}$$

The respective root loci are shown in Figs. 29-32. With the rate gyro located near the aft end of the vehicle, the mode slope at the gyro location is negative. This implies a stable condition. Thus Fig. 29 corresponds in form to Case 1 of Fig. 21. At a later time of flight, $t = 152$ sec, the fundamental bending-mode frequency has increased to 41.1 rad/sec, with the result that the departure angle of the bending pole is into the right-half plane (Fig. 30). This illustrates the basic limitation of the simple stability criterion stated in Sec. 3.3.1.4; namely, the bending mode is stable if $\sigma_G^{(i)}$ is negative. The frequency range in which this criterion is applicable must be determined beforehand. This can always be done once the open-loop poles and zeros are specified, using a diagram of the form of Fig. 25.

It will be noted that Cases A and B employ a simple lag filter whose effect is to deteriorate both the rigid-body and the bending-mode responses. This has been included because many autopilots will have some lag introduced into the lower-frequency modes from filters intended to shape the intermediate or higher bending-mode loci. Obviously, Case B is unsatisfactory, and some remedy must be employed. The simplest solution is to introduce some phase lead in the vicinity of 30-50 rad/sec. This is sometimes done by switching in a filter that is active only in a prescribed flight interval.

Cases C and D illustrate the condition of a gyro location near the nose of the vehicle ($\sigma_G^{(i)}$ positive). Stability considerations require that a double lag filter be used in order to stabilize the bending mode. The gain margin in the system is severely compromised but may be assumed adequate.* The phase margin in Fig. 31 is about 37 degrees; in Fig. 32, it is about 85 degrees.

In all the above cases, only one bending mode at a time was considered. Usually, a gyro location that is favorable for one mode is unfavorable for others. Preliminary selection of filters of and sensor location must therefore be validated by a complete computer simulation that includes all significant coupling and nonlinear effects. The factors that influence these final design values are discussed next.

3.3.2.2 Sensor Location

When establishing preliminary shaping-filter values and sensor location, one focuses primary attention on the fundamental bending mode. To assure that the influence of nonlinearities and coupling with other modes does not vitiate the selected gains, locations, etc., the complete system dynamics must be studied via computer. Such a simulation must include all significant bending modes (generally a maximum of five), higher-order engine inertia effects as well as oil and mount compliances, flow nonlinearities, etc. Aerodynamics, sloshing, and instrumentation dynamics must also be included.

*With $K_A = 1.8$, the gain margin is on the order of 6 db.

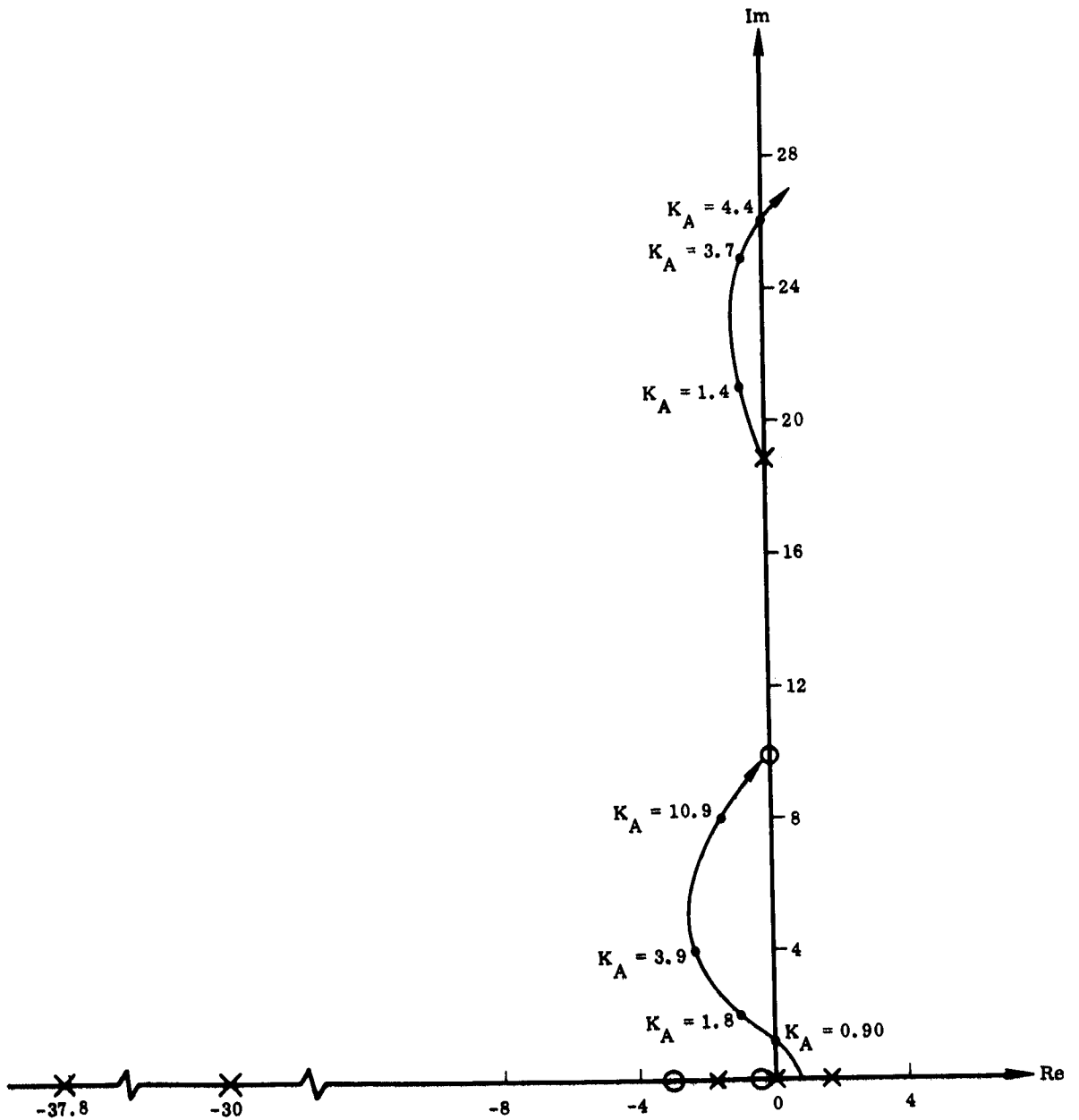


Figure 29. Root Locus for Case A

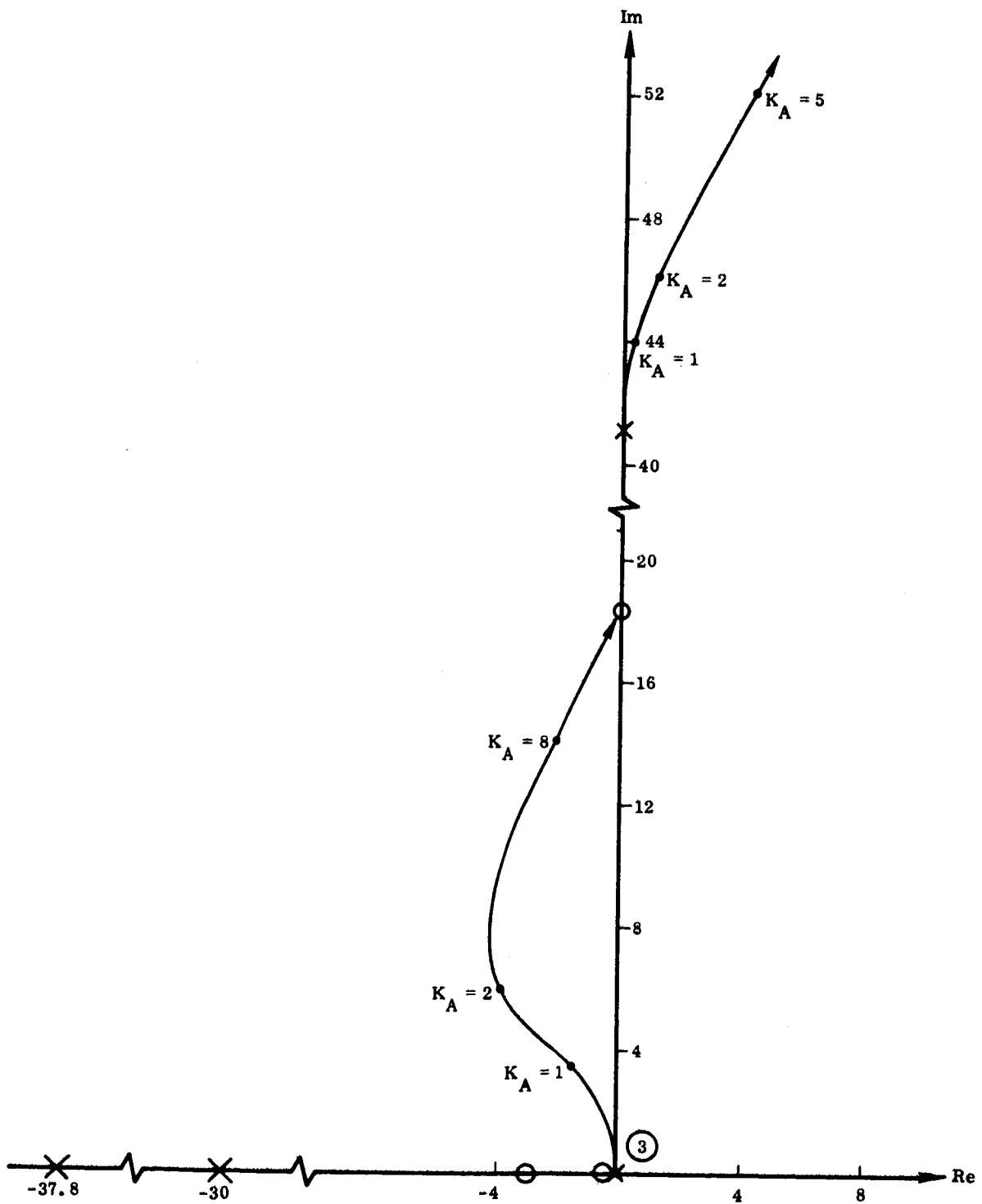


Figure 30. Root Locus for Case B

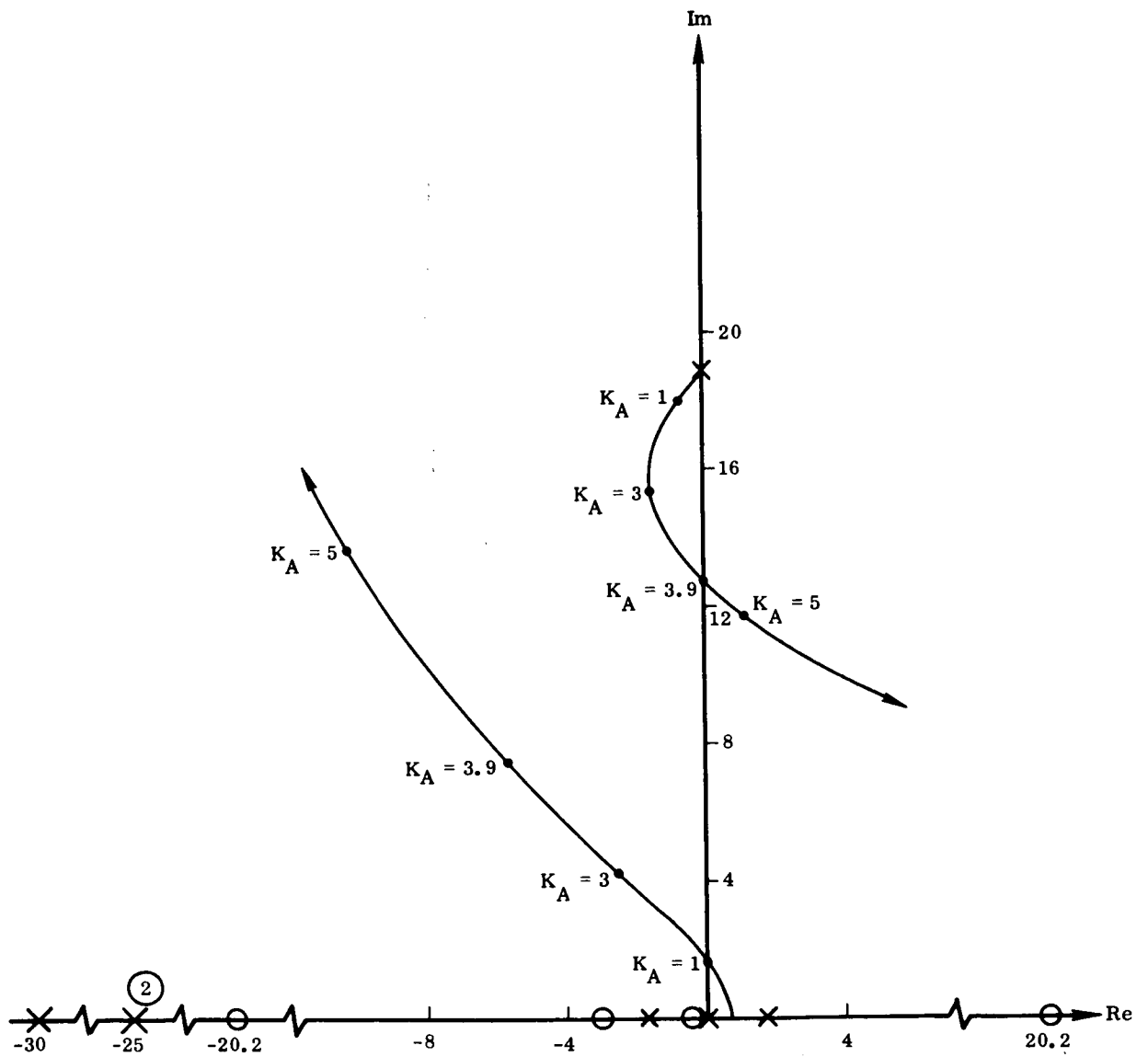


Figure 31. Root Locus for Case C

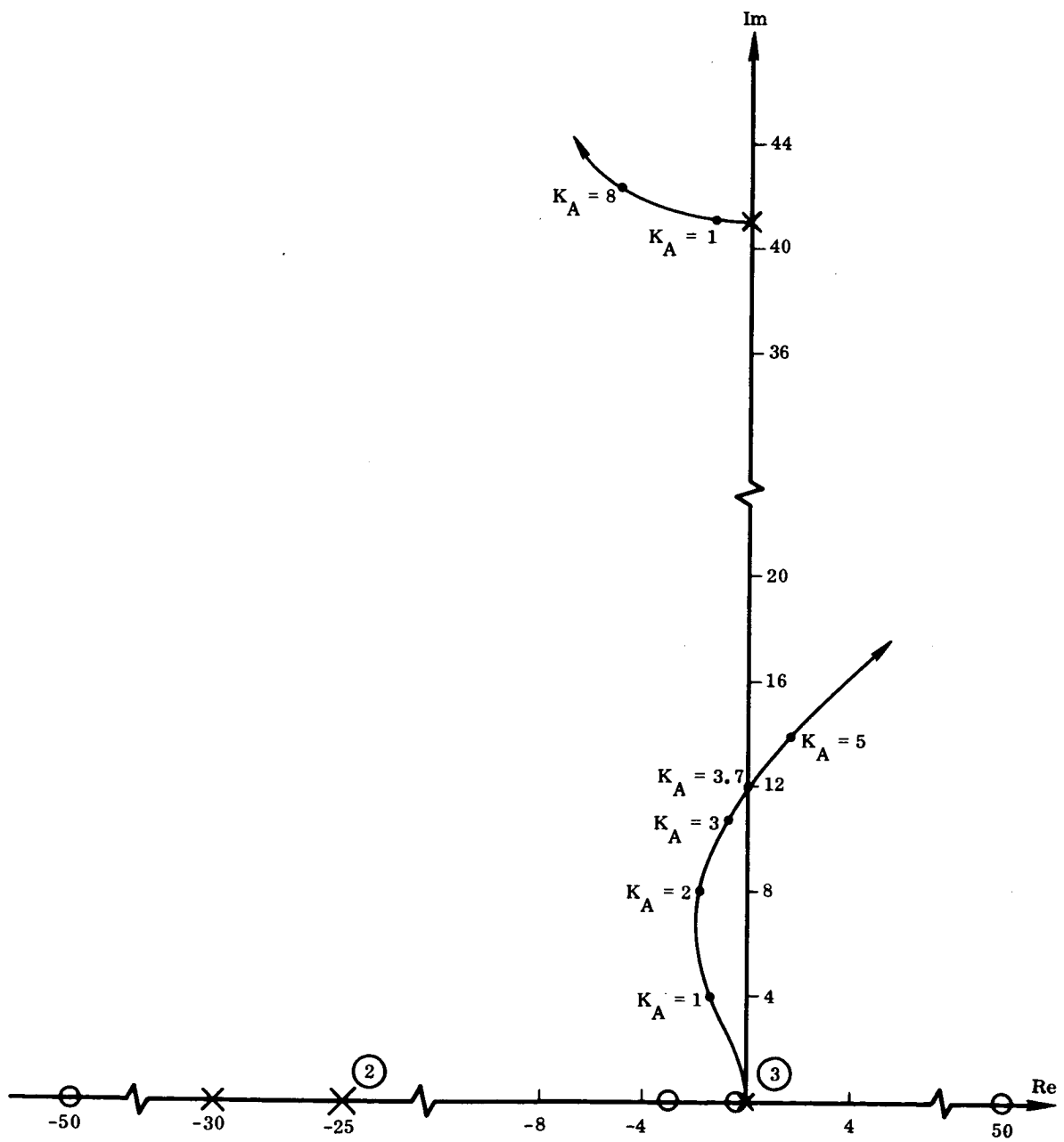


Figure 32. Root Locus for Case D

The inclusion of aerodynamics usually leads to an effective reduction of the bending-mode frequencies and some damping. Instrumentation and actuator dynamics are often in the bandpass of the intermediate and higher bending modes and therefore have a significant effect on their stability properties. Coupling of the slosh modes with the fundamental bending mode is often severe at certain times of flight.

Experience has shown that the most important nonlinearities in the system are:

- a. The hydraulic pressure-flow relationship in the servo valve.
- b. Engine gimbal bearing coulomb friction.
- c. Valve dead zone.

Saturation effects in engine deflection and instrumentation are important to a lesser degree.

An unstable condition manifests itself in the form of a limit cycle rather than a divergent oscillation. Stability may therefore be viewed as a condition whereby the system either returns to a quiescent state or exhibits a limit cycle whose amplitude and frequency are not objectionable.

One valid criterion for judging the merit of a particular sensor location is the gain margin obtained. As used here, "gain margin" is not a precise term, since we are dealing with a nonlinear system. Instead, it is taken to mean the ratio of open-loop gain that produces an unacceptable limit cycle to the nominal value of this gain.

Values of open loop-gain and sensor location are determined as follows. For any given sensor location, determine the loop gain, $K_A K_R$, that results in an unacceptable limit cycle. Do this for a series of locations along the vehicle. The results may be plotted in the manner shown in Fig. 33. This figure shows the stability boundaries for three times of flight, superimposed on one plot. It is now possible to select a location and an open-loop gain that is satisfactory throughout flight. As a rule, the preliminary choices will be modified only slightly, since the broad features of the system derived by simplified analyses do not alter radically when higher-order dynamic effects are included.

Neither the simplified analytical or empirical approach is valid by itself for a complex system typified by the launch vehicle autopilot. However, a judicious blend of both in the manner noted above represents an efficient design procedure.

3.3.3 Influence of Nonlinearities

In the discussions thus far, it has been assumed that the vehicle autopilot dynamics could be represented by a linear, constant-coefficient system at any given

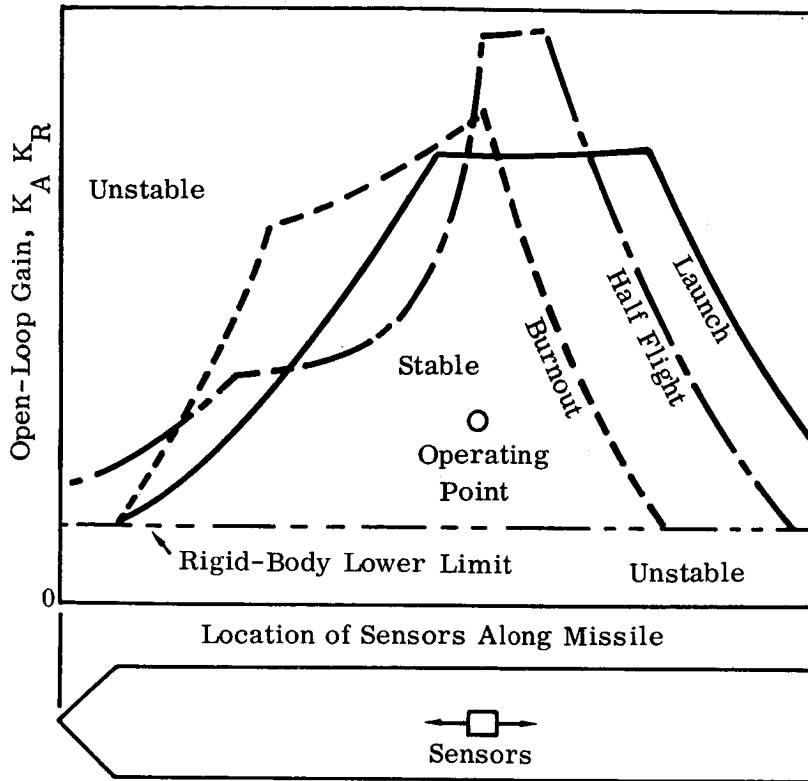


Figure 33. Typical Stability Boundary Plot for Several Flight Times

instant of flight time. The state variables, in this context, represent small deviations from some prescribed reference condition. Two questions arise. Is this so-called "time-slice" approximation valid; and how serious is the neglect of various nonlinearities in the system?

In the first place, the implicit assumption in the "time-slice" approximation is that the vehicle mass and inertial properties vary "slowly" over a small time interval and therefore may be represented by average (constant) values in this interval. If the resulting linear stationary system is found to be stable, then it is presumed that the nonstationary (time-varying) system is stable. However, counter examples show that this presumption is not always true. For a launch vehicle autopilot of the type shown in Fig. 10 and having negligible actuator phase lag, sufficient conditions for stability of the nonstationary system are given by⁽¹⁸⁾

$$2 K_A K_R \mu_c > \frac{\dot{\mu}_\alpha - K_A \dot{\mu}_c}{(K_A \mu_c - \mu_\alpha)} \quad (107)$$

$$K_A \mu_c - \mu_\alpha > 0 \quad (108)$$

Eq. (108) is the condition derived in the usual time-slice case. Inequality (107) displays the destabilizing influence of a rapidly increasing μ_α in quantitative form. Time histories of μ_c and μ_α for a typical Atlas vehicle are shown in Figs. 34 and 35. Positive values of $\dot{\mu}_\alpha$ vary from about 0.007 sec^{-3} to 0.078 sec^{-3} near $\max q$. It is readily found that in this case, inequality (107) is satisfied with ample margin. Thus, at least in the case of large booster vehicles, the stability of the nonstationary system is not a major concern (as has been verified by extensive flight tests).

Nonlinearities in the system are derived from various sources:

- a. Flow nonlinearities of the servovalve.
- b. Engine gimbal coulomb friction.
- c. Saturation and dead-zone effect in sensors.
- d. Displacement and rate limits for engine deflection angles.

Sources c and d are not usually significant in launch vehicle autopilots because high-quality gyro instrumentation is employed and sufficient control capability must be provided in the rocket engines to prevent prescribed limits from being exceeded. However, nonlinearities a and b do have a significant influence on the control system response, especially insofar as bending-mode limit cycles are concerned.

Taking account of these nonlinear effects means that the engine dynamics described by Eq. (33) are no longer valid, since this system is not linear. By taking a describing function point of view, we may still represent the actuator by a transfer function identical in form to Eq. (33). However, K_c , ω_c , and ζ_c are no longer constant but are actually functions of the amplitude and frequency of the applied signal (assumed sinusoidal).

The method of analysis is due to Backus⁽¹⁰⁾ and is described in detail in another monograph in this series.* The transfer function for the "equivalent linear" system (describing function) is given by

$$\begin{aligned} & \left(s^3 + 2 \zeta_{cn} \omega_{cn} s^2 + \omega_{cn}^2 s + K_c \omega_c^2 \right) \delta \\ & = K_c \omega_c^2 \delta_c - \frac{1}{I_R} (s + K_0) T_L \end{aligned} \quad (109)$$

*Vol. III, part 11, "Component Dynamics."

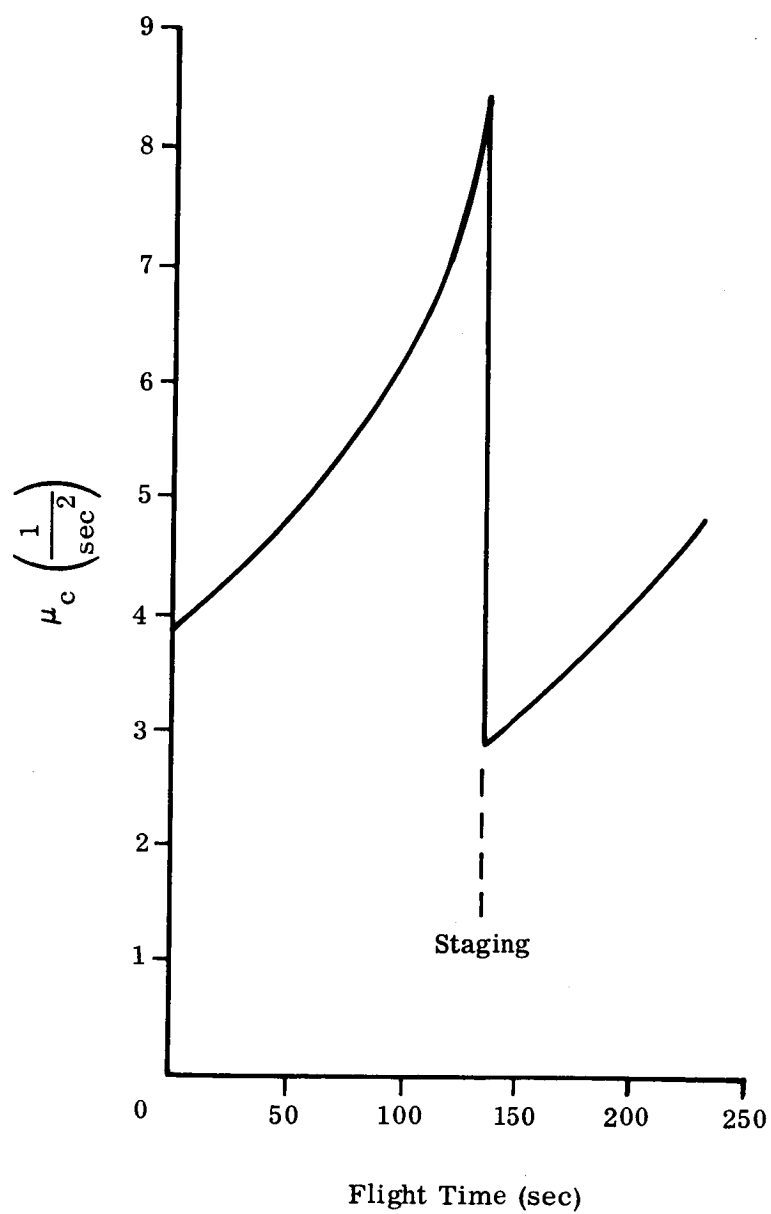


Figure 34. Flight History for μ_c

where

$$K_c = \frac{K_a K_v}{AR} \sqrt{P_s - P_R}$$

$$\omega_c^2 = \frac{(AR)^2}{I_R} \left(\frac{V_T}{4B} + \frac{A^2}{K_m} \right)^{-1}$$

$$\omega_{cn}^2 = \omega_c^2 + \frac{\bar{C}_f K_0}{I_R}$$

$$2 \zeta_{cn} \omega_{cn} = K_0 + \frac{\bar{C}_f}{I_R}$$

$$K_0 = \left(\frac{V_T}{4B} + \frac{A^2}{K_m} \right)^{-1} \left(\bar{C}_L + \frac{A^2}{K_m} K_c \right)$$

$$\bar{C}_f = C_v + \frac{4 C_B}{\pi \omega \bar{\delta}}$$

$$\bar{C}_L = 1.11 C_L \left[\frac{\bar{\delta}}{AR} \sqrt{(I_R \omega^2)^2 + (\bar{C}_f \omega)^2} \right]^{-\frac{1}{2}}$$

Definitions and typical values for the servo system parameters may be found in Appendix A. Having the system parameters, the quantities ω_{cn} , ζ_{cn} , and K_0 are then functions of $\bar{\delta}$, the output amplitude, and the frequency, ω .

In the low-frequency range, Eq. (109) may be simplified by letting $\omega_c \rightarrow \infty$. The result is

$$\frac{\delta}{\delta_c} = \frac{K'_c}{s + K'_c} \quad (110)$$

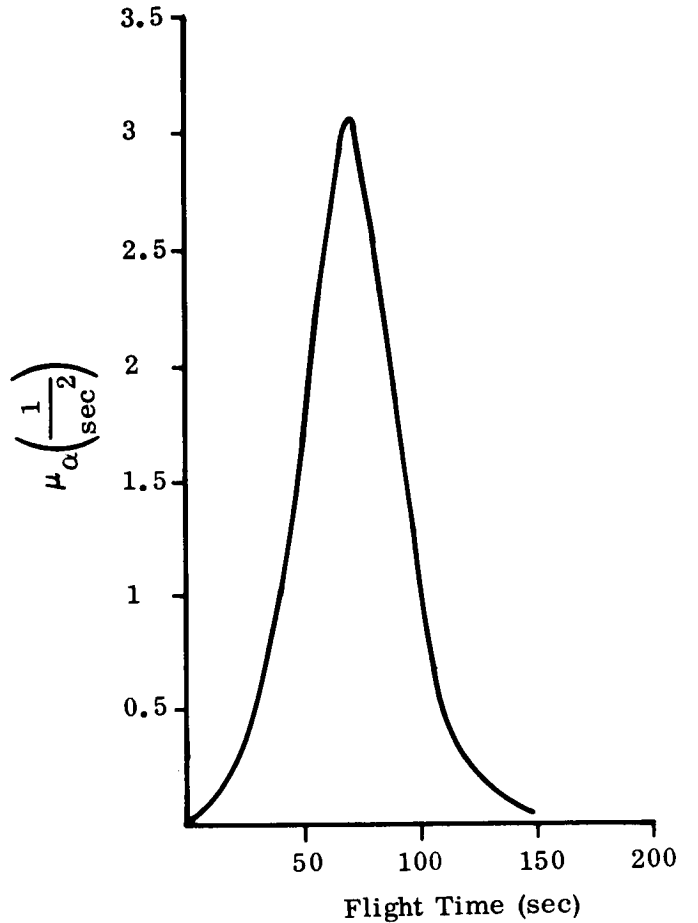


Figure 35. Flight History for μ_α

where

$$K'_c = K_c \left[1 + \frac{\bar{C}_f \left(\bar{C}_L + \frac{A^2}{K_m} K_c \right)}{A^2 R^2} \right]^{-1}$$

A typical plot of K'_c vs. $\bar{\delta}$ is shown in Fig. 36 for several values of ω .

The use of the "equivalent linear" transfer functions, (109) or (110), in determining the (possible) existence of stable or unstable limit cycles will now be described. It should be pointed out, first of all, that the usual describing function is expressed by $j\omega$ rather than s . Thus Eq. (109) or (110) is, strictly speaking, true only for $s = j\omega$. However, if we use $s = \sigma + j\omega$ whenever σ is sufficiently small,* the results obtained will be reasonably accurate.

Assume now that a linear analysis of the autopilot shown in Fig. 20 indicates a potentially unstable bending mode, the root locus of which has the form shown in Fig. 23. Obviously, for sufficiently high open-loop gain, K_A , there will exist a divergent

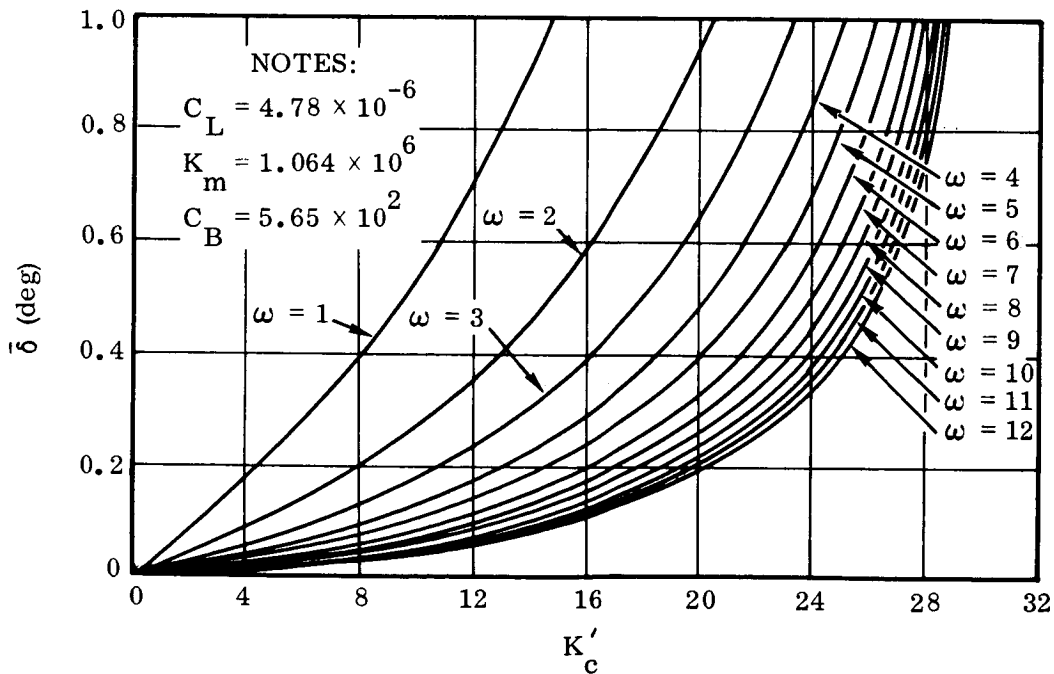


Figure 36. Low-frequency Approximation $K'_c/(s + K'_c)$

* $\sigma \approx 0.05 \omega$.

oscillation at the bending mode frequency. It will be shown that by taking account of the actuator nonlinearities, one can predict the amplitude and frequency of a limit cycle rather than a divergent oscillation (a condition verified by computer simulation).

To do this we assume a value for the steady-state engine angle, $\bar{\delta}$, and a frequency $\omega = \omega_1$ (i.e., the bending-mode frequency). This then yields values for the parameters of the equivalent linear transfer function, Eq. (110).^{*} One obtains these either by direct calculation or from a curve of the type shown in Fig. 36. Having this, we may then calculate the closed-loop poles for the system. This is done for a range of values of $\bar{\delta}$. Fig. 37 shows the closed-loop bending poles obtained in this fashion. Here the bending mode frequency $\omega_1 \approx 28$ rad/sec; a constant value of $K_A = 1.5$ was used throughout. Fig. 37 contains all the necessary information relative to the existence of stable or unstable limit cycles and their respective amplitudes and frequency. To show this, we proceed as follows. Suppose that some disturbance produces an engine oscillation of amplitude $\bar{\delta} = 0.05$ deg. This results in a closed-loop pole labeled $\bar{\delta} = 0.05$ in Fig. 37. Since this pole is in the left-half plane, the engine amplitudes will damp out, such that successively smaller values of $\bar{\delta}$ are produced, eventually leading to a quiescent state, $\bar{\delta} = 0$. However, if some disturbance causes an engine oscillation of amplitude $\bar{\delta} = 0.10$ deg, it yields a closed-loop pole in the right-half plane, with the result that the engine amplitudes increase and the closed-loop poles approach point B. If $\bar{\delta}$ increases still further, the closed-loop poles enter the left-half plane, meaning that the oscillation amplitudes tend to damp out. Thus it is apparent that point B is a point of stable equilibrium and corresponds, in fact, to the amplitude and frequency of a stable limit cycle; in the present case, these have the values $\bar{\delta} = 0.37$ deg and $\omega = 28.15$ rad/sec. Similarly, we find that point A corresponds to an unstable limit cycle. It may be concluded, therefore, that any disturbance that produces an engine amplitude $\bar{\delta} < 0.075$ deg will ultimately return to a quiescent state $\bar{\delta} = 0$, while any disturbance that causes a larger engine amplitude will lead to a stable limit cycle with amplitude and frequency as noted above.

Instead of the one locus shown in Fig. 37 for one value of open-loop gain, one may form a series of loci for different values of open-loop gain as shown in Fig. 38. An examination of these loci shows that when $K_A < 1.30$, the system returns to the quiescent state, whatever the magnitude of the engine amplitude caused by a disturbance. It is apparent that an identical approach may be used to determine slosh limit cycles.

In applying the technique herein described, the use of a digital computer is virtually mandatory. However in certain simplified situations, it is possible to modify the above approach such that conventional root-locus techniques may be used.⁽¹⁹⁾ Consider, for example, the autopilot shown in Fig. 39, in which the equivalent linear transfer function of Eq. (110) is used. Via some elementary operations, this may be transformed to the form shown in Fig. 40, in which parameter K'_C appears as an "open-loop gain" in the transfer function.

^{*}Or, equivalently, Eq. (109), whichever is used.

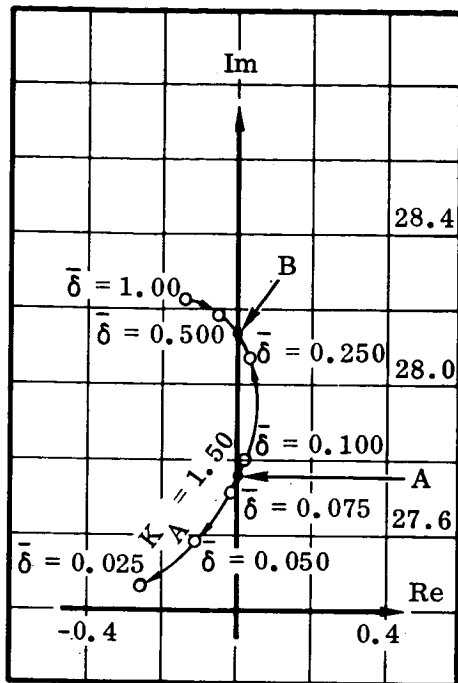


Figure 37. Constant-amplitude and Constant-gain Loci

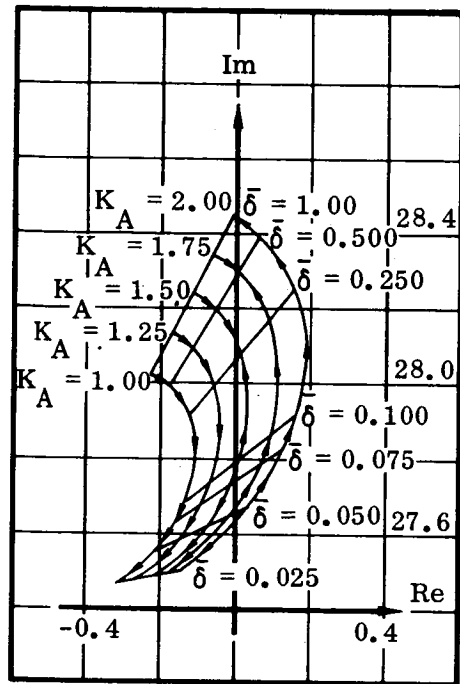


Figure 38. Family of Constant-gain vs. Constant-amplitude Loci

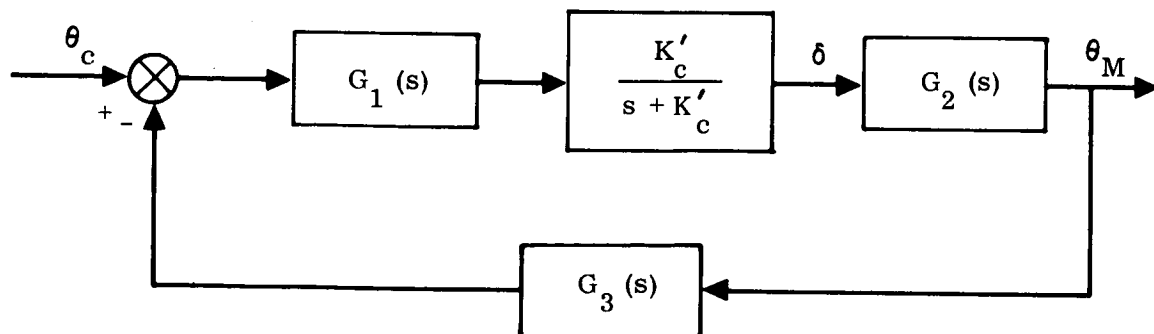


Figure 39. Simplified Autopilot with Equivalent Linear Transfer Function for Actuator

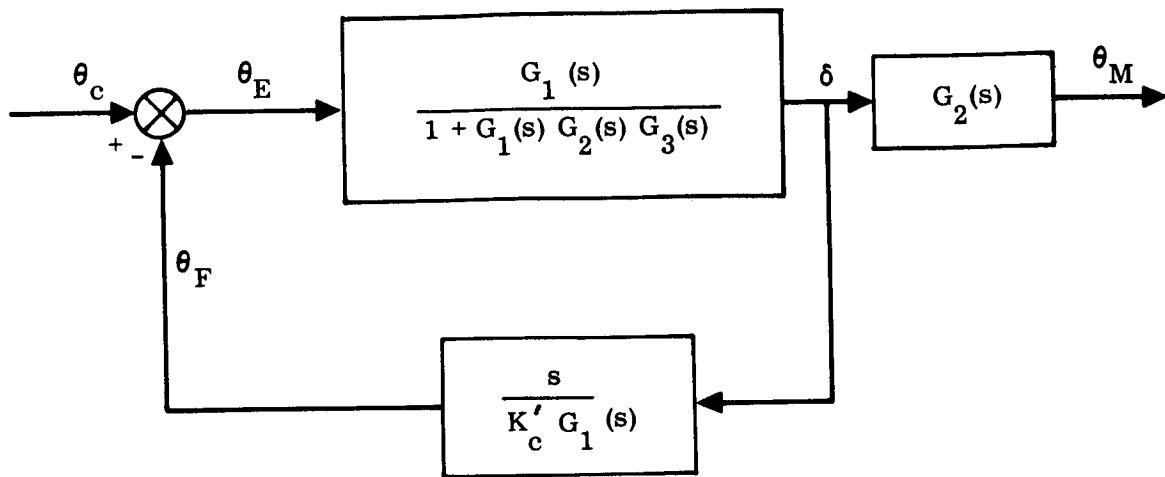


Figure 40. Equivalent Form of Autopilot of Figure 38

$$\frac{\theta_F}{\theta_E} = \left(\frac{1}{K'_c} \right) \frac{s}{1 + G_1(s) G_2(s) G_3(s)} \quad (111)$$

For convenience, we have defined

$$\theta_M = \theta + \sigma_G^{(i)} q^{(i)} \quad (112)$$

in Figs. 39 and 40, which is useful when only one bending mode is considered.

We then take

$$G_1(s) = K_A$$

$$G_2(s) = \frac{\mu_c A^{(i)}}{(s^2 - \mu_\alpha)} \frac{(s^2 + 2\zeta_k \omega_k s + \omega_k^2)}{(s^2 + 2\zeta_i \omega_i s + \omega_i^2)}$$

$$G_3(s) = K_R s + 1$$

The expression for $G_2(s)$ is obtained from Eq. (97) after neglecting engine inertia effects. Substituting these relations in Eq. (111), we find

$$\frac{\theta_F}{\theta_E} = \left(\frac{1}{K'_c} \right) \frac{s(s^2 - \mu_\alpha)(s^2 + 2\zeta_i \omega_i s + \omega_i^2)}{(s^4 + a_1 s^3 + a_2 s^2 + a_3 s + a_4)} \quad (113)$$

where

$$a_1 = 2\zeta_i \omega_i + B^{(i)}$$

$$a_2 = \omega_i^2 - \mu_\alpha + B^{(i)} \left(2\zeta_k \omega_k + \frac{1}{K_R} \right)$$

$$a_3 = -2\zeta_i \omega_i \mu_\alpha + B^{(i)} \left(\omega_k^2 + \frac{2\zeta_k \omega_k}{K_R} \right)$$

$$a_4 = -\mu_\alpha \omega_i^2 + B^{(i)} \frac{\omega_k^2}{K_R}$$

$$B^{(i)} = K_A K_R \mu_c A^{(i)}$$

We may apply the conventional root-locus technique to the open-loop transfer function, Eq. (113). The "variable" open-loop gain is now $1/K'_c$ instead of K_A as in the usual case.

Using the data for a typical launch vehicle,* the pole-zero configuration for Eq. (113) would appear as shown in Fig. 41. Note that for this case, the aerodynamic and bending-mode effects appear as open-loop zeros rather than open-loop poles. (Compare with Figs. 21-24.) The complex pole pair of lower frequency in Fig. 41 is associated with the rigid-body mode, while three possible locations are shown for the complex pole pair due to bending. Three different loci are thus possible, depending on whether the bending pole in Fig. 41 is above or below the bending zero, or whether

*See Appendix A.

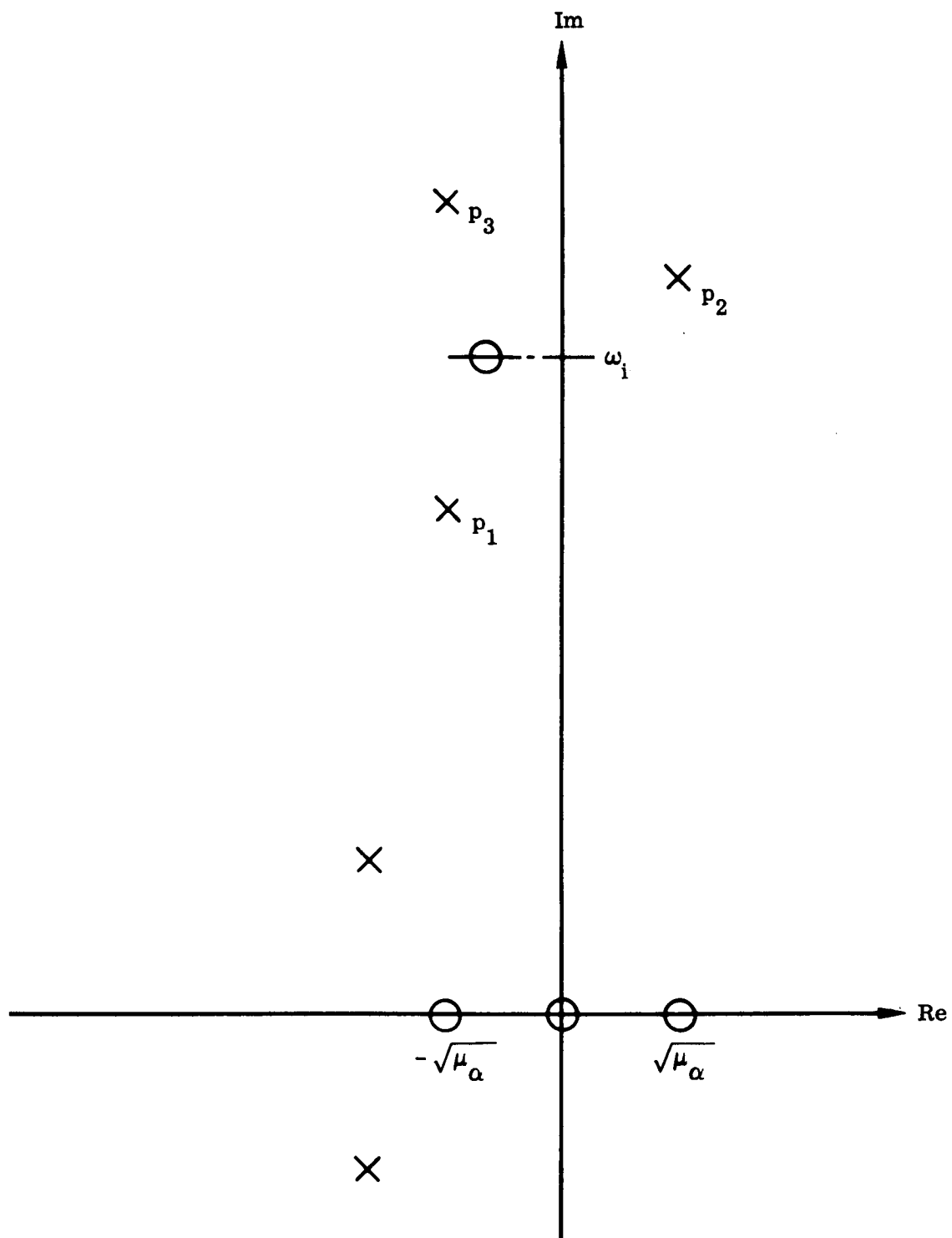


Figure 41. Pole-zero Configuration for Eq. (113)

it is in the right-half plane. The location, in fact, directly depends on the value of $A^{(i)}$ and roughly corresponds to the three conditions discussed on page . We seek to determine the (possible) existence of limit cycles for this system.

Consider first the pole location, p_1 . The bending-mode locus for this case is shown in Fig. 42 in enlarged form. Suppose a disturbance applied to the system produces an engine amplitude, $\bar{\delta}$. This corresponds to a certain value of K'_c and, in turn, to a definite value for $1/K'_c$. The closed-loop pole is then always in the left-half plane, which means that $\bar{\delta}$ decreases so that $1/K'_c$ always increases. In other words, whatever the size of $\bar{\delta}$ induced by the disturbance, the system will always return to a quiescent state.

A somewhat different situation prevails in Fig. 43. If a disturbance produces a value of $\bar{\delta}$ such that the corresponding K'_c results in a gain, $1/K'_c$, located at point B, $\bar{\delta}$ decreases since this closed-loop pole is stable. Then $1/K'_c$ increases and the zero is approached, which means that a quiescent condition is reached. However, a larger disturbance will produce a $1/K'_c$ located at point C, which means that $\bar{\delta}$ will increase and that $1/K'_c$ will decrease. The closed-loop pole will move to the right, toward the open-loop pole; this, in turn, implies that the oscillation increases without bound (explosive instability). Point A is therefore an unstable limit cycle.

It is a straightforward matter to calculate the engine amplitude angle, $\bar{\delta}$, corresponding to the unstable limit cycle. One merely calculates the gain, $1/K'_{c_2}$, at point A by conventional root-locus methods. Then, using the relations for K'_c , \bar{C}_f , and \bar{C}_L , defined after Eqs. (109) and (110), one solves for $\bar{\delta}$, using the given system parameters with $\omega = \omega_i$.

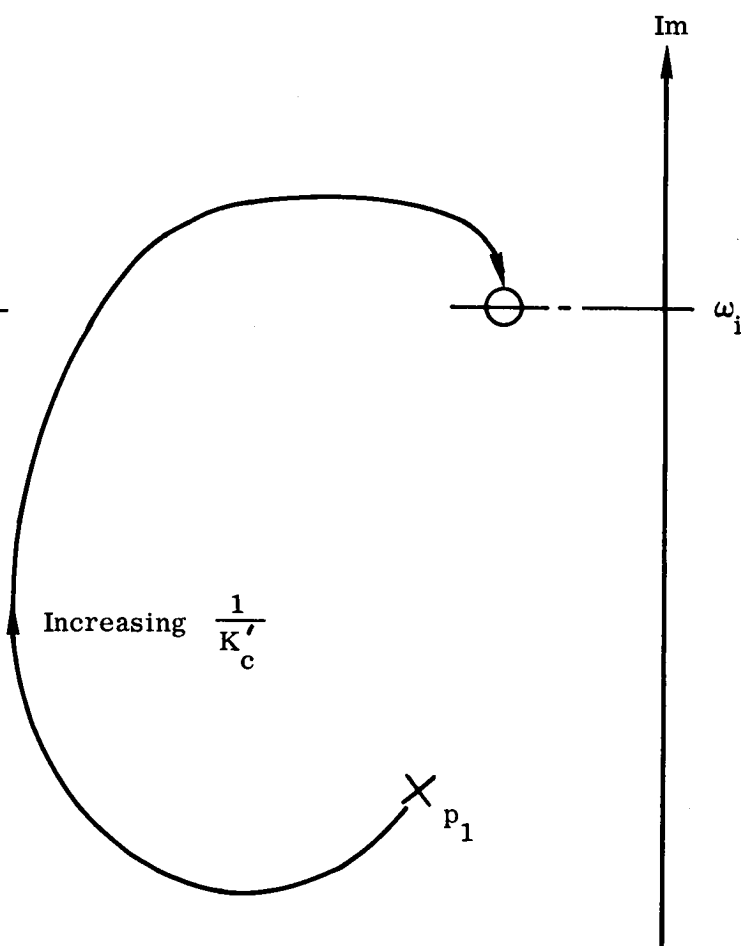


Figure 42. Root Locus for Pole Position p_1

Finally for the pole location shown in Fig. 44, one finds, using the same reasoning as above, that point B is a stable limit cycle, while point A is an unstable limit cycle. In other words, if a disturbance causes an engine amplitude $\bar{\delta}$ such that $1/K'_C$ is located at point C, the motion will die out. A larger disturbance will result in a limit cycle whose amplitude and frequency are determined by point B.

The above methods have been remarkably successful in predicting bending and sash mode limit cycles for launch vehicle autopilots. They are an indispensable supplement to the linear methods of analysis for this class of vehicle.

3.3.4 Approximations

The analytical methods considered thus far have been based on various approximations of the system dynamics. These have been necessary so that the salient features of the stability and response of the system could be highlighted. In the preliminary stages of analysis it is neither necessary nor desirable to perform a complete computer simulation, for two reasons. First, such a procedure is highly uneconomical in terms of time and money; and second, no rational basis is provided whereby certain response features are related to specific parameter values. The use of a simplified mathematical model does provide a foundation for analyzing and predicting performance qualities of the system. It is necessary, however, to justify the use of a particular model, either by complete computer simulation or by some analytical means.

In this section, we will consider various methods of evaluating the errors introduced by the simplifications employed throughout this monograph.

3.3.4.1 Aerodynamic Damping

The rigid-body pitching motion is given by Eqs. (21) and (26), the latter of which contains all the coupling terms with other modes. Assuming for the moment that the pitching motion is excited only by engine angle deflection, and including the effect of aerodynamic damping, we have

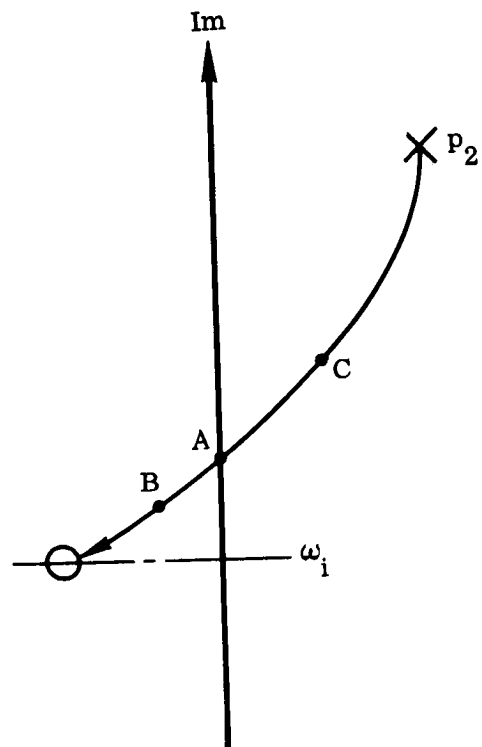


Figure 43. Root Locus for Pole Position p_2

$$\frac{\theta}{\delta} = \frac{\mu_c}{(s^2 + \mu_{\dot{\theta}} s + \mu_{\alpha})}$$

where

$$\mu_{\dot{\theta}} = \frac{1}{2} \rho U_0 A_2 \int_0^L \frac{\partial C_N(\ell)}{\partial \alpha} \times (\ell_a - \ell) d\ell \quad (115)$$

and having assumed that $\alpha \approx \theta$.

Eq. (114) differs from the transfer function, (55), by the presence of the $\mu_{\dot{\theta}}$ term, which arises from aerodynamic damping. For launch vehicles having no appreciable aerodynamic surfaces, this damping term is very small. Its effect is illustrated in Fig. 45, which represents the root locus for the simplified autopilot. With no aerodynamic damping, the pitching-mode poles are located symmetrically about the imaginary axis. Inclusion of the damping term merely shifts these poles slightly to the left. The percentage error introduced by neglecting this damping is generally less than the percentage error in other aerodynamic parameters. Its omission, then, is clearly justified.

While the aerodynamic damping has a negligible effect on the rigid-body response, it may have a significant effect on the bending-mode response. To see this, we write Eq. (29) as follows.*

$$\left(s^2 + 2 \zeta_i \omega_i s + \omega_i^2 \right) q^{(i)} = - \frac{1}{M^{(i)}} \left[T_c \delta + \mu_{\dot{q}}^{(i)} \dot{q}^{(i)} \right] \quad (116)$$

*Mode shapes have been normalized at the engine gimbal point, which means that $\varphi^{(i)}(\ell_T) = 1$.

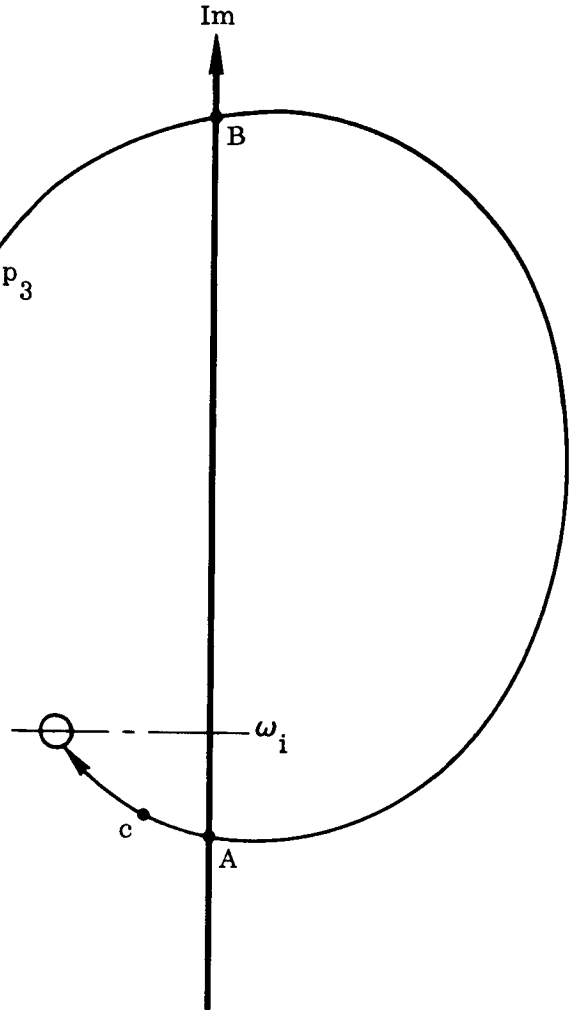


Figure 44. Root Locus for Pole Position p_3

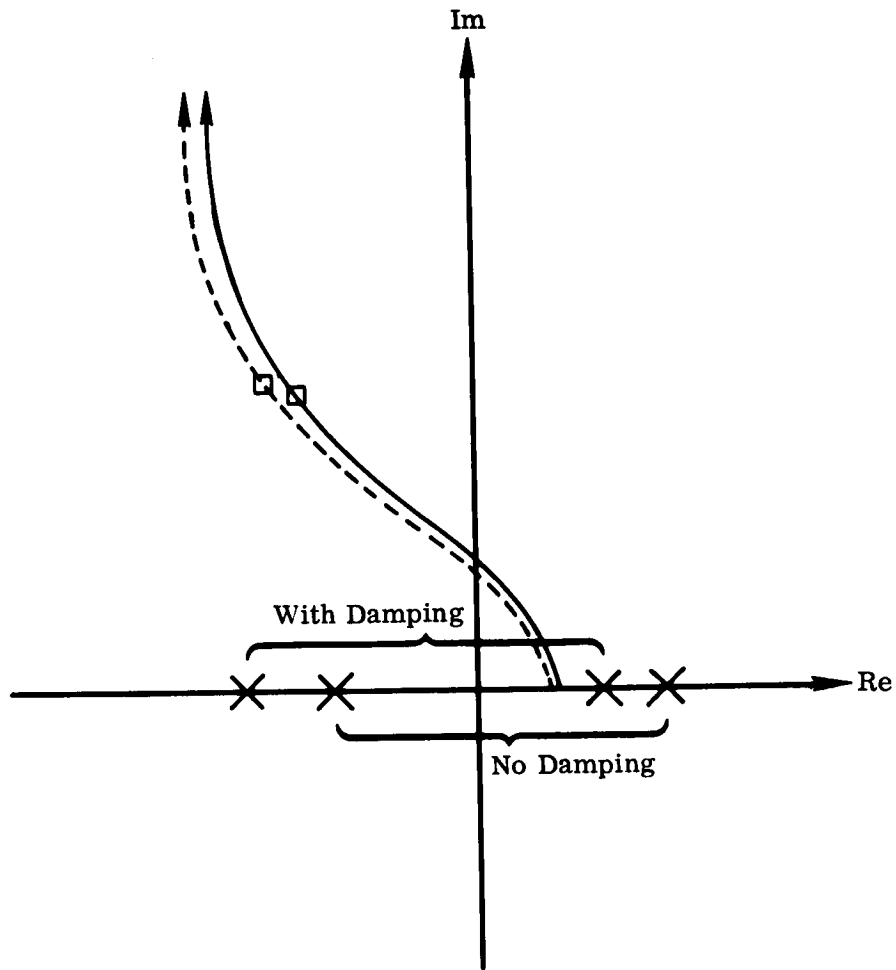


Figure 45. Effect of Aerodynamic Damping on Pitching Mode

where

$$\mu_{\dot{q}}^{(i)} = \frac{1}{2} \rho U_0 A_1 \int_0^L \frac{\partial C_N^{(l)}}{\partial \alpha} \varphi^{(i)}(l) dl \quad (117)$$

Thus, the effective relative damping factor is given by

$$\zeta'_i = \zeta_i + \frac{\mu_{\dot{q}}^{(i)}}{2 \omega_i M^{(i)}} \quad (118)$$

ζ_i represents the structural damping, which is very small (on the order of 0.02). However, the second term on the right-hand side of the above equation is often

of the same order of magnitude as ζ_i . It has the effect of shifting the bending pole-zero pair to the left as shown in Fig. 46. Since the higher bending modes are generally gain-stabilized, this term can have a crucial effect on bending stability. However, it acts only during the time when aerodynamic effects are appreciable. Consequently, omitting this term leads to a conservative analysis.

3.3.4.2 Modal Coupling

Coupling occurs either between orthogonal modes ($q^{(i)}$ to $q^{(j)}$) or nonorthogonal modes (slosh or plunging with pitching mode). Coupling between bending modes usually results from the aerodynamic and thrust terms, the latter of which are the more important. Consider, for example, *

$$\left(s^2 + 2\zeta_i \omega_i s + \omega_i^2\right) q^{(i)} = - \frac{1}{M^{(i)}} \left[T_c \delta - T_T \sigma_T^{(j)} q^{(j)} \right] \quad (119)$$

$$\left(s^2 + 2\zeta_j \omega_j s + \omega_j^2\right) q^{(j)} = - \frac{1}{M^{(j)}} \left[T_c \delta - T_T \sigma_T^{(i)} q^{(i)} \right] \quad (120)$$

Substituting $q^{(j)}$ from Eq. (120) into Eq. (119) yields

$$\frac{q^{(i)}}{\delta} = - \frac{T_c}{M^{(i)}} \frac{\left[G_j(s) + \frac{T_T \sigma_T^{(j)}}{M^{(j)}} \right]}{\left[G_i(s) G_j(s) - \frac{\sigma_T^{(i)} \sigma_T^{(j)} T_T^2}{M^{(i)} M^{(j)}} \right]} \quad (121)$$

where

$$G_i(s) = s^2 + 2\zeta_i \omega_i s + \omega_i^2$$

$$G_j(s) = s^2 + 2\zeta_j \omega_j s + \omega_j^2$$

In the absence of coupling between the two modes, we would have merely

$$\frac{q^{(i)}}{\delta} = - \frac{T_c}{M^{(i)}} \cdot \frac{1}{G_i(s)} \quad (122)$$

*We use the abbreviation $\sigma_T^{(j)} \equiv \sigma^{(j)}(\ell_T)$.

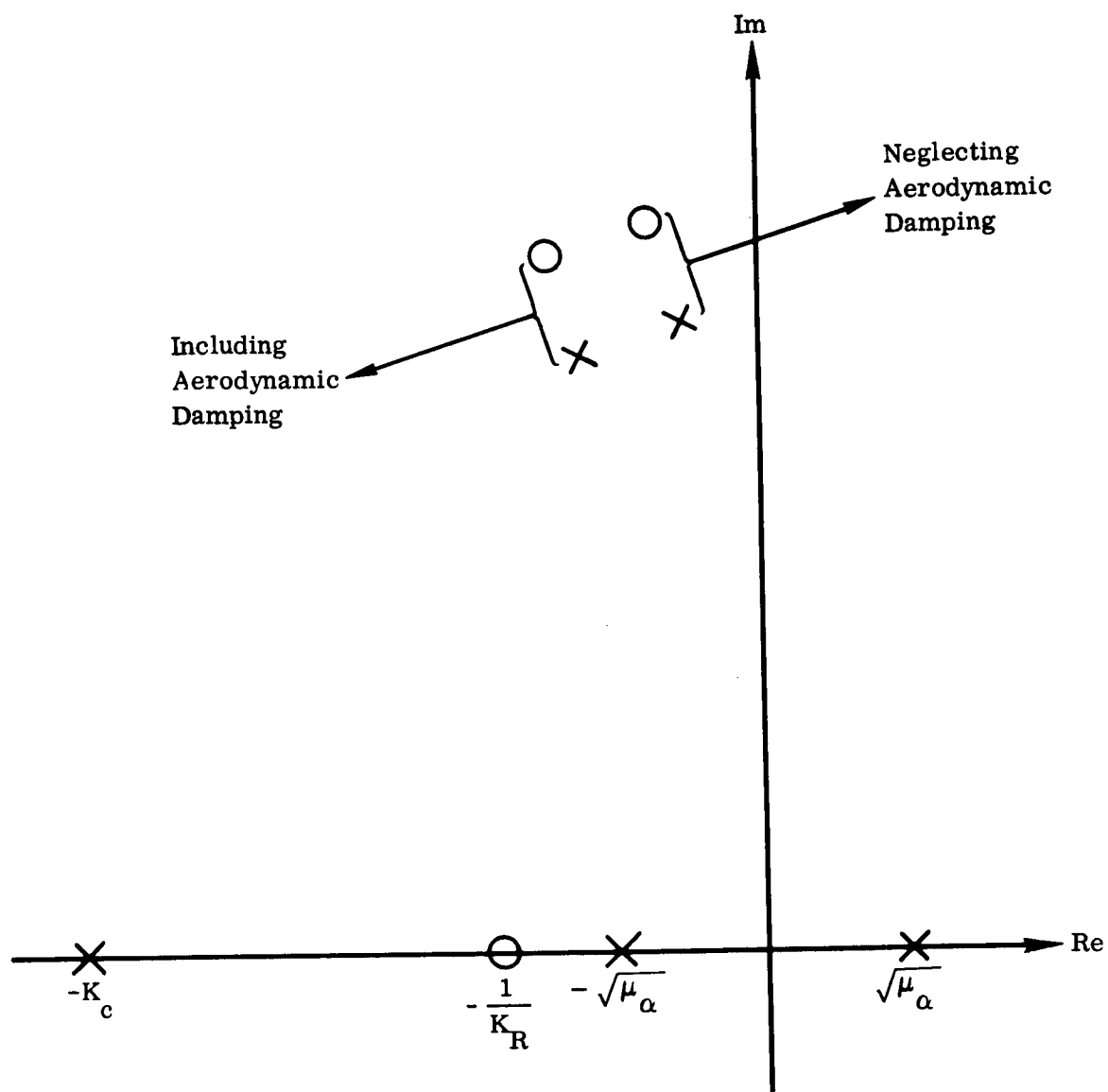


Figure 46. Effect of Aerodynamic Damping on Bending Mode

It is apparent that for

$$\frac{T_T \sigma_T^{(j)}}{M^{(j)}} \ll \omega_j^2$$

$$\frac{\sigma_T^{(i)} \sigma_T^{(j)} T_T^2}{M^{(i)} M^{(j)}} \ll \omega_i^2 \omega_j^2$$
(123)

the transfer functions, (121) and (122), are essentially the same. To examine a specific situation quantitatively, consider the first and second bending modes at $t = 152$ sec, the basic data of which are given in Appendix A. Substituting numerical values in Eqs. (121) and (122) we find*

$$\frac{T_T \sigma_T^{(1)}}{M^{(1)}} = -50.0$$

$$\frac{T_T \sigma_T^{(2)}}{M^{(2)}} = -71.1$$

$$\omega_1^2 = 1689$$

$$\omega_1^2 \omega_2^2 = 8.975 \times 10^6$$

It is easily verified that conditions (123) are indeed satisfied and that the coupling between bending modes is quite negligible.

The analysis of coupling between nonorthogonal modes follows a similar pattern. The influence of sloshing on the rigid-body mode, for example, may be ascertained from the root-locus plot of Fig. 47, which shows the case for two slosh pendulums. When the sloshing mode pole-zero pair are very close together (as is generally the case), the contribution in phase and gain to the control mode closed-loop pole is completely negligible. When such is not the case, plotting the open-loop poles and zeros, with a quick sketch of the resulting locus, ** will make this fact obvious.

*The engine swivel point, ℓ_T , is located at Station Number (SN) 1212.

**Detailed methods of performance analysis via pole-zero configurations are contained in Ref. 20.

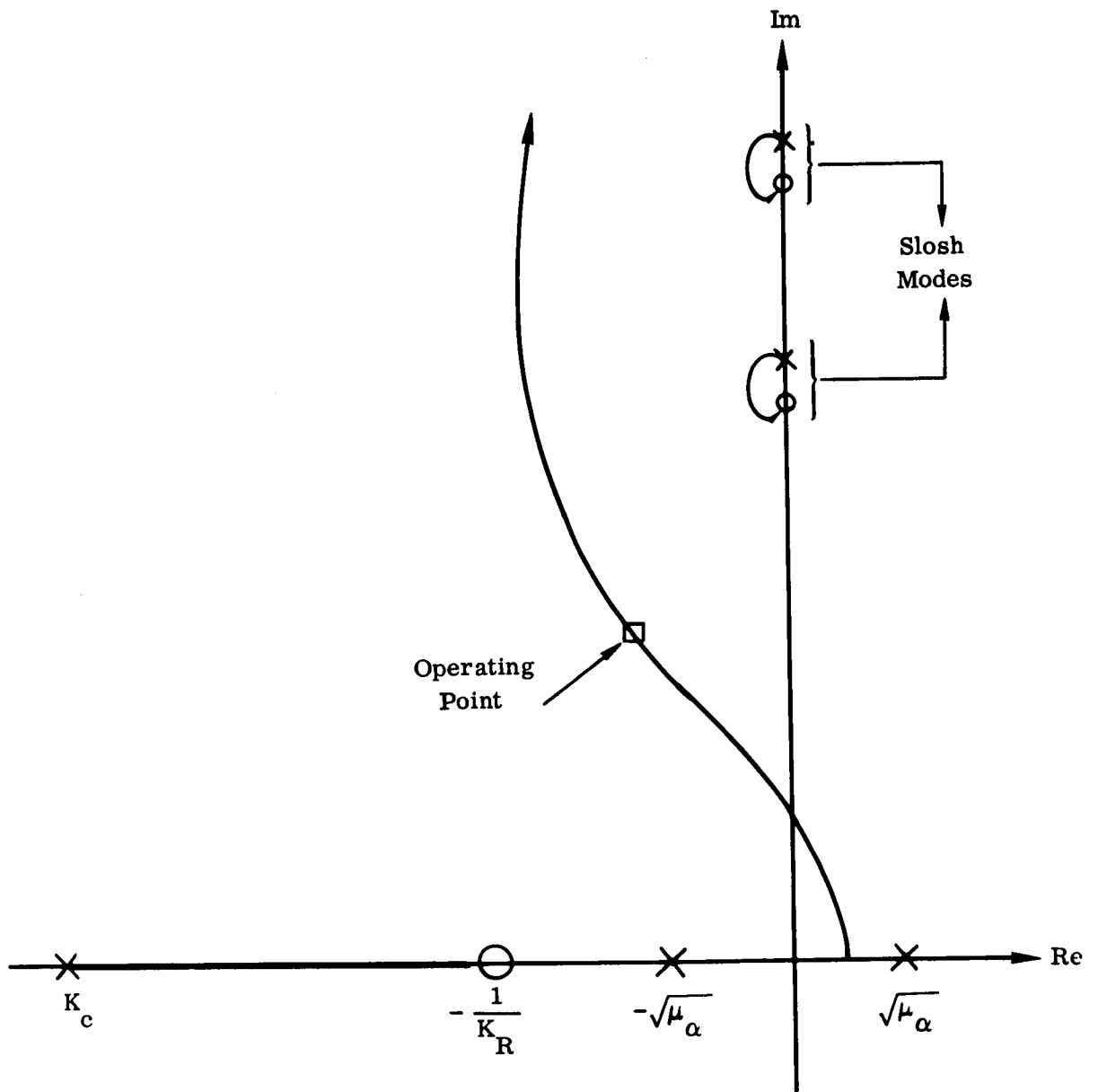


Figure 47. Influence of Sloshing Mode

3.3.4.3 Load Torque Feedback to Actuator

For purposes of preliminary analysis, the load torque feedback term, T_L , in the equation of actuator dynamics, (33), is generally neglected. As shown in Eq. (34), this term contains the acceleration feedbacks from the pitching, plunging, and bending modes. That due to pitching is usually the most significant. Let us take, therefore,*

$$T_L = m_R \ell_c^2 \ddot{\theta} + m_R \ell_c \dot{U}_0 \dot{\theta}$$

Assuming negligible aerodynamic effects, the θ/δ_c block diagram would appear as shown in Fig. 48. A simple manipulation yields the form shown in Fig. 49, which permits the analysis of the δ/δ_c transfer function more directly. We then have

$$\begin{aligned} \frac{\delta}{\delta_c} = & K_c \omega_c^2 / \left[s^3 + 2 \zeta_c \omega_c s^2 + \left(\omega_c^2 + \frac{\mu_c m_R \ell_R \ell_c^2}{K_c \omega_c^2 I_R} \right) s \right. \\ & \left. + \left(K_c \omega_c^2 + \frac{2 \zeta_c \omega_c \mu_c m_R \ell_R \ell_c^2}{K_c \omega_c^2 I_R} \right) \right] \end{aligned} \quad (124)$$

assuming that $\dot{U}_0/\ell_c \ll \omega_c$.

For most launch vehicles,

$$\frac{\mu_c m_R \ell_R \ell_c^2}{K_c \omega_c^2 I_R} \ll \omega_c^2$$

$$\frac{2 \zeta_c \omega_c \mu_c m_R \ell_R \ell_c^2}{K_c \omega_c^2 I_R} \ll K_c \omega_c^2$$

Therefore, the transfer function, (124), is essentially equivalent to (33), with T_L set equal to zero.

*We neglect I_R in comparison with $m_R \ell_c^2$.

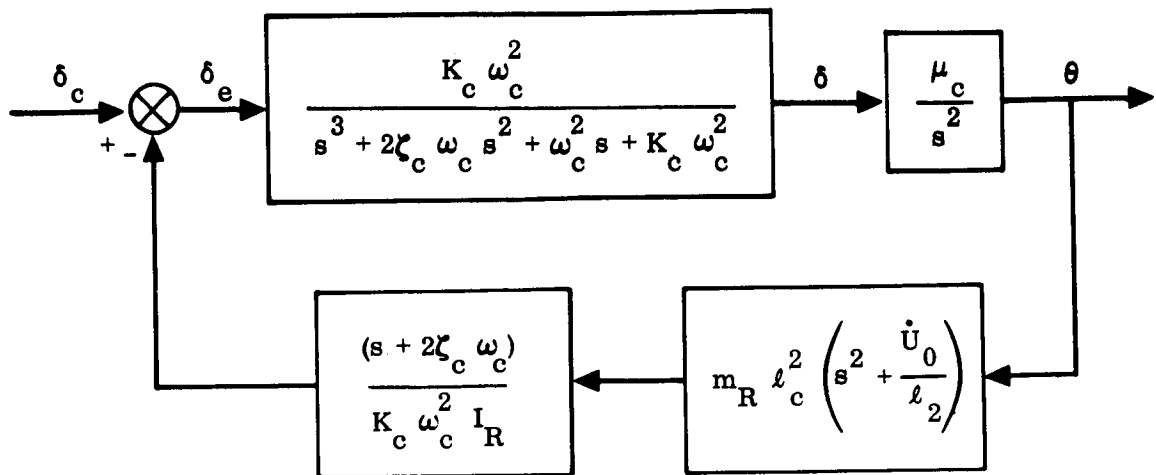


Figure 48. Load Torque Feedback to Actuator

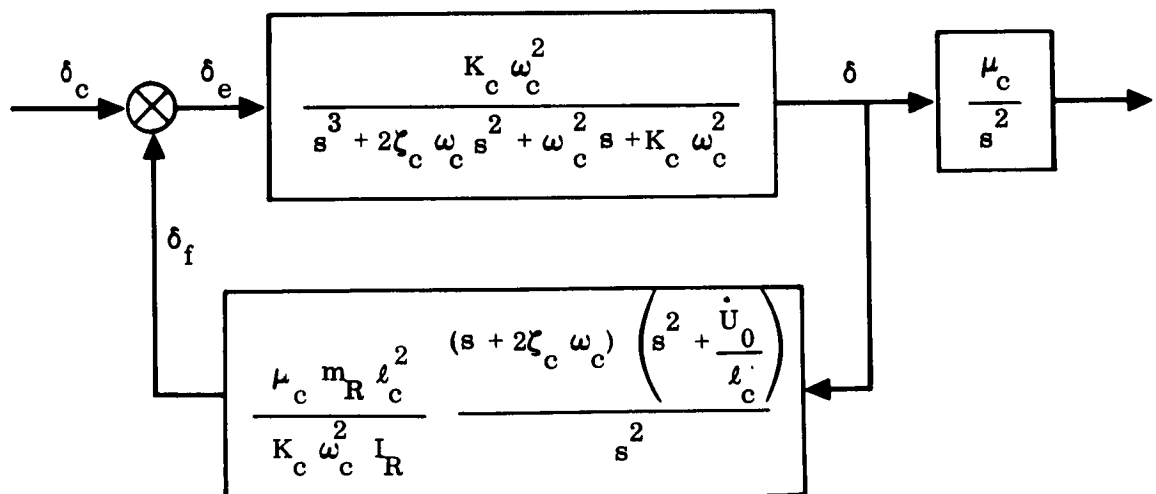


Figure 49. Alternate Form of Load Torque Feedback

3.3.4.4 Higher-Order Dynamic Effects

In studying the dynamic response properties of various modes, many well-known simplifications have been used. The most common has been to eliminate from consideration those modes that are far removed in frequency from the one being studied. Thus, for example, gyro dynamics are neglected when the essential features of the rigid-body mode are analyzed, since ω_R is much greater than the undamped natural frequency of θ . These factors are discussed in detail in another monograph. ⁽²⁰⁾

3.3.5 Complete Simulation

Using the techniques outlined thus far, one may, with a high level of confidence in satisfactory performance, formulate a fairly complete autopilot design. Since actual flight tests for design refinement are highly uneconomical, it is logical to simulate "flight" via computer. The simulation should include time-slice studies with all modes and nonlinearities accounted for, so that the stability properties of the system, especially the higher bending modes, can be validated. Such a simulation, with all higher-order actuator and instrumentation dynamic effects included, will then yield the proper gain and phase relationships, which are not easy to obtain in a simplified analysis. A lack of agreement between the theoretical and computer results should be carefully examined. Dismissing obvious numerical or computing program errors, this would indicate that certain parameters were more critical than supposed, or that particular analytical simplifications were not permissible.

Complete time-varying analog simulations should also be performed, especially for analyzing response to winds. Bending deflections should be included, since these have a significant effect in the induced bending loads.

Finally, actual flight traces, when compared with computer results, pinpoint problem areas. A good simulation serves to locate a possible malfunction and is an invaluable tool in providing a "fix."

4. REFERENCES

1. Greensite, A. Design Criteria for Control of Space Vehicles, Vol. I, part 1, Short Period Dynamics, General Dynamics Convair, Report GDC-DDE65-055, 1 Oct. 1965.
2. Schmitt, A., et al Approximate Transfer Functions for Flexible Booster and Autopilot Analysis, WADD TR-61-93, April 1961.
3. Geissler, E. D. "Problems in Attitude Stabilization of Large Guided Missiles," Aerospace Engr., Oct. 1960, p. 24.
4. Hoelker, R. F. Theory of Artificial Stabilization of Missiles and Space Vehicles with Exposition of Four Control Principles, NASA TN D-555, June 1961.
5. Lindberg, H. E. In Flight Dynamics of a Flexible Missile, Space Technology Laboratories Report STL/TR-60-0000-00083, 20 April 1960.
6. Rheinfurth, M. H. Control Feedback Stability Analysis, ABMA Report DA-TR-2-60, 11 Jan. 1960.
7. Bauer, H. F. Stability Boundaries of a Liquid Propelled Elastic Spacecraft, MSFC Report MTP-AERO-61-7, 17 Feb. 1961.
8. Greensite, A. "Analysis of Liquid Propellant Mode Stability of a Multitank Ballistic Booster Vehicle," J. Aero. Sci., Vol. 29, No. 2, 1962, p. 130.
9. Kachigan, K. The General Theory and Analysis of a Flexible Bodied Missile with Autopilot Control, General Dynamics Convair Report ZU7-048, 11 Nov. 1955.
10. Backus, F. I. Describing Functions for Nonlinear Electrohydraulic Gimballed Rocket Engine Position Servos with Application to Closed Loop Control Systems, General Dynamics Convair Report AE60-0287, 10 June 1960.

11. Greensite, A. Design Criteria for Control of Space Vehicles, Vol. I, part 3, Trajectory Equations, General Dynamics Convair Report GDC-DDE65-058, 1 Nov. 1965.
12. Beharrell, J. L., and Friedrich, H. R. "The Transfer Function of a Rocket Type Guided Missile with Consideration of its Structural Elasticity," J. Aero. Sci., 1954, p. 454.
13. Kachigan, K. Forced Oscillations of a Fluid in a Cylindrical Tank, General Dynamics Convair Report ZU-7-046, 4 Oct. 1955.
14. Lomen, D. O. Dynamic Behavior of Fluids Contained in Mobile Tanks of Arbitrary Shape, General Dynamics Convair Report ERR-AN-501, 11 May 1964.
15. Schmitt, A. F. Forced Oscillations of a Fluid in a Cylindrical Tank Undergoing Both Translation and Rotation, General Dynamics Convair Report ZU-7-069, 16 Oct. 1956.
16. Schmitt, A. F. Forced Oscillations of a Fluid in a Cylindrical Tank Oscillating in a Carried Acceleration Field - A Correction, General Dynamics Convair Report ZU-7-074, 4 Feb. 1957.
17. Pipes, L. A. Applied Mathematics for Engineers and Physicists, McGraw Hill Book Co., Inc., New York, N. Y., 1946.
18. Greensite, A. Design Criteria for Control of Space Vehicles, Vol. II, part 2, Nonlinear Systems, General Dynamics Convair Report GDC-DDE65-056, 1 Sept. 1965.
19. Greensite, A. A Note on the Determination of Limit Cycles in the Atlas Autopilot, General Dynamics Convair Memo CD-65-05-FUN, 7 Jan. 1965.
20. Greensite, A. Design Criteria for Control of Space Vehicles, Vol. II, part 1, Linear Systems, General Dynamics Convair Report GDC-DDE66-019, 25 April 1966.

APPENDIX A
BASIC DATA FOR A TYPICAL
LAUNCH VEHICLE

A.1 RIGID-BODY PARAMETERS

	UNITS	0.5 SEC	72 SEC	152 SEC
m_0	slugs	8225	5058	1670
I_{yy}	slug ft ²	3.25×10^6	2.42×10^6	1.50×10^6
\dot{U}_0	ft/sec ²	40.5	66.3	215.2
T_c	lb	308,000	342,000	356,000
L_α	lb/rad	0	198,000	9,000
l_c	ft	33.9	32.3	46.8
l_α	ft	-	34.1	18.6
U_0	ft/sec	-	-	-
μ_c	sec ⁻²	3.21	4.56	11.10
μ_α	sec ⁻²	0	2.80	.19
T_T	lb	366,100	418,900	436,400

A.2 SLOSH PARAMETERS

	UNITS	0.5 SEC	72 SEC	152 SEC
m_{P1}	slugs	113	388	239
m_{P2}	slugs	200	280	128
L_{P1}	ft	1.79	2.73	4.81
L_{P2}	ft	2.43	2.75	4.61
l_{P1}	ft	21.12	5.56	-18.52
l_{P2}	ft	-13.71	-20.62	-39.08
μ_{P1}	sec ⁻²	0.0297	0.0591	-0.6352
μ_{P2}	sec ⁻²	-0.0342	-0.1582	-0.7178

A.3 BENDING PARAMETERS

	UNITS	0.5 SEC	72 SEC	152 SEC
M ⁽¹⁾	slugs	2540	1590	1200
M ⁽²⁾	slugs	2470	9550	2260
M ⁽³⁾	slugs	4400	1840	1420
ω_1	rad/sec	16.5	18.9	41.1
ω_2	rad/sec	41.6	60.7	72.9
ω_3	rad/sec	67.4	87.1	238.0
$\sigma^{(1)}$, SN400	rad/ft	0.0384	0.0044	0.0623
$\sigma^{(2)}$, SN400	rad/ft	0.00192	-0.0276	0.0309
$\sigma^{(3)}$, SN400	rad/ft	-0.0770	-0.0813	-0.2902
$\sigma^{(1)}$, SN966	rad/ft	-0.0702	-0.0543	-0.1475
$\sigma^{(2)}$, SN966	rad/ft	0.1037	0.5672	0.2182
$\sigma^{(3)}$, SN966	rad/ft	-0.3281	-0.0951	-0.0290
A ⁽¹⁾ , SN400	N.D.	-0.45	0.793	-0.665
A ⁽²⁾ , SN400	N.D.	0.925	1.217	0.562
A ⁽³⁾ , SN400	N.D.	2.68	4.31	7.55
A ⁽¹⁾ , SN966	N.D.	3.65	3.56	4.94
A ⁽²⁾ , SN966	N.D.	-3.03	-3.45	-2.10
A ⁽³⁾ , SN966	N.D.	8.16	4.88	1.65
$\sigma^{(1)}$, SN1212	rad/ft	-0.0550	-0.0648	-0.1375
$\sigma^{(2)}$, SN1212	rad/ft	-0.1218	-0.1710	-0.3680
$\sigma^{(3)}$, SN1212	rad/ft	-0.2720	0.5650	0.3400

The engine swivel point is located at SN1212

A.4 ENGINE SERVO PARAMETERS

A	ft ²	2.47×10^{-2}
B	lb/ft ²	3.89×10^7
C _B	lb/ft	565
C _L	(ft ³ /sec)/√lb/ft ²	4.78×10^{-6}
C _V	lb ft/(rad/sec)	3.60×10^3
I _R	slug ft ²	377
K _a	ma/rad	340
K _m	lb/ft	1.12×10^6
K _V	(ft ³ /sec)/ma√lb/ft ²	7.125×10^{-6}
ℓ _R	ft	2.52
m _R	slugs	30.8
P _s	lb/ft ²	4.32×10^5
P _R	lb/ft ²	7.2×10^3
R	ft	1.77
V _T	ft ³	7.6×10^{-3}

The engine servo system configuration is shown in Figure A1. The symbols have the following meaning:

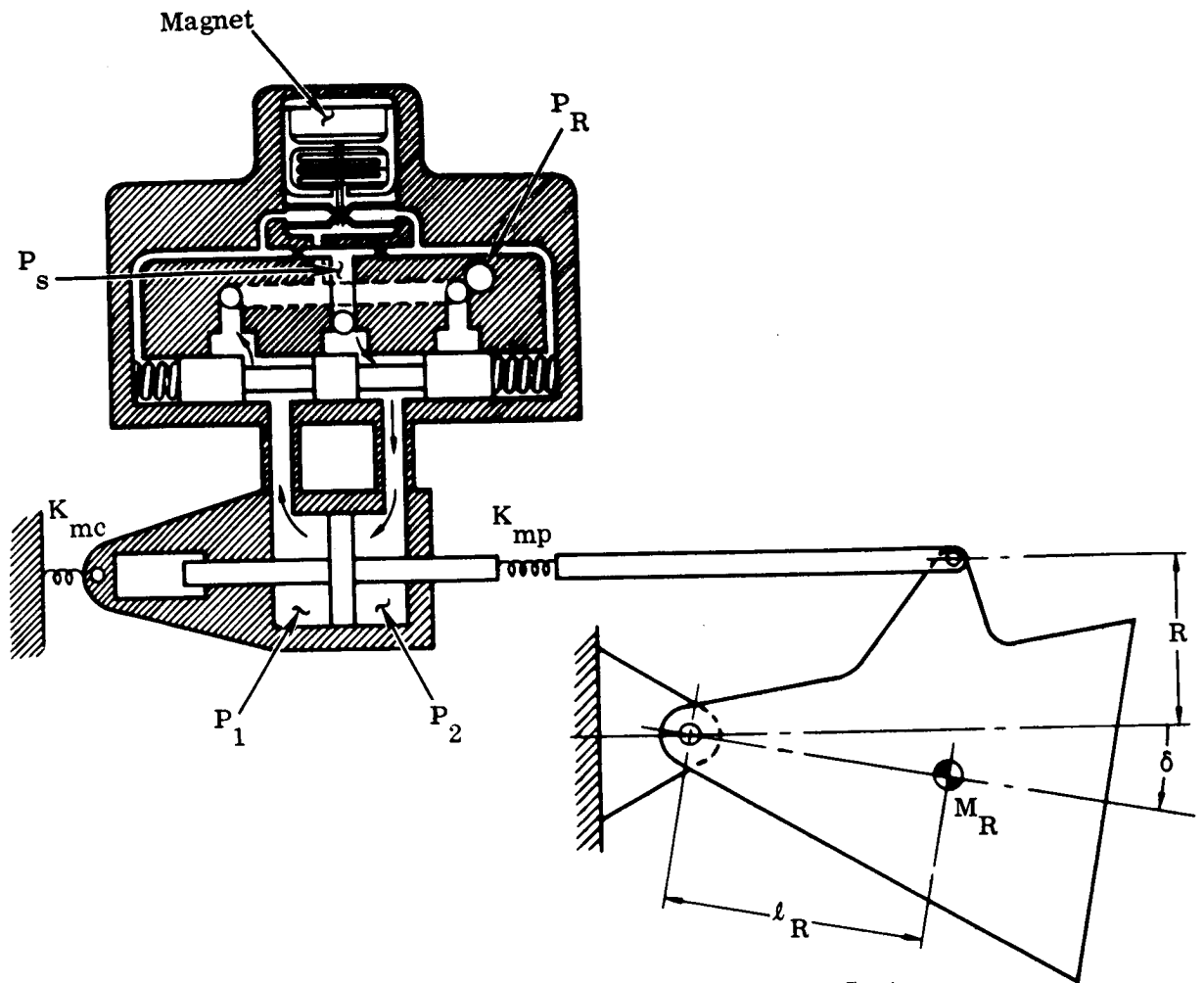


Figure A1. Schematic of Engine Servo System

- A = effective area of piston
- B = bulk modulus of hydraulic fluid
- C_B = coulomb friction coefficient of engine swivel point
- C_L = discharge coefficient for valve orifice
- C_V = viscous friction coefficient of engine swivel point
- I_R = moment of inertia of engine about swivel point
- K_σ = servo valve transducer gain
- K_m = effective spring constant of engine mount

K_V = valve flow gain constant

l_R = distance from mass center of engine to swivel point

m_R = mass of rocket engine

P_s = valve supply pressure

P_R = reservoir pressure

R = moment arm

V_T = total volume of hydraulic fluid under compression

Constant K_a is a combination of servo valve and transducer gain, which relates the valve current to the error signal in radians as follows.

$$i_v = K_a \left[\delta_c - \delta - \frac{AP_L}{K_m R} \right]$$

i_v = valve current, ma

P_L = pressure differential across actuator piston

The flow through the valve is given by

$$Q_v = K_v i_v \sqrt{P_v}$$

where P_v is the pressure differential across the valve orifice. Constant K_v is usually obtained from the $Q_v - i_v$ curves for several values of P_v . These are generally supplied by the valve manufacturer.

The effective mount compliance, K_m , is given by

$$\frac{1}{K_m} = \frac{1}{K_{mc}} + \frac{1}{K_{mp}}$$

where K_{mp} and K_{mc} are the piston rod and mount spring constants respectively.

APPENDIX B

MECHANICAL ANALOGY FOR LIQUID SLOSHING IN A CYLINDRICAL TANK

NOMENCLATURE

a = radius of tank

F = force

g = gravity acceleration

h = height of liquid in tank

$J_m ()$ = Bessel function of first kind of order m

\bar{k} = unit vector in positive z direction (see Fig. B1)

ℓ = length parameter (see Fig. B1)

ℓ_1 = distance from point of force application to pendulum hinge point (see Fig. B3)

ℓ_0 = distance from point of force application to center of mass (see Fig. B3)

L_p = length of pendulum

m_0 = mass of rigid body (see Fig. B3)

m_1 = mass of pendulum

M = total mass of fluid

p = pressure

q = velocity of fluid particle

s = Laplace operator

t = time

x = displacement of tank (see Fig. B1)

$Y_m ()$ = Bessel function of second kind of order m

z = longitudinal parameter

η = wave length of liquid measured from level surface

ξ_i = roots of Eq. (B55)

ρ = density of fluid

r, φ = cylindrical coordinates

Φ = velocity potential function

Ω = force potential function

∇ = gradient operator

$(\dot{}) = \frac{d}{dt} ()$

$\vec{}$ = vector

$\vec{A} \cdot \vec{B}$ = scalar product of A and B

$\vec{A} \times \vec{B}$ = vector product of A and B

B.1 INTRODUCTION

We consider here the problem of determining the forces and moments produced by the sloshing of a liquid in a cylindrical tank. Only the translational motion of the tank is considered, and the applied forces are assumed arbitrary. It is shown that the forces and moments produced by the liquid sloshing may be duplicated by an analogous mechanical configuration in which the sloshing liquid is replaced by a rigid mass and a series of pendulums. Only the simplest case is considered: that of a cylindrical tank subject to translation only.⁽¹³⁾ The case of combined translation and rotation has been analyzed by Schmitt,^(15,16) while tanks of arbitrary shape have been considered by Lomen.⁽¹⁴⁾

The development that follows proceeds from first principles in the theory of hydrodynamics.

B.2 METHOD OF SOLUTION

From the equation of continuity

$$\frac{\partial \rho}{\partial t} + \nabla \cdot (\rho \bar{q}) = 0 \quad (B1)$$

Assuming an incompressible fluid and irrotational flow, we obtain Laplace's equation

$$\nabla^2 \Phi = 0 \quad (B2)$$

which in cylindrical coordinates is expressed as

$$\frac{\partial^2 \Phi}{\partial r^2} + \frac{1}{r} \frac{\partial \Phi}{\partial r} + \frac{1}{r^2} \frac{\partial^2 \Phi}{\partial \varphi^2} + \frac{\partial^2 \Phi}{\partial z^2} = 0 \quad (B3)$$

In addition, we have the equation of motion

$$\frac{d\bar{q}}{dt} = \bar{F} - \frac{1}{\rho} \nabla p \quad (B4)$$

Now since

$$\frac{d\bar{q}}{dt} = \frac{\partial \bar{q}}{\partial t} + \bar{q} \cdot \nabla \bar{q} \quad (B5)$$

we have, on substituting (B5) in (B4),

$$\frac{\partial \bar{q}}{\partial t} + \bar{q} \cdot \nabla \bar{q} = \bar{F} - \frac{1}{\rho} \nabla p \quad (B6)$$

Using the rule for the gradient of a scalar product, viz.,

$$\nabla \bar{A} \cdot \bar{B} = \bar{A} \cdot \nabla \bar{B} + \bar{B} \cdot \nabla \bar{A} + \bar{A} \times (\nabla \times \bar{B}) + \bar{B} \times (\nabla \times \bar{A}) \quad (B7)$$

and observing that for irrotational motion

$$\nabla \times \bar{q} = 0 \quad (B8)$$

we find

$$\bar{q} \cdot \nabla \bar{q} = \frac{1}{2} \nabla \bar{q} \cdot \bar{q} = \nabla \left(\frac{1}{2} q^2 \right) \quad (B9)$$

Putting this in Eq. (B6) and using the fact that

$$\bar{F} = -\nabla \Omega \quad (B10)$$

we obtain

$$\frac{\partial q}{\partial t} + \nabla \left(\frac{1}{2} q^2 \right) = -\nabla \Omega - \frac{1}{\rho} \nabla p \quad (B11)$$

Or, since

$$\bar{q} = -\nabla \Phi \quad (B12)$$

we find

$$-\nabla \left(\frac{\partial \Phi}{\partial t} \right) + \nabla \left(\frac{1}{2} q^2 \right) = -\nabla \Omega - \frac{1}{\rho} \nabla p \quad (B13)$$

Forming the scalar product of both sides of this equation by $d\bar{l}$ gives

$$-d \left(\frac{\partial \Phi}{\partial t} \right) + d \left(\frac{1}{2} q^2 \right) = -d\Omega - \frac{1}{\rho} dp \quad (B14)$$

which, on integration, becomes

$$\int \frac{dp}{\rho} + \Omega + \frac{1}{2} q^2 - \frac{\partial \Phi}{\partial t} = B(t) \quad (B15)$$

where $B(t)$, in general, is a function of time, since the integration was performed with respect to the spatial coordinates only.

If the fluid is incompressible, $\rho = \text{a constant}$ and Eq. (B15) becomes

$$p = \rho \left[\frac{\partial \Phi}{\partial t} - \Omega - \frac{1}{2} q^2 + B(t) \right] \quad (\text{B16})$$

We note, incidentally, that if the motion is steady, Φ does not depend on time, and we obtain Bernoulli's equation

$$\frac{p}{\rho} + \Omega + \frac{1}{2} q^2 = \text{a constant} \quad (\text{B17})$$

The equation for static pressure may be obtained from Eq. (B6) with $\bar{q} = 0$; i.e.,

$$\rho \bar{F} = \nabla p_s \quad (\text{B18})$$

The only body force is gravity acting in the negative Z direction. (See Fig. B1.)

$$\bar{F} = -\bar{k}g \quad (\text{B19})$$

so that

$$\nabla p_s = -\rho \bar{k}g \quad (\text{B20})$$

Taking the scalar product of both sides by $d\bar{l}$, we have

$$dp_s = -\rho g dz \quad (\text{B21})$$

or

$$p_s = -\rho g z + p_0 \quad (\text{B22})$$

where we have used the fact that $p_s = p_0$ at $z = 0$.

To obtain an expression for the dynamic pressure only, we neglect \bar{F} in Eq. (B6), obtaining in place of (B16)

$$p_0 = \rho \left[\frac{\partial \Phi}{\partial t} - \frac{1}{2} q^2 + B(t) \right] \quad (\text{B23})$$

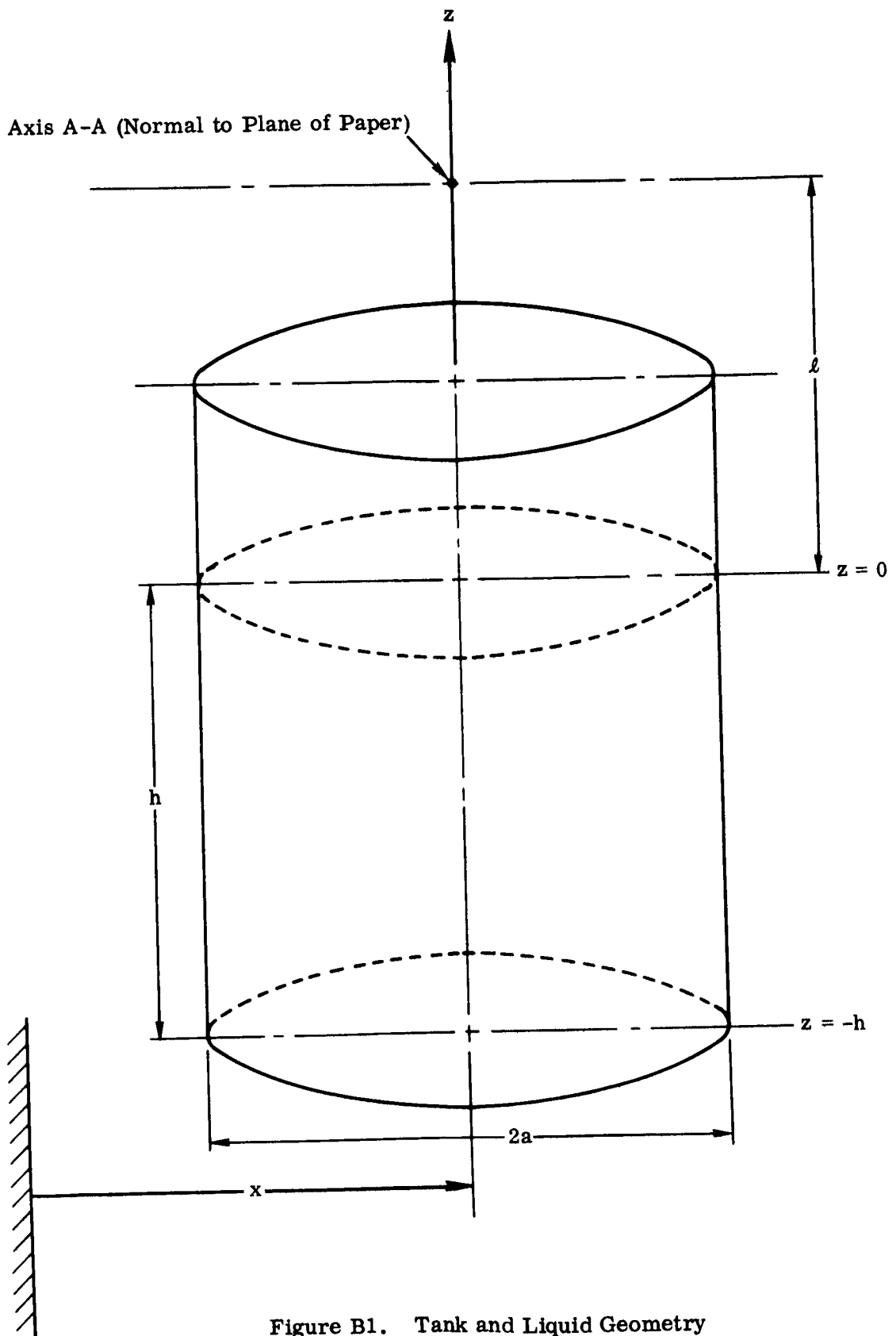


Figure B1. Tank and Liquid Geometry

If the velocity is small, the $\frac{1}{2} q^2$ term may be neglected. Assuming steady-state initial conditions at $t = 0$, Eq. (B23) reduces to

$$p_0 = \rho \frac{\partial \Phi}{\partial t} \quad (\text{B24})$$

The problem now reduces to solving the Laplace equation for prescribed boundary conditions and then determining p_0 at the tank walls from Eq. (B24).

Now at the surface of the fluid we must have

$$\frac{dp}{dt} = 0 \quad (\text{B25})$$

Taking Eq. (B16), neglecting the $\frac{1}{2} q^2$ term, and writing $+gz$ for Ω (since gravity is the only extraneous force), we obtain, on differentiating with respect to time,

$$\frac{dp}{dt} = \rho \left[\frac{\partial^2 \Phi}{\partial t^2} - g \frac{dz}{dt} \right] \quad (\text{B26})$$

under the aforementioned initial conditions. By virtue of (B25), we have, therefore,

$$\frac{\partial^2 \Phi}{\partial t^2} + g \frac{\partial \Phi}{\partial z} = 0 \quad \text{at } z = \eta \quad (\text{B27})$$

where we have put

$$\frac{\partial \Phi}{\partial z} = - \frac{dz}{dr} \quad (\text{B28})$$

If η is small compared to h , we have

$$\frac{\partial^2 \Phi}{\partial t^2} + g \frac{\partial \Phi}{\partial z} = 0 \quad \text{at } z = 0 \quad (\text{B29})$$

The boundary condition at the bottom of the tank is

$$\frac{\partial \Phi}{\partial z} = 0 \quad \text{at } z = -h \quad (\text{B30})$$

If the velocity of the cylinder in the horizontal direction is \dot{x} , then the boundary condition at the tank walls must be

$$\frac{\partial \Phi}{\partial r} = -\dot{x} \cos \varphi \quad \text{at } r = a \quad (\text{B31})$$

To recapitulate, we must first solve the equation

$$\frac{\partial^2 \Phi}{\partial r^2} + \frac{1}{r} \frac{\partial \Phi}{\partial r} + \frac{1}{r^2} \frac{\partial^2 \Phi}{\partial \varphi^2} + \frac{\partial^2 \Phi}{\partial z^2} = 0 \quad (\text{B32})$$

where the boundary conditions are as follows

At the walls

$$\frac{\partial \Phi}{\partial r} = -\dot{x} \cos \varphi \quad \text{at } r = a \quad (\text{B33})$$

At the bottom

$$\frac{\partial \Phi}{\partial z} = 0 \quad \text{at } z = -h \quad (\text{B34})$$

At the surface

$$\frac{\partial^2 \Phi}{\partial t^2} + g \frac{\partial \Phi}{\partial z} = 0 \quad \text{at } z = 0 \quad (\text{B35})$$

Assume a solution of the form

$$\Phi = R(r) \cdot \Psi(\varphi) \cdot Z(z) \quad (\text{B36})$$

where

$R(r)$ is a function of r only

$\Psi(\varphi)$ is a function of φ only

$Z(z)$ is a function of z only

Substituting (B36) in (B32) gives

$$\frac{1}{Z} \frac{d^2 Z}{dz^2} = -\frac{1}{R} \frac{d^2 R}{dr^2} - \frac{1}{Rr} \frac{dR}{dr} - \frac{1}{r^2 \Psi} \frac{d^2 \Psi}{d\varphi^2} \quad (\text{B37})$$

Since the right-hand side of this equation does not vary with z , it follows that

$$\frac{1}{Z} \frac{d^2 Z}{dz^2} = K^2 \quad (\text{B38})$$

where K is a constant. Substituting this back in Eq. (B37) results in

$$\frac{r^2}{R} \frac{d^2 R}{dr^2} + \frac{r}{R} \frac{dR}{dr} + K^2 r^2 = -\frac{1}{\Psi} \frac{d^2 \Psi}{d\varphi^2} \quad (\text{B39})$$

so that

$$-\frac{1}{\Psi} \frac{d^2 \Psi}{d\varphi^2} = m^2 \quad (\text{B40})$$

where m is a constant. Combining (B39) and (B40) gives

$$r^2 \frac{d^2 R}{dr^2} + r \frac{dR}{dr} + (K^2 r^2 - m^2) = 0 \quad (\text{B41})$$

The solution of Eq. (B38) is

$$Z = c_1 \sinh (Kz) + c_2 \cosh (Kz) \quad \text{for } K \neq 0 \quad (\text{B42})$$

$$Z = c_3 z + c_4 \quad \text{for } K = 0 \quad (\text{B43})$$

Solving Eq. (B40) gives

$$\Psi = c_5 \cos m\varphi + c_6 \sin m\varphi \quad (\text{B44})$$

Eq. (B41) can be reduced to the standard form of Bessel's equation. Its solution is

$$R = c_7 J_m(Kr) + c_8 Y_m(Kr) \quad \text{for } K \neq 0 \quad (\text{B45})$$

$$R = c_9 r^m + c_{10} r^{-m} \quad \text{for } K = 0 \quad (\text{B46})$$

If the solution is single-valued, then Ψ in Eq. (B44) must not change when φ is increased by 2π . Hence m must be an integer; the solution of Eq. (B41) must therefore involve the Bessel function of the second kind as indicated in (B45).

There are two solutions for Φ , depending on whether or not K equals zero; i.e.,

$$\Phi_0 = (c_9 r^m + c_{10} r^{-m})(c_5 \cos m\varphi + c_6 \sin m\varphi)(c_3 z + c_4) \quad (\text{B47})$$

$$\Phi_K = \left[c_7 J_m(Kr) + c_8 Y_m(Kr) \right] (c_5 \cos m\varphi + c_6 \sin m\varphi) \left[c_1 \sinh(Kz) + c_2 \cosh(Kz) \right] \quad (\text{B48})$$

A more general solution is given by a superposition of both.

$$\Phi = \Phi_0 + \Phi_K \quad (\text{B49})$$

The constants in the general solution can be determined by utilizing the boundary conditions.

The boundary conditions at the cylinder wall can be fulfilled by

$$\left. \begin{aligned} \frac{\partial \Phi_0}{\partial r} &= -\dot{x} \cos \varphi \\ \frac{\partial \Phi_K}{\partial r} &= 0 \end{aligned} \right\} \text{ at } r = a \quad (\text{B50})$$

$$\left. \begin{aligned} \frac{\partial \Phi_0}{\partial r} &= -\dot{x} \cos \varphi \\ \frac{\partial \Phi_K}{\partial r} &= 0 \end{aligned} \right\} \text{ at } r = a \quad (\text{B51})$$

From (B47) and (B50),

$$(c_9 m a^{m-1} - c_{10} m a^{-m-1})(c_5 \cos m\varphi + c_6 \sin m\varphi)(c_3 z + c_4) = -\dot{x} \cos \varphi \quad (\text{B52})$$

from which it follows that

$$\left\{ \begin{aligned} c_3 &= c_6 = c_{10} = 0 \\ m &= 1 \\ c_9 c_5 c_4 &= -\dot{x} \end{aligned} \right.$$

Therefore,

$$\Phi_0 = -\dot{x} r \cos \varphi \quad (\text{B53})$$

Now $Y_1(0) = \infty$ at $r = 0$. Since this is not compatible with the physical problem involved, it follows that $c_8 = 0$. Combining the resulting Eq. (B48) with Eq. (B51), we have

$$c_7 c_5 J_1'(Ka) \cos \varphi \left[c_1 \sinh(Kz) + c_2 \cosh(Kz) \right] = 0 \quad (B54)$$

where the prime denotes derivative with respect to r . Eq. (B54) requires that

$$J_1'(Ka) = 0 \quad (B55)$$

An infinite number of positive real roots satisfy Eq. (B55). Denote these by $\xi_1, \xi_2, \dots, \xi_n$. With each ξ_k , a corresponding solution can be associated. We have, therefore,

$$\Phi = -\dot{x} r \cos \varphi + \sum_{n=1}^{\infty} c_n J_1 \left(\xi_n \frac{r}{a} \right) \cos \varphi \left[c_{n1} \sinh \left(\xi_n \frac{z}{a} \right) + c_{n2} \cosh \left(\xi_n \frac{z}{a} \right) \right] \quad (B56)$$

where for $J_1'(\xi_n) = 0$

$$\xi_1 = 1.840$$

$$\xi_2 = 5.335$$

$$\xi_3 = 8.535$$

$$\xi_4 = 11.705$$

$$\xi_5 = 14.850$$

$$\xi_k \approx \xi_{k-1} + \pi \quad \text{for } n > 5$$

and where the constants are written with the subscript to emphasize their dependence on n .

To fulfill the boundary conditions at the bottom of the tank, Eq. (B34), we must have

$$\sum_{n=1}^{\infty} c_n J_1 \left(\xi_n \frac{r}{a} \right) \cos \varphi \left[c_{n1} \cosh \left(\xi_n \frac{h}{a} \right) - c_{n2} \sinh \left(\xi_n \frac{h}{a} \right) \right] \frac{\xi_n}{a} = 0 \quad (B57)$$

This requires that the expression inside the brackets vanish, or

$$c_{n1} = c_{n2} \frac{\sinh \left(\xi_n \frac{h}{a} \right)}{\cosh \left(\xi_n \frac{h}{a} \right)} \quad (B58)$$

Substituting this in (B56) and writing β_n for $c_n c_{n2}$, we obtain

$$\Phi = -x r \cos \varphi + \sum_{n=1}^{\infty} \beta_n J_1 \left(\xi_n \frac{r}{a} \right) \frac{\cos \varphi}{\cosh \left(\xi_n \frac{h}{a} \right)} \cosh \left[\frac{\xi_n}{a} (h + z) \right] \quad (\text{B59})$$

β_n may be determined by satisfying the boundary condition at the surface, Eq. (B35).

From (B35) and (B59), we have

$$\left. \frac{\partial^2 \Phi}{\partial t^2} \right|_{z=0} = -s^3 x(s) r \cos \varphi + \sum_{n=1}^{\infty} s^2 \beta_n(s) J_1 \left(\xi_n \frac{r}{a} \right) \cos \varphi$$

$$\left. g \frac{\partial \Phi}{\partial z} \right|_{z=0} = \sum_{n=1}^{\infty} \omega_n^2 \beta_n J_1 \left(\xi_n \frac{r}{a} \right) \cos \varphi$$

where

$$\omega_n^2 = \frac{g \xi_n}{a} \tanh \left(\xi_n \frac{h}{a} \right)$$

or

$$-s^3 x(s) r \cos \varphi + \sum_{n=1}^{\infty} J_1 \left(\xi_n \frac{r}{a} \right) (s^2 + \omega_n^2) \beta_n(s) \cos \varphi = 0 \quad (\text{B60})$$

where we have used the Laplace operational notation, since all initial conditions are zero.

Multiplying both sides of Eq. (B60) by $r J_1 \left(\xi_m \frac{r}{a} \right) dr$ and integrating between the limits of 0 and a , we have

$$\begin{aligned} & -s^3 x(s) \cos \varphi \int_0^a r^2 J_1 \left(\xi_m \frac{r}{a} \right) dr \\ & + \sum_{n=1}^{\infty} (s^2 + \omega_n^2) \beta_n(s) \cos \varphi \int_0^a r J_1 \left(\xi_m \frac{r}{a} \right) J_1 \left(\xi_n \frac{r}{a} \right) dr = 0 \end{aligned} \quad (\text{B61})$$

By virtue of the orthogonality properties of the Bessel functions*

$$\int_0^a r J_1\left(\xi_m \frac{r}{a}\right) J_1\left(\xi_n \frac{r}{a}\right) dr = 0 \quad \text{for } n \neq m \quad (\text{B62})$$

with

$$J_1'(\xi_n) = J_1'(\xi_m) = 0 \quad (\text{B63})$$

When $n = m$, we have*

$$\int_0^a r J_1^2\left(\xi_n \frac{r}{a}\right) dr = \frac{a^2}{2} J_1(\xi_n) J_1''(\xi_n) \quad (\text{B64})$$

We may evaluate $J_1''(\xi_n)$ in terms of $J_1(\xi_n)$ as follows.

Since (primes now denoting derivatives with respect to y)

$$\begin{aligned} y J_1''(y) &= \frac{d}{dy} [y J_1'(y)] - J_1'(y) \\ &= \frac{d}{dy} [J_1(y) - y J_2(y)] - J_1'(y) \\ &= J_1'(y) - \frac{d}{dy} [y J_2(y)] - J_1'(y) \\ &= -\frac{d}{dy} \left[\frac{1}{y} y^2 J_2(y) \right] \\ &= -\frac{1}{y} \frac{d}{dy} [y^2 J_2(y)] - y^2 J_2(y) \frac{d}{dy} \left(\frac{1}{y} \right) \\ &= -\frac{1}{y} y^2 J_1(y) + J_2(y) \end{aligned}$$

$$y^2 J_1''(y) = -y^2 J_1(y) + y J_2(y) = -y^2 J_1(y) + J_1(y) - y J_1'(y)$$

* Ref. 17, p. 319.

Replacing y by ξ_n gives

$$J_1''(\xi_n) = -J_1(\xi_n) + \frac{1}{\xi_n^2} J_1(\xi_n) - \frac{1}{\xi_n} J_1'(\xi_n)$$

The last term in the above equation vanishes by virtue of (B63). We have, therefore,

$$J_1''(\xi_n) = \left(\frac{\xi_n^2 - 1}{\xi_n^2} \right) J_1(\xi_n)$$

Putting this in Eq. (B64) yields

$$\int_0^a r J_1^2 \left(\xi_n \frac{r}{a} \right) dr = \frac{a^2}{2} \left(\frac{\xi_n^2 - 1}{\xi_n^2} \right) J_1^2(\xi_n) \quad (\text{B65})$$

We may summarize the previous results as follows.

$$\int_0^a r J_1 \left(\xi_n \frac{r}{a} \right) J_1 \left(\xi_m \frac{r}{a} \right) dr = \begin{cases} 0 & \text{for } m \neq n \\ \frac{a^2}{2} \left(\frac{\xi_n^2 - 1}{\xi_n^2} \right) J_1^2(\xi_n) & \text{for } m = n \end{cases} \quad (\text{B66})$$

The first integral in Eq. (B61) remains to be evaluated. We have

$$\int_0^a r^2 J_1 \left(\xi_n \frac{r}{a} \right) dr = \frac{a^3}{\xi_n^3} \int_0^{\xi_n} \left(\frac{\xi_n r}{a} \right)^2 J_1 \left(\xi_n \frac{r}{a} \right) \left(\frac{\xi_n}{a} dr \right)$$

The integral on the right is of the form

$$\int y^2 J_1(y) dy$$

where

$$y = \xi_n \frac{r}{a}$$

$$dy = \frac{\xi_n}{a} dr$$

Since

$$\frac{d}{dy} [y^2 J_2(y)] = y^2 J_1(y)$$

it follows that

$$\int_0^a r^2 J_1 \left(\xi_n \frac{r}{a} \right) dr = \frac{a^3}{\xi_n^3} \left[\left(\frac{\xi_n r}{a} \right)^2 J_2 \left(\xi_n \frac{r}{a} \right) \right]_0^a = \frac{a^3}{\xi_n^3} J_2(\xi_n)$$

By virtue of the relation

$$y J_2(y) = J_1(y) - y J_1'(y)$$

we obtain, replacing y with ξ_n ,

$$J_2(\xi_n) = \frac{1}{\xi_n} J_1(\xi_n) - J_1'(\xi_n)$$

and since the last term vanishes by virtue of (B63), we obtain, finally,

$$\int_0^a r^2 J_1 \left(\xi_n \frac{r}{a} \right) dr = \frac{a^3}{\xi_n^2} J_1(\xi_n) \quad (\text{B67})$$

Then, using (B66) and (B67), Eq. (B61) becomes

$$\frac{a^3}{\xi_n^2} s^3 x(s) J_1(\xi_n) \cos \varphi = (s^2 + \omega_n^2) \beta_n(s) \frac{a^2}{2} \left(\frac{\xi_n^2 - 1}{\xi_n^2} \right) J_1^2(\xi_n) \cos \varphi \quad (\text{B68})$$

where the $\sum_{n=1}^{\infty}$ is implied for all terms with the subscript n .

Solving for $\beta_n(s)$, we have

$$\beta_n(s) = \frac{2a}{(\xi_n^2 - 1) J_1(\xi_n)} \cdot \frac{s^3 x(s)}{(s^2 + \omega_n^2)} \quad (\text{B69})$$

Substituting this back in Eq. (B59) gives the complete solution for the velocity potential.

$$\Phi(s) = -sx(s)r\cos\varphi + \sum_{n=1}^{\infty} \frac{2as^3x(s)J_1\left(\xi_n\frac{r}{a}\right)\cos\varphi\cosh\left[\frac{\xi_n}{a}(z+h)\right]}{(s^2+\omega_n^2)(\xi_n^2-1)J_1(\xi_n)\cosh\left(\xi_n\frac{h}{a}\right)} \quad (B70)$$

B.2.1 Dynamic Pressure at the Boundaries

Having the expression for Φ , the dynamic pressure at the walls of the tank may be calculated from Eq. (B24) with $\frac{\partial\Phi}{\partial t}$ evaluated at $r = a$; viz.,

$$p_D = \rho \left[\frac{\partial\Phi}{\partial t} \right]_{r=a} \quad (B71)$$

The force in the x direction exerted by the fluid on the tank wall is

$$(p_D \cos\varphi)(dzd\varphi) \quad (B72)$$

B.2.2 Forces in the x Direction

The force exerted by the tank walls on the fluid is equal, but opposite in sign, to expression (B72). Integrating over the whole tank, we have

$$F_x = - \int_{-h}^0 \int_0^{2\pi} \rho \left[\frac{\partial\Phi}{\partial t} \right]_{r=a} a \cos\varphi d\varphi dz = +Ms^2x(s) - M \sum_{n=1}^{\infty} \frac{A_n s^4 x(s)}{(s^2+\omega_n^2)} \quad (B73)$$

where

$$M = \rho\pi a^2 h = \text{total mass of fluid}$$

$$A_n = \frac{2a \tanh\left(\xi_n \frac{h}{a}\right)}{h \xi_n (\xi_n^2 - 1)}$$

3.2.3 Moment Due to Dynamic Pressure

The dynamic pressure produces a moment about some axis A-A passing through the z axis at a distance l from the origin and perpendicular to the x-z plane. This moment (clockwise) is given by

$$\mathcal{M} = -p_D(z-l)a^2 \cos\varphi dzd\varphi - p_D r^2 \cos\varphi drd\varphi$$

Integrating over the whole tank, we have

$$\begin{aligned}
 \eta &= - \int_{-h}^0 \int_0^{2\pi} \rho \left[\frac{\partial \Phi}{\partial t} \right]_{r=a} (z - \ell) a^2 \cos \varphi \, dz d\varphi - \int_0^a \int_0^{2\pi} \rho \left[\frac{\partial \Phi}{\partial t} \right]_{z=-h} r^2 \cos \varphi \, dr d\varphi \\
 &= -B_1 M s^2 x(s) + \frac{B_2 M s^4 x(s)}{(s^2 + \omega_n^2)}
 \end{aligned} \tag{B74}$$

where

$$\begin{aligned}
 B_1 &= \frac{a^2}{4h} - \left(\ell + \frac{h}{2} \right) \\
 B_2 &= \sum_{n=1}^{\infty} \frac{2a^2}{\xi_n^2 h} \left[\frac{2 - \cosh\left(\xi_n \frac{h}{a}\right) - \ell \frac{\xi_n}{a} \sinh\left(\xi_n \frac{h}{a}\right)}{(\xi_n^2 - 1) \cosh\left(\xi_n \frac{h}{a}\right)} \right]
 \end{aligned}$$

and where the following expressions were used in establishing the result.

$$\begin{aligned}
 \left[\frac{\partial \Phi}{\partial t} \right]_{r=a} &= -s^2 x(s) a \cos \varphi + \sum_{n=1}^{\infty} \frac{s^4 x(s)}{(s^2 + \omega_n^2)} \frac{2a \cos \varphi}{(\xi_n^2 - 1)} \frac{\cosh \frac{\xi_n}{a} (z + h)}{\cosh\left(\xi_n \frac{h}{a}\right)} \\
 \left[\frac{\partial \Phi}{\partial t} \right]_{z=-h} &= -s^2 x(s) r \cos \varphi + \sum_{n=1}^{\infty} \frac{s^4 x(s)}{(s^2 + \omega_n^2)} \frac{2a J_1\left(\xi_n \frac{r}{a}\right) \cos \varphi}{(\xi_n^2 - 1) J_1(\xi_n) \cosh\left(\xi_n \frac{h}{a}\right)}
 \end{aligned}$$

Equations (B73) and (B74) converge very rapidly. The terms with subscript $n = 2$ or higher may be dropped, therefore, without appreciable error. There results

$$F_x = M s^2 x(s) - \frac{M A_1 s^4 x(s)}{(s^2 + \omega_1^2)} \tag{B75}$$

$$\eta = -B_1 M s^2 x(s) + \frac{B_2 M s^4 x(s)}{(s^2 + \omega_1^2)} \tag{B76}$$

$$\left. \begin{aligned}
 A_1 &= \frac{2a \tanh\left(\xi_1 \frac{h}{a}\right)}{h \xi_1 (\xi_1^2 - 1)} \\
 B_1 &= \frac{a^2}{4h} - \left(\ell + \frac{h}{2}\right) \\
 B_2 &= \frac{2a^2}{\xi_1^2 h} \left[\frac{2 - \cosh\left(\xi_1 \frac{h}{a}\right) - \ell \frac{\xi_1}{a} \sinh\left(\xi_1 \frac{h}{a}\right)}{(\xi_1^2 - 1) \cosh\left(\xi_1 \frac{h}{a}\right)} \right] \\
 \omega_1^2 &= \frac{g \xi_1}{a} \tanh\left(\xi_1 \frac{h}{a}\right)
 \end{aligned} \right\} \quad (B77)$$

B.3 MECHANICAL ANALOGY

Consider the system shown in Fig. B2. Point P is constrained to move horizontally. The origin of coordinates is at 0.

The displacement of the c.g. of mass m_0 is given by

$$x_0 = x - \ell_0 \sin \theta$$

$$y_0 = -\ell_0 \cos \theta$$

Hence

$$\dot{x}_0 = \dot{x} - \ell_0 \dot{\theta} \cos \theta$$

$$\dot{y}_0 = \ell_0 \dot{\theta} \sin \theta$$

The kinetic energy of mass m_0 is therefore

$$\begin{aligned}
 T_0 &= \frac{1}{2} m_0 [(\dot{x} - \ell_0 \dot{\theta} \cos \theta)^2 + \ell_0^2 \dot{\theta}^2 \sin^2 \theta] + \frac{1}{2} I_0 \dot{\theta}^2 \\
 &= \frac{1}{2} m_0 (\dot{x}^2 + \ell_0^2 \dot{\theta}^2 - 2 \ell_0 \dot{x} \dot{\theta} \cos \theta) + \frac{1}{2} I_0 \dot{\theta}^2
 \end{aligned}$$

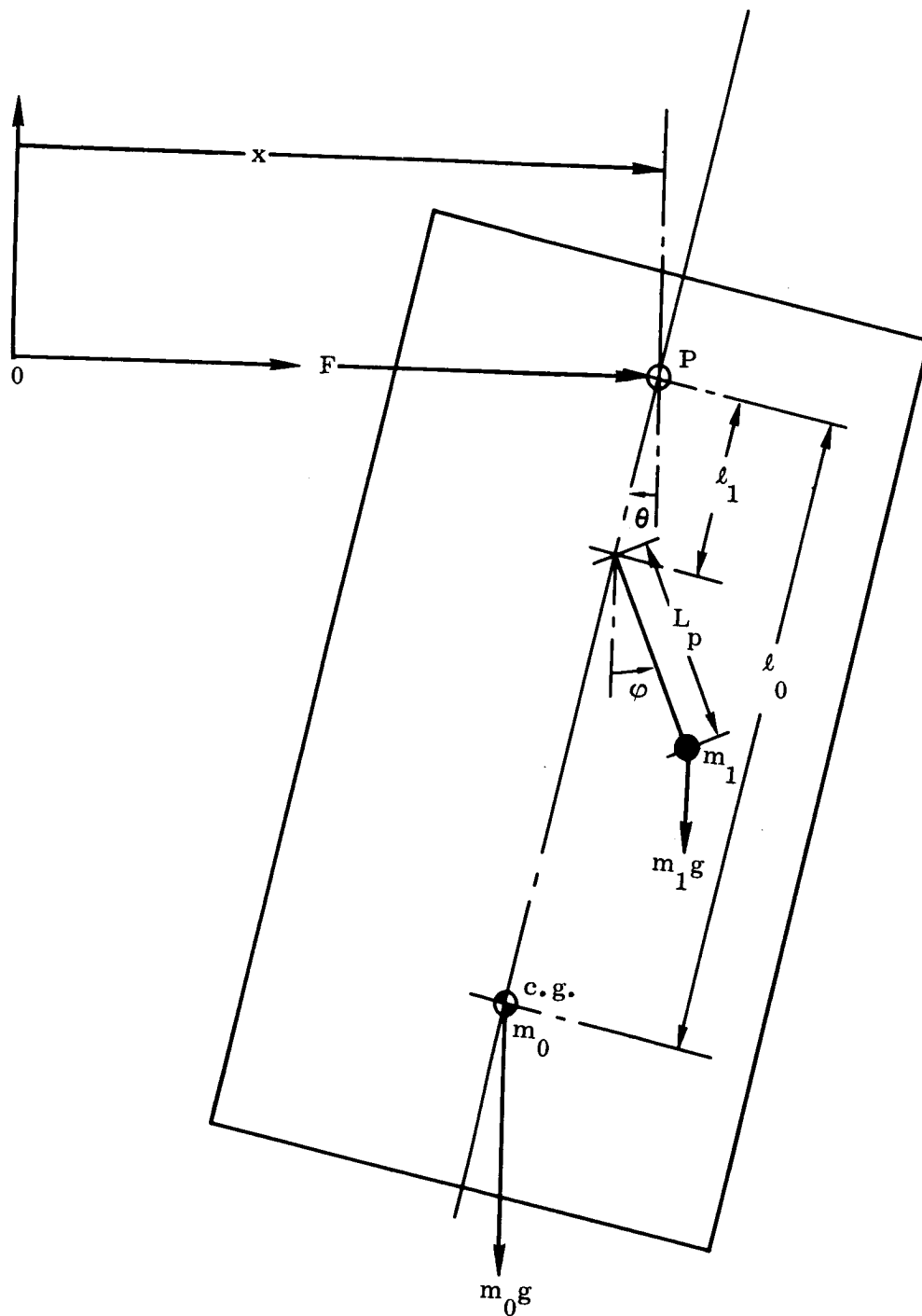


Figure B2. Analogous Mechanical System; Rotational Degree of Freedom Included

The displacement of mass m_1 is given by

$$x_1 = x - \ell_1 \sin \theta + L_p \sin \varphi$$

$$y_1 = -\ell_1 \cos \theta - L_p \cos \varphi$$

Thus

$$\dot{x}_1 = \dot{x} - \ell_1 \dot{\theta} \cos \theta + L_p \dot{\varphi} \cos \varphi$$

$$\dot{y}_1 = \ell_1 \dot{\theta} \sin \theta + L_p \dot{\varphi} \sin \varphi$$

The kinetic energy is given by

$$\begin{aligned} T_1 &= \frac{1}{2} m_1 [(\dot{x} - \ell_1 \dot{\theta} \cos \theta + L_p \dot{\varphi} \cos \varphi)^2 + (\ell_1 \dot{\theta} \sin \theta + L_p \dot{\varphi} \sin \varphi)^2] \\ &= \frac{1}{2} m_1 [\dot{x}^2 + \ell_1^2 \dot{\theta}^2 + L_p^2 \dot{\varphi}^2 + 2\dot{x}(L_p \dot{\varphi} \cos \varphi - \ell_1 \dot{\theta} \cos \theta) \\ &\quad - 2\ell_1 L_p \dot{\theta} \dot{\varphi} \cos (\theta - \varphi)] \end{aligned}$$

Hence the total kinetic energy is

$$\begin{aligned} T &= T_0 + T_1 = \frac{1}{2} m_0 (\dot{x}^2 + \ell_0^2 \dot{\theta}^2 - 2\ell_0 \dot{x} \dot{\theta} \cos \theta) + \frac{1}{2} I_0 \dot{\theta}^2 \\ &\quad + \frac{1}{2} m_1 [\dot{x}^2 + \ell_1^2 \dot{\theta}^2 + L_p^2 \dot{\varphi}^2 + 2\dot{x}(L_p \dot{\varphi} \cos \varphi - \ell_1 \dot{\theta} \cos \theta) \\ &\quad - 2\ell_1 L_p \dot{\theta} \dot{\varphi} \cos (\theta - \varphi)] \end{aligned} \tag{B-78}$$

The moment corresponding to coordinate θ is given by

$$\mathfrak{M} = \frac{d}{dt} \left(\frac{\partial T}{\partial \dot{\theta}} \right) - \frac{\partial T}{\partial \theta}$$

with

$$\frac{\partial T}{\partial \dot{\theta}} = m_0 \ell_0 (\ell_0 \dot{\theta} - \dot{x} \cos \theta) + I_0 \dot{\theta} + m_1 \ell_1 [\ell_1 \dot{\theta} - \dot{x} \cos \theta - L_p \dot{\varphi} \cos (\theta - \varphi)]$$

$$\frac{\partial T}{\partial \theta} = \{ m_0 \ell_0 \dot{x} \sin \theta + m_1 \ell_1 [\dot{x} \sin \theta + L_p \dot{\varphi} \sin (\theta - \varphi)] \} \dot{\theta}$$

Putting $\theta = \dot{\theta} = 0$ (i.e., no rotation about point P), we obtain the expression for the static moment (clockwise) about P; viz.,

$$\mathcal{M} = -(m_0 \ell_0 + m_1 \ell_1) \ddot{x} - m_1 \ell_1 L_p \ddot{\phi} \quad (\text{B79})$$

where ϕ has been assumed small.

For $\theta = 0$, the configuration is as shown in Fig. B3. In this case, the expression for kinetic energy with the assumption of small ϕ reduces to

$$T = \frac{1}{2} m_0 \dot{x}^2 + \frac{1}{2} m_1 (\dot{x}^2 + L_p \dot{\phi}^2 + 2 L_p \dot{x} \dot{\phi}) \quad (\text{B80})$$

and

$$\frac{\partial T}{\partial \dot{x}} = m_0 \dot{x} + m_1 \dot{x} + m_1 L_p \dot{\phi}$$

$$\frac{\partial T}{\partial \dot{\phi}} = m_1 L_p (L_p \dot{\phi} + \dot{x})$$

$$\frac{\partial T}{\partial x} = \frac{\partial T}{\partial \phi} = 0$$

Therefore, the equations of motion are

$$(m_0 + m_1) \ddot{x} + m_1 L_p \ddot{\phi} = F \quad (\text{B81})$$

$$\ddot{x} + L_p \ddot{\phi} = -g\phi \quad (\text{B82})$$

Expressing Eqs. (B81) and (B82) in operational notation and eliminating ϕ between them, we obtain

$$F(s) = (m_0 + m_1) s^2 x(s) - \frac{m_1 s^4}{(s^2 + \omega_p^2)} x(s) \quad (\text{B83})$$

where

$$\omega_p^2 = \frac{g}{L_p}$$

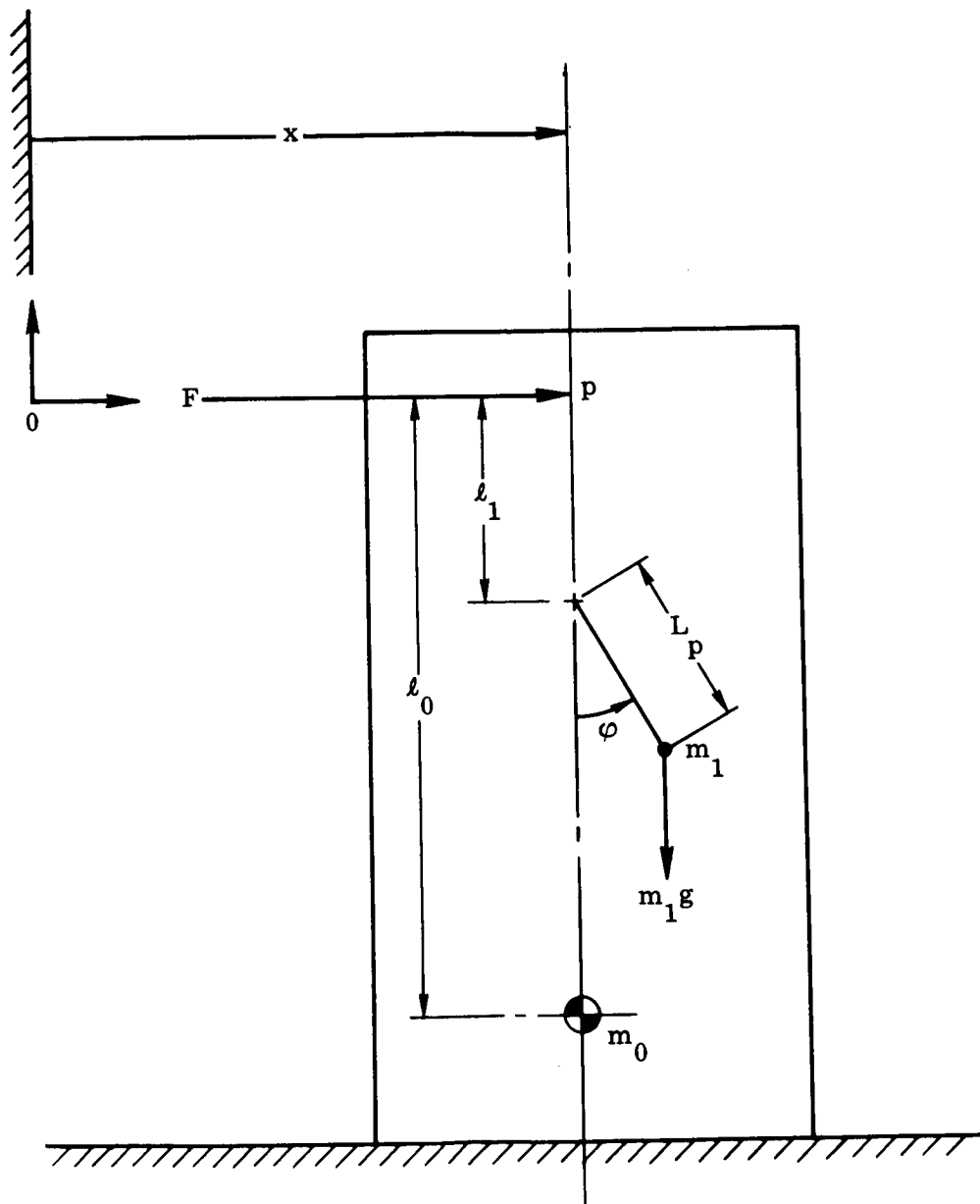


Figure B3. Analogous Mechanical System; Translational Degree of Freedom Only

Substituting Eq. (B82) in (B79) gives the expression for the static moment about P; i.e.,

$$\eta = - (m_0 \ell_0 + m_1 \ell_1) s^2 x(s) + \frac{m_1 \ell_1}{(s^2 + \omega_p^2)} s^4 x(s) \quad (\text{B84})$$

Equations (B75) and (B76) are equivalent in form to equations (B83) and (B84)

The correspondence of parameters may be set up as shown in Table B1.

Table B1. Correspondence of Parameters

	HYDRAULIC	MECHANICAL
a	M	$(m_0 + m_1)$
b	MA_1	m_1
c	$B_1 M$	$m_0 \ell_0 + m_1 \ell_1$
d	$B_2 M$	$m_1 \ell_1$
e	ω_1^2	$\frac{g}{L_p}$

From a and b of Table B1, we find

$$m_1 = MA_1 \quad (\text{B85})$$

$$m_0 = M(1 - A_1) \quad (\text{B86})$$

Also, from c and d,

$$\ell_1 = \frac{B_2}{A_1} \quad (\text{B87})$$

$$\ell_0 = \frac{B_1 - B_2}{1 - A_1} \quad (\text{B88})$$

and from e,

$$L_p = \frac{g}{\omega_1^2} \quad (B89)$$

Equations (B85) - (B89) represent the complete mechanical analogy of the hydrodynamic system herein discussed.

9124167

"The aeronautical and space activities of the United States shall be conducted so as to contribute . . . to the expansion of human knowledge of phenomena in the atmosphere and space. The Administration shall provide for the widest practicable and appropriate dissemination of information concerning its activities and the results thereof."

—NATIONAL AERONAUTICS AND SPACE ACT OF 1958

NASA SCIENTIFIC AND TECHNICAL PUBLICATIONS

TECHNICAL REPORTS: Scientific and technical information considered important, complete, and a lasting contribution to existing knowledge.

TECHNICAL NOTES: Information less broad in scope but nevertheless of importance as a contribution to existing knowledge.

TECHNICAL MEMORANDUMS: Information receiving limited distribution because of preliminary data, security classification, or other reasons.

CONTRACTOR REPORTS: Scientific and technical information generated under a NASA contract or grant and considered an important contribution to existing knowledge.

TECHNICAL TRANSLATIONS: Information published in a foreign language considered to merit NASA distribution in English.

SPECIAL PUBLICATIONS: Information derived from or of value to NASA activities. Publications include conference proceedings, monographs, data compilations, handbooks, sourcebooks, and special bibliographies.

TECHNOLOGY UTILIZATION PUBLICATIONS: Information on technology used by NASA that may be of particular interest in commercial and other non-aerospace applications. Publications include Tech Briefs, Technology Utilization Reports and Notes, and Technology Surveys.

Details on the availability of these publications may be obtained from:

SCIENTIFIC AND TECHNICAL INFORMATION DIVISION
NATIONAL AERONAUTICS AND SPACE ADMINISTRATION

Washington, D.C. 20546